

用于量子计算的离子阱技术研发

(申请清华大学理学博士学位论文)

[b]培养单位：交叉信息研究院

[b]学科：物理

[b]研究生：汪野

[b]指导教师：金奇奂教授

二〇一七年十一月

Development of Trapped Ion System for Quantum computing

Thesis Submitted to
Tsinghua University
in partial fulfillment of the requirement
for the professional degree of
Doctor of Philosophy

by
Wang Ye
(Physics)

Thesis Supervisor : Professor Kihwan Kim

November, 2017

关于学位论文使用授权的说明

本人完全了解清华大学有关保留、使用学位论文的规定，即：

清华大学拥有在著作权法规定范围内学位论文的使用权，其中包括：（1）已获学位的研究生必须按学校规定提交学位论文，学校可以采用影印、缩印或其他复制手段保存研究生上交的学位论文；（2）为教学和科研目的，学校可以将公开的学位论文作为资料在图书馆、资料室等场所供校内师生阅读，或在校园网上供校内师生浏览部分内容。

本人保证遵守上述规定。

（保密的论文在解密后应遵守此规定）

作者签名： _____

导师签名： _____

日 期： _____

日 期： _____

摘 要

关键词: $\text{T}_{\text{E}}\text{X}$; $\text{L}^{\text{A}}\text{T}_{\text{E}}\text{X}$; CJK; 模板; 论文

Abstract

Key words: T_EX; L^AT_EX; CJK; template; thesis

目 录

| | | |
|-------|--|----|
| 第1章 | Introduction | 1 |
| 1.1 | Single-qubit quantum memory | 1 |
| 1.2 | A scalable three-dimensional monolithic trap | 2 |
| 1.3 | Thesis structure | 3 |
| 第2章 | Trap ion system | 4 |
| 2.1 | Principle for Paul trap | 4 |
| 2.1.1 | Average of an oscillation electric field..... | 4 |
| 2.1.2 | Mathieu equation | 6 |
| 2.1.3 | Structure..... | 7 |
| 2.1.4 | Helical resonator..... | 8 |
| 2.2 | $^{171}\text{Yb}^+$ ion | 9 |
| 2.2.1 | Energy level | 9 |
| 2.2.2 | Basic operation: ionization, Doppler cooling, pumping and detection | 10 |
| 2.2.3 | Laser system | 11 |
| 2.3 | $^{138}\text{Ba}^+$ ion | 13 |
| 2.3.1 | Energy level | 13 |
| 2.3.2 | Basic operation: ionization, Doppler cooling, pumping and detection | 14 |
| 2.3.3 | Laser system | 14 |
| 2.4 | Image system | 14 |
| 2.5 | Control system | 15 |
| 第3章 | Single ion quantum memory | 18 |
| 3.1 | Background of quantum memory | 18 |
| 3.2 | Sympathetic cooling | 19 |
| 3.2.1 | Laser system | 20 |
| 3.2.2 | Loading $^{171}\text{Yb}^+$ and $^{138}\text{Ba}^+$ ion | 22 |
| 3.2.3 | Cooling effect | 22 |
| 3.3 | Dynamical decoupling..... | 23 |
| 3.3.1 | Introduction | 23 |
| 3.3.2 | Calculation of the filter function | 24 |
| 3.3.3 | Filter function of CPMG and KDD | 27 |

| | | |
|-------|--|----|
| 3.3.4 | Environment noise | 29 |
| 3.3.5 | Slow magnetic field drifting..... | 32 |
| 3.4 | Microwave gate | 32 |
| 3.4.1 | Control of DDS | 34 |
| 3.4.2 | DDS performance | 35 |
| 3.4.3 | Random benchmarking test | 35 |
| 3.5 | Control system and Data taking | 37 |
| 3.5.1 | FPGA control system..... | 38 |
| 3.5.2 | One shot data taking..... | 38 |
| 3.5.3 | Process tomography | 41 |
| 3.5.4 | Outlook..... | 41 |
| 第4章 | Monolithic 3D ion trap design | 44 |
| 4.1 | Background | 44 |
| 4.2 | Design of the monolithic trap | 45 |
| 4.3 | Trap simulation | 46 |
| 4.3.1 | CPO simulation | 47 |
| 4.3.2 | Simulation analysis | 50 |
| 4.3.3 | Trap performance simulated with different parameters | 53 |
| 4.3.4 | Compare with other traps | 57 |
| 4.4 | electrode control | 58 |
| 4.4.1 | Control of the axial potential..... | 58 |
| 4.4.2 | Control of the radial frequency | 59 |
| 4.4.3 | Rotate the axis angle..... | 60 |
| 第5章 | Trap Fabrication and assembling | 63 |
| 5.1 | Fabrication technique | 63 |
| 5.1.1 | Steps to make the trap | 63 |
| 5.1.2 | Laser cutting | 64 |
| 5.1.3 | Gold coating | 67 |
| 5.2 | Design of the main chamber..... | 67 |
| 5.2.1 | Low-pass filter | 68 |
| 5.2.2 | Electronic connection | 68 |
| 5.2.3 | Holder design | 70 |
| 5.2.4 | Oven design | 70 |

| | | |
|-----------------------|--|-----|
| 5.3 | Assembling process | 71 |
| 5.3.1 | Main part assemble | 72 |
| 5.3.2 | Vacuum system assemble | 74 |
| 5.3.3 | Pump and bake process | 74 |
| 第6章 | Trap testing | 76 |
| 6.1 | Load $^{171}\text{Yb}^+$ and $^{138}\text{Ba}^+$ | 76 |
| 6.1.1 | Laser system | 76 |
| 6.1.2 | Laser and image system alignment | 77 |
| 6.1.3 | Loading procedure | 78 |
| 6.2 | Control ability of the DC electrodes | 81 |
| 6.2.1 | Micromotion compensation | 81 |
| 6.2.2 | Axial and radial frequency measurement | 83 |
| 6.2.3 | Compare to the simulation data | 86 |
| 6.3 | Heating rate measurement | 89 |
| 6.3.1 | Doppler re-cooling method | 89 |
| 6.3.2 | Sideband cooling method | 89 |
| 6.3.3 | Principle axes angle measurement | 93 |
| 6.4 | Remain problems | 94 |
| 第7章 | Conclusion and outlook | 96 |
| 插图索引 | | 97 |
| 表格索引 | | 101 |
| 公式索引 | | 102 |
| 参考文献 | | 105 |
| 致 谢 | | 110 |
| 声 明 | | 111 |
| 附录 A | Codes | 112 |
| A.1 | Mathematica simulation program | 112 |
| A.2 | Program for generating different model with different parameters | 116 |
| A.3 | KDD _{xy} sequence | 122 |
| 个人简历、在学期间发表的学术论文与研究成果 | | 126 |

第1章 Introduction

The idea of quantum computer could be traced back to the early 1980's when proposals made by Feynman^[1] and Deutsch^[2]. Feynman suggested using a simple well-controlled quantum system to emulate the behavior of another complex quantum system, which may need exponentially increasing calculation time using classical computing methods. Deutsch suggested using the quantum parallelism to solve a mathematical problem, which lies on the fundamental properties of a quantum system: quantum superposition and quantum entanglement. These ideas inspired people to find more practical algorithms, such like Shor's algorithm^[3], Grover's algorithm^[4] and quantum simulation algorithms^[5]. These years, several systems have been developed to be the platform for a quantum computer, which include quantum optics, NV (nitrogen vacancy) centers in diamond, superconducting system, molecular and atomic systems. Among them, trapped ion system is the oldest and most mature candidate, which have been shown to satisfy all the requirement for a large-scale quantum computer proposed by DiVincenzo^[6], especially the advantage of high fidelity of fundamental operations, relative slow decoherence rate, the architecture for a large quantum system. In this thesis, we will show two technological development for trapped ion system toward the large-scale quantum system, which are the single-qubit quantum memory with long coherence time and a scalable three-dimensional monolithic trap for quantum computing.

1.1 Single-qubit quantum memory

A long-time quantum memory capable of storing and measuring quantum information at the single-qubit level is an essential ingredient for practical quantum computation and communication^[7,8]. The unique quantum nature like no-cloning principle, the impossibility of copying a quantum information, can be observed and utilized with only the capability of coherently manipulating and detecting an individual quantum system, a qubit in the most elementary level^[9,10]. Without the accessibility to individual qubits, it is fundamentally inconceivable to store, operate and retrieve a quantum information in ensemble of qubits. It has been a long quest to develop technologies to coherently process and detect a quantum information in a single qubit level. More than twenty years ago, the coherence time of around 10 minutes was observed in ensemble of ions with

magnetic-field insensitive states^[11,12]. After more than ten years of developments, the coherence time of a single qubit with magnetic-field insensitive states was able to be measured^[13]. Unexpectedly, the reported coherence time of a single qubit is much shorter than those of ensemble systems. The technology of controlling the field-insensitive qubit has been seriously improved, but the coherence time of a single qubit was still observed as less than 1 minute. Recently, an hour-level of coherence time was reported in ensemble of nuclear spins of ionized donors^[14,15], but the coherence time of a single qubit in such solid systems has not been yet reported, to our knowledge.

In the thesis, we will report the observation of over 10-minutes coherence time of a single qubit in a $^{171}\text{Yb}^+$ ion sympathetically cooled by a $^{138}\text{Ba}^+$ ion in the same Paul trap, which eliminates the problem of qubit-detection inefficiency from the heating of the qubit ion^[16,17]. We also apply a few thousands of dynamical decoupling pulses to suppress ambient noise from magnetic-field fluctuation^[14,15,18–22]. The long-time quantum memory of the single trapped ion qubit would be the essential component of scalable quantum computer^[7,23,24], quantum networks^[8,25,26] and quantum money^[9,10].

1.2 A scalable three-dimensional monolithic trap

One of the core problem of the scalable trapped ion quantum computer is the technological path to scale up the trapped ion system. One possible method is the the ion shuttling in a complex ion trap^[27]. In all of this work, ions will be confined in linear traps, which provide the strongest confinement in any atomic or ionic system. Instead of simply adding ions to a single trapping zone, scaling will require the fabrication of complicated trap structures where ions can be shuttled between different regions by appropriately changing the static voltages on the linear trap so that ions ride a “wave” of electric potential through the structure. This arrangement known as a “quantum CCD” . An important component of this proposal is to miniaturize linear trap structures from the millimeter-scale to the micrometer scale. Since the speed of most multi-ion qubit gates is proportional to the ions’ motional frequencies and these frequencies are inversely proportional to the square of the trap dimensions, we would like to decrease the size of these dimensions. To do this robustly, micro-fabrication techniques are required.

In the thesis, we will report the whole process of design, simulation, fabrication, and test.

1.3 Thesis structure

Chapter 2 is mainly about the basic principle and introduction of our trapped ion system. Since there are many good reference of these basic things, I will focus on our realization and some knowledge we may use in the later chapters.

Chapter 3 will introduce the main technique we used to maintain a long coherence time, including the sympathetic cooling, environment noise study, dynamical decoupling, quantum process tomography. We also describe the system details like the control system and the laser system.

Chapter 4 is about the design of the monolithic trap. We describe the simulation tool, verify the validity of the simulation, then use the simulation tool to improve the design. We also show some control capability with the simulation results.

Chapter 5 is about the fabrication technology. We introduce the fabrication procedure, some mistake we made and the assembling details.

Chapter 6 is about the test of the trap. We show the performance of the trap, the comparison between the real data and simulated result. We adjust the model for simulation, and success to predict the two-dimensional ion crystal.

第2章 Trap ion system

2.1 Principle for Paul trap

The radiofrequency (RF) ion trap is the most important tool for the experiment in the following chapters. The RF ion trap was invented by Wolfgang Paul, who shared the 1989 Nobel prize^[28]. Almost 40 years ago, David Wineland et al.^[29] and Neuhauser et al.^[30] independently present the first laser-cooling experiments in ion trap. The RF ion trap system has been used for a wealth of applications, including quantum information, atomic clocks, precision measurement, mass and frequency spectroscopy^[31–34]

2.1.1 Average of an oscillation electric field

We know "a charged particle cannot be held in a stable equilibrium by electrostatic forces alone" from Earnshaw's Theorem^[35]. We also know this from free spaces Maxwell equation $\nabla \cdot \hat{E} = 0$, because the electric field lines entering a region also need a exhibition. However, it is still possible to confine the charged particle with either a combination of electric and magnetic fields (Penning trap) or dynamic electric field which is the method we use in the Paul trap.

Let's see the average force of a dynamic field following the reference^[36]. We write the spatial dependence of the field as $E_0(z)$, while the time dependence as $\cos(\Omega_T t)$. The force is simply:

$$F = m\ddot{z} = eE_0(z) \cos(\Omega_T t) \quad (2-1)$$

By integrating this equation, we have

$$z(t) = z_0 - \frac{eE_0(z)}{m\Omega_T^2} \cos(\Omega_T t) \quad (2-2)$$

The electric field around point z_0 can be expanded as

$$E_0(z) \approx E_0(z_0) + \frac{\partial E_0(z_0)}{\partial z_0} \left(\frac{eE_0(z_0)}{m\Omega_T^2} \cos(\Omega_T t) \right) \quad (2-3)$$

where we assume the derivative of $E_0(z_0)$ is much smaller than $E_0(z_0)$. So we can write

the equation for the force on the charged particle like

$$\begin{aligned} F &= eE_0(z) \cos(\Omega_T t) \\ &\approx eE_0(z_0) \cos(\omega_T t) - e \frac{\partial E_0(z_0)}{\partial z_0} \left(\frac{eE_0(z_0)}{m\Omega_T^2} \cos(\Omega_T t) \right)^2 \end{aligned} \quad (2-4)$$

Average the force over one oscillation period, we have

$$\begin{aligned} \bar{F} &= -\frac{e^2}{2m\Omega_T^2} \frac{\partial E_0(z_0)}{\partial z_0} E_0 \\ &= -e \frac{\partial \psi_p}{\partial z_0} \end{aligned} \quad (2-5)$$

where we defined the pseudo-potential, ψ_p , as

$$\psi_p = \frac{eE_0^2}{4m\Omega_T^2} \quad (2-6)$$

This result shows the time averaged force of an inhomogeneous, oscillating electric field does not vanish. We may have some effective potential. Extending this to three dimension, the result is

$$\bar{F} = -e\nabla\psi_p \text{ with } \psi_p = \frac{e(\hat{E}_0(x, y, z))^2}{4m\Omega_T^2} \quad (2-7)$$

This is a good description for the effective motion of a charged particle in a oscillating electric field. In our trapped ion system, we want to know $\hat{E}_0(x, y, z)$ in detail. We first consider the idealized hyperbolic electrode, give the two opposite electrodes potential $V_0 \cos(\Omega_T t)$, while the other two electrodes are held at 0. the potential is given like

$$\phi_{hyp} = \frac{V_0}{2} \cos(\Omega_T t) \left(1 + \frac{x^2 - y^2}{R^2} \right) \quad (2-8)$$

The electric field of this potential is

$$\begin{aligned} \hat{E}(x, y, t) &= -\nabla\phi_{hyp} \\ &= -\frac{V_0}{R^2} (x\hat{x} - y\hat{y}) \cos(\Omega_T t) \\ &= -\hat{E}_0(x, y) \cos(\Omega_T t) \end{aligned} \quad (2-9)$$

Then we can know the average force as

$$\bar{F} = -\frac{e^2 V_0^2}{2m\Omega_T^2 R^4} x \hat{x} - \frac{e^2 V_0^2}{2m\Omega_T^2 R^4} y \hat{y} \quad (2-10)$$

We can know the motion equation as

$$\ddot{x} = -\frac{e^2 V_0^2}{2m^2 \Omega_T^2 R^4} x \quad (2-11)$$

This can be view as the equation for a harmonic oscillator with

$$\omega_x = \frac{eV_0}{2^{1/2} m \Omega_T R^2} \quad (2-12)$$

We called ω_x as the secular motion frequency in the x axis. It's exactly same for the y axis. Thus, we see the effective potential of an oscillating quadrupole field is a harmonic potential, which can trap a charged particle.

2.1.2 Mathieu equation

In the previews section, we discuss the motion on a charged particle driven by the average force of a dynamic filed, which is the first order approximation of the oscillating field. In this section we will use the Mathieu equation to see the motion more clearly.

According to Eq. 2-8 and Eq. 2-9, we know

$$F_x = m\ddot{x} = -\frac{eV_0}{R^2} \cos(\Omega_T t) x \quad (2-13)$$

which yielding the equation of motion

$$\ddot{x} + \frac{eV_0}{mr^2} \cos(\Omega_T t) x = 0 \quad (2-14)$$

This is a simplified version of a Mathieu equation, which the general form is

$$\frac{d^2 u}{d\tau^2} + (a_u + 2q_u \cos(2\tau)) u = 0 \quad (2-15)$$

Our Eq. 2-14 can be realize by setting $2\tau = \Omega_T t$. So that it can be written as

$$\frac{d^2 x}{d\tau^2} + 2q_x \cos(2\tau)x = 0 \quad (2-16)$$

where

$$\begin{aligned} q_x &= (e2V_0)/(mR^2\Omega_T^2) \\ &= 2\sqrt{2}\omega_x/\Omega_T \end{aligned} \quad (2-17)$$

Here we neglected the third dimension of the confinement. If we have the third dimension confinement, $a_x \neq 0$ ^[37].

The general solution is in the form

$$x(\tau) = A \sum_{-\infty}^{\infty} C_{2n} \cos((2n + \beta)\tau) + iB \sum_{-\infty}^{\infty} C_{2n} \sin((2n + \beta)\tau) \quad (2-18)$$

where A,B are determined by the initial conditions, β and C_{2n} is solved by substitution. We omit the details of solving all these parameter in reference^[38], but give the final result as

$$x(t) = AC_0 \cos(\omega_x t) \left[1 + \frac{q_x}{2} \cos(\Omega_T t) \right] \quad (2-19)$$

Now we see there is another oscillation beyond the secular motion with frequency Ω_T , which is called "micromotion". In general, we can have a stable trap when $q_x \ll 1$ ^[39].

2.1.3 Structure

We are using a four-rod trap for most of the experiments in our lab. The diameter of each rod is 0.5 mm, the distance between the center of two neighbor rod is 1 mm. DC electrodes and RF electrodes are mounted with a pair of 5 holes ceramic tubes which are cut and drilled by laser machining. There are two more rod parallel to the old four rod using for micromotion compensation.

We put 4 atomic oven filled with natural Yb, $^{171}\text{Yb}^+$, natural Ba and $^{138}\text{Ba}^+$ are mounted on the chamber as the atom sources. The resistance of these oven is around 0.5 Ω . We design all the holder by "Autodesk Inventor". We can also do the assembling of all the component to make sure about the parameters.

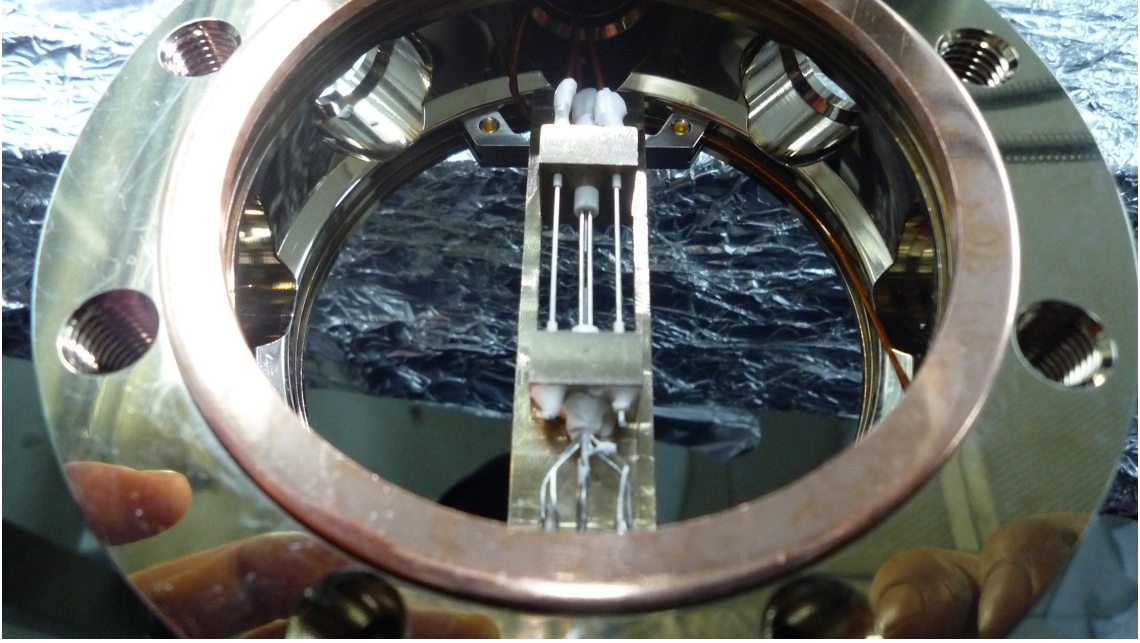


图 2.1 Our four-rod trap

2.1.4 Helical resonator

We use helical resonator^[40] to have a high quality radio frequency signal. The helical resonator act as a cavity, smaller the cavity is, the higher resonance frequency is has. We care about the quality factor Q which indicate the power amplification ration. We sweep the input frequency and measure the reflection signal spectrum. We know

$$Q \approx \frac{\omega}{\delta\omega} \quad (2-20)$$

where ω is the center frequency and $\delta\omega$ is the full width at half maximum.

One way to increase the Q factor is to reduce the resister of the whole loop. We always use phosphoric acid to clean the surface then use the sand paper to polish it again. We can have $Q \approx 400$ without loading and $Q \approx 200$ with the trap. The drive frequency we use is $\Omega_T = 12.6$ MHz for single ion experiment and $\Omega_T = 24$ MHz for two ion experiment, for the four-rod trap. From Eq. 2-12, we can have bigger secular frequency ω_x with smaller Ω_T . However, from Eq. 2-17, we know smaller Ω_T will cause bigger q_x which make the trap unstable. So if we want to have stable trap with secular frequency $\omega_x \approx 3$ MHz, we should use bigger Ω_T and bigger power V_0 .

2.2 $^{171}\text{Yb}^+$ ion

There are a lot of species can be used for the quantum information include Ba^+ , Be^+ , Ca^+ , Cd^+ , Mg^+ , Sr^+ and Yb^+ . We use Yb^+ ions. Because it has a strong dipole transition between $^2S_{1/2} \leftrightarrow ^2P_{1/2}$, the spin-1/2 nucleus of $^{171}\text{Yb}^+$ has hyperfine structures with simple, fast and efficient preparation and detection. The basic technique to manipulate $^{171}\text{Yb}^+$ is developed by Monroe's group in University of Maryland and a lot of important results are demonstrate with $^{171}\text{Yb}^+$ ions^[41-45]. We will describe the basic idea for using $^{171}\text{Yb}^+$ ion as a qubit.

2.2.1 Energy level

For $^{171}\text{Yb}^+$, its ground energy level are degenerated and split into Zeeman levels. We use the dipole transitions between $^2S_{1/2} \leftrightarrow ^2P_{1/2}$, which can be use as the cycle for Doppler cooling, pumping and state detection. The energy level are shown in the Fig. 2.2.

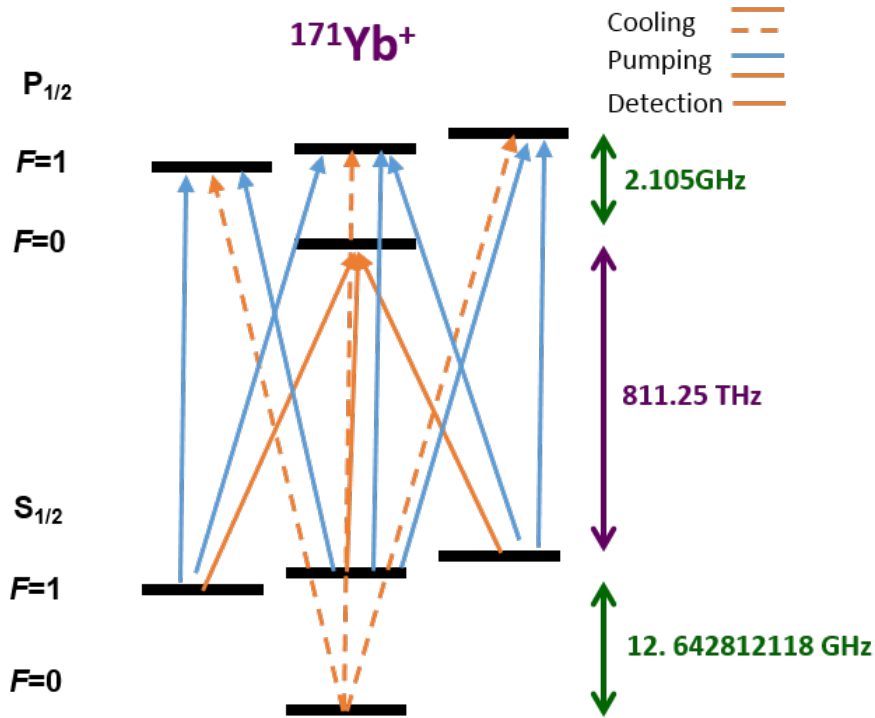


图 2.2 Energy level of $^{171}\text{Yb}^+$

The two hyperfine levels of $^{171}\text{Yb}^+$ ion in the $^2S_{1/2}$ manifold are used as a qubit represented by $|\downarrow\rangle \equiv |F=0, m_F=0\rangle$ and $|\uparrow\rangle \equiv |F=1, m_F=0\rangle$, which is separated by

$12642812118 + 310.8B^2$ Hz, where B is magnetic field in Gauss. In experiment, we initialize the qubit state to $|\downarrow\rangle$ by the standard optical pumping method and discriminate the state by the fluorescence detection scheme. We perform the coherent manipulation of qubit by applying the resonant microwave.

2.2.2 Basic operation: ionization, Doppler cooling, pumping and detection

To load the $^{171}\text{Yb}^+$ ion, the first thing is the ionization. We use the atomic oven to generate the atom beam. The oven is heated up around the sublimation temperature for Yb ions around 480°C in UHV^[46]. A $300\ \mu\text{W}$ $398.9108\ \text{nm}$ laser and a $2\ \text{mW}$ $369.5263\ \text{nm}$ laser is used for the ionization process. The two beam is focused to around $40\ \mu\text{m}$ waist at the ion position. The Yb atoms will be photon-ionized by the way of resonantly assisted dichroic two-photo transition with two laser^[38]. We need to add Doppler frequency shift due to the angle between atomic oven and the laser.

For the Doppler cooling, we use a around $2\ \mu\text{W}$ $369.5263\ \text{nm}$ laser beam focus on the ion position with waist around $40\ \mu\text{m}$. The laser is slightly red-detuned (normally around $15\ \text{MHz}$) from the resonance of transition $^2S_{1/2} \leftrightarrow ^2P_{1/2}$. The ion on $^2S_{1/2}$ will absorb one photon and go to the $^2P_{1/2}$ state, whose life time is $8.7\ \text{ns}$. Then the ion will spontaneously emit a photon to all direction with uniformly random distribution. Typically, we shine the Doppler cooling beam for $1\ \text{ms}$, so that the ion will be cooled to around 10 average phonon. As shown in the Fig. 2.2, we need a $14.74\ \text{GHz}$ sideband to cover all the transitions between hyperfine levels.

We also need a re-pump laser since the 0.5% leakage on the metastable state $^2D_{3/2}$. We use $935.1882\ \text{nm}$ laser with $10\ \text{mW}$ to bring the ion back into the Doppler cooling cycle. This beam need a $3.1\ \text{GHz}$ sideband.

Sometimes the collisions make the ion go to the $^2F_{7/2}$ state. We use a beam in the range of $638.6101\ \text{nm}$ to $638.6151\ \text{nm}$ with around $5\ \text{mW}$ to bring the ion back to the Doppler cooling cycle.

The optical pumping laser is the $369.5263\ \text{nm}$ laser with a $2.105\ \text{GHz}$ sideband. As shown in Fig. 2.2, the sideband doesn't cover the transition from $|F = 0, m = 0\rangle$, which means $|F = 0, m = 0\rangle$ will not be excited. So all the other state will go down to the $|F = 0, m = 0\rangle$ by spontaneously emission. We use around $5\ \mu\text{s}$ for the optical pumping process. The pumping efficiency is around 99.5% .

We can do the quantum state detection by fluorescence detection scheme. We use the

369.5263 nm laser beam without sideband which is only resonant to ${}^2S_{1/2} : |F = 1\rangle \leftrightarrow {}^2P_{1/2} : |F = 0\rangle$ transition. We distinguish the state by the emitted rate of the photon, if the emission rate is bigger than $1/300\mu\text{s}$, we consider the state is at ${}^2S_{1/2} : |F = 0\rangle$, otherwise we consider the state is at ${}^2S_{1/2} : |F = 1\rangle$. We use the PMT (photomultiplier tube) to count the photon.

2.2.3 Laser system

In this section we will briefly introduce the laser system we use to manipulate the ${}^{171}\text{Yb}^+$ ion. The main laser for ${}^{171}\text{Yb}^+$ is the 369 nm laser which is generated by the Toptica SHG laser. This laser generate the 369 nm laser by using SHG to double the frequency of the seed laser 739 nm laser. We have two output for this laser, one is for 739 nm laser, chose power is around 40 mW, one is for 369 nm laser, whose power is around 15mW.

We have wavelength fluctuation on the 369 nm laser output due to the temperature and current noise. To have a stable detection and pumping laser for ${}^{171}\text{Yb}^+$ ion, we need lock the wavelength of the laser to some reference. We are using the Fabry-Perot cavity and Pound-Drever-Hall method^[47] to compensate the fast fluctuation. Then we lock the cavity length to an absolute frequency reference provided by an Iodine vapor cell to compensate to long time drift^[38]. A 13GHz fiber EOM is used to shift the frequency to the Iodine reference point. After locking to the cavity and Iodine, we may have the laser linewidth less than 1 MHz. The lock point can be shifted by changing the EOM's driving frequency in the control system.

We separate 369 nm laser into three path for four purposes which are Doppler cooling, optical pumping, detection and strong beam for ionization. Fig. 2.3 shows the diagram of the optical components. We use three AOMs (Acousto-Optic Modulator) to be the switch for each path. We use two EOMs (Electro-optic modulator) to generate the sideband of the Doppler cooling and optical pumping beam. The strong beam and the detection beam don't need the sideband, so we can just use one AOM to have both of them, which are the 0 order and 1 order of the AOM output. We use a PBS (polarized beam splitter) to merge the four as shown in the Fig. 2.3

The 935.1882 nm laser is directly locked to the HighFinesse wavelength meter with precision around 20 MHz. We use the 739.0526 nm laser locked to the Iodine as a reference for the wavelength meter.

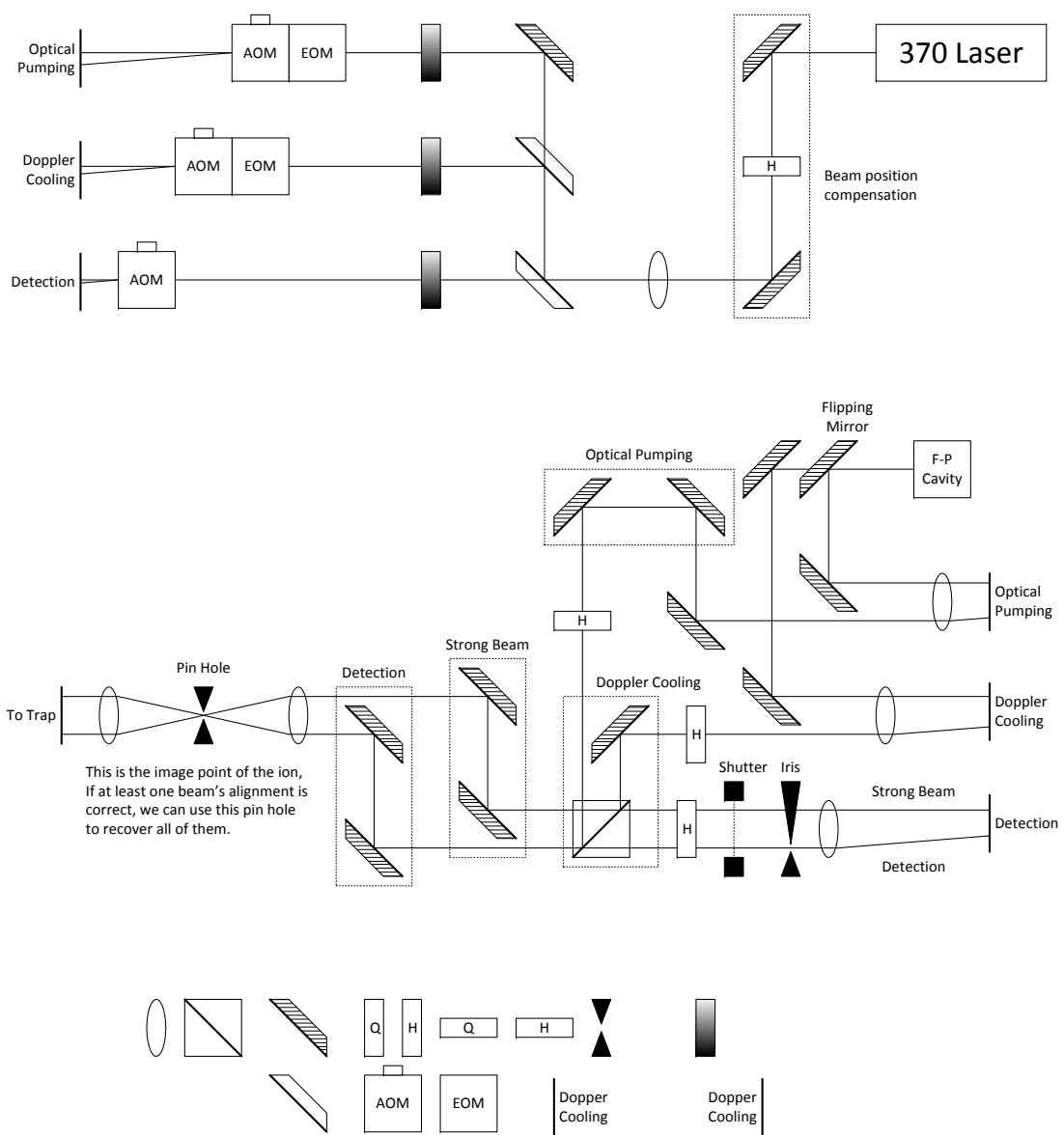


图 2.3 Diagram of the 370 laser system.

2.3 $^{138}\text{Ba}^+$ ion

The $^{138}\text{Ba}^+$ ion has already study by a lot groups in the world. We are interested in the $^{138}\text{Ba}^+$ ion since the wavelength, 493 nm, of the qubit transition is kind for fiber transmission and the mass of $^{138}\text{Ba}^+$ is close to $^{171}\text{Yb}^+$, which helps the sympathetic cooling and motion operation between $^{171}\text{Yb}^+$ and $^{138}\text{Ba}^+$ [48,49]. We are using $^{138}\text{Ba}^+$ for the multi-species experiments.

2.3.1 Energy level

In my experiment, we use $^{138}\text{Ba}^+$ ion mainly as a sympathetic cooling ion. We use the dipole transition between $6^2S_{1/2} \leftrightarrow 6^2P_{1/2}$ for the Doppler cooling. Because the branching ratios between $6^2S_{1/2} \leftrightarrow 5^2D_{3/2}$ is big, 27.1% [50,51], it is important to use a laser to bring the state from $5^2D_{3/2}$ back to $6^2P_{1/2}$ to keep the Doppler cooling cycle. The energy level is shown in the Fig. 2.4.

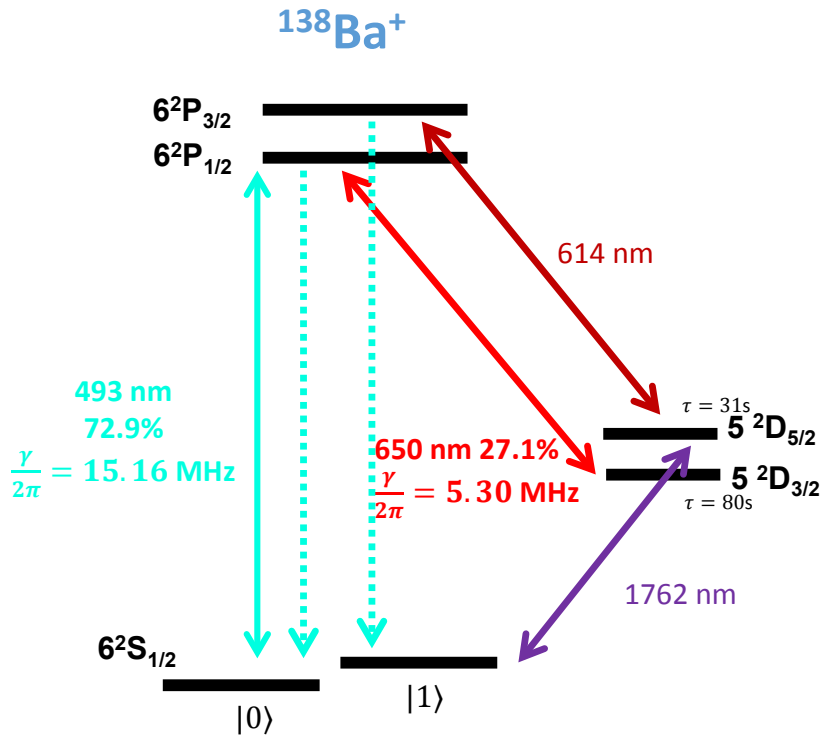


图 2.4 Energy level of $^{138}\text{Ba}^+$

2.3.2 Basic operation: ionization, Doppler cooling, pumping and detection

We use 413 nm laser first excite the atom and then use 493 nm laser to ionize the ion. We apply 493 nm laser with a slightly red detuning to excite all the possible transition between $S_{1/2}$ and $P_{1/2}$ to make the Doppler cooling cycle. We use the two Zeeman state of $S_{1/2}$ as the qubit. For the optical pumping process, we first apply the 614 nm laser to repump the population from $D_{5/2}$. Then we apply a pure σ^+ polarization 493 nm laser to pump the population to $|m = -1\rangle$. For detection, we shelve the population on $|m = +1\rangle$ to the metastable level $D_{5/2}$ with 1762 nm laser through an electric quadrupole transition^[52]. Then we excite the cyclic transition between $S_{1/2}$ and $P_{1/2}$ with 493 nm laser. Then we collect the emit photon and distinguish the state by the photon count.

2.3.3 Laser system

The diagram of the laser system is shown in the Fig. 2.5. The 493 nm laser is used for Doppler cooling, optical pumping, detection and EIT cooling process. The significance of 493 nm laser for $^{138}\text{Ba}^+$ is same as the 369 nm laser for $^{171}\text{Yb}^+$. So we make a similar system for the wavelength locking of 493 nm laser. The laser is lock to a Fabry-Perot cavity, whose cavity length is locked to a tellurium vapor cell using Doppler-free spectroscopy^[53]. We are using a double pass AOM system to shift the locking point. 650 nm laser is locked to the wavelength meter. All the three laser are coupled to the fiber, and merged before the trap.

2.4 Image system

To load $^{171}\text{Yb}^+$ and $^{138}\text{Ba}^+$ together, we need the individual laser system and image system. We have already described about the laser system. We will talk about the image system.

The fluorescence wavelength of $^{171}\text{Yb}^+$ and $^{138}\text{Ba}^+$ ion is 369 nm and 493 nm. The different of wavelength will introduce the different of the image system. We use two re-entrant viewport on our octagon chamber on the top and bottom side. As shown in the Fig. 2.6, we make two image system on the both side with same objective lens, one is for $^{171}\text{Yb}^+$ and the other one is for the $^{138}\text{Ba}^+$. Due to the different wavelength, the focus length of the first objective lens is different for two systems. So the position of the second stage of the image system is different as shown in the figure. Of cause, the final position of CCD and PMT is different for two systems. When we have two different species of

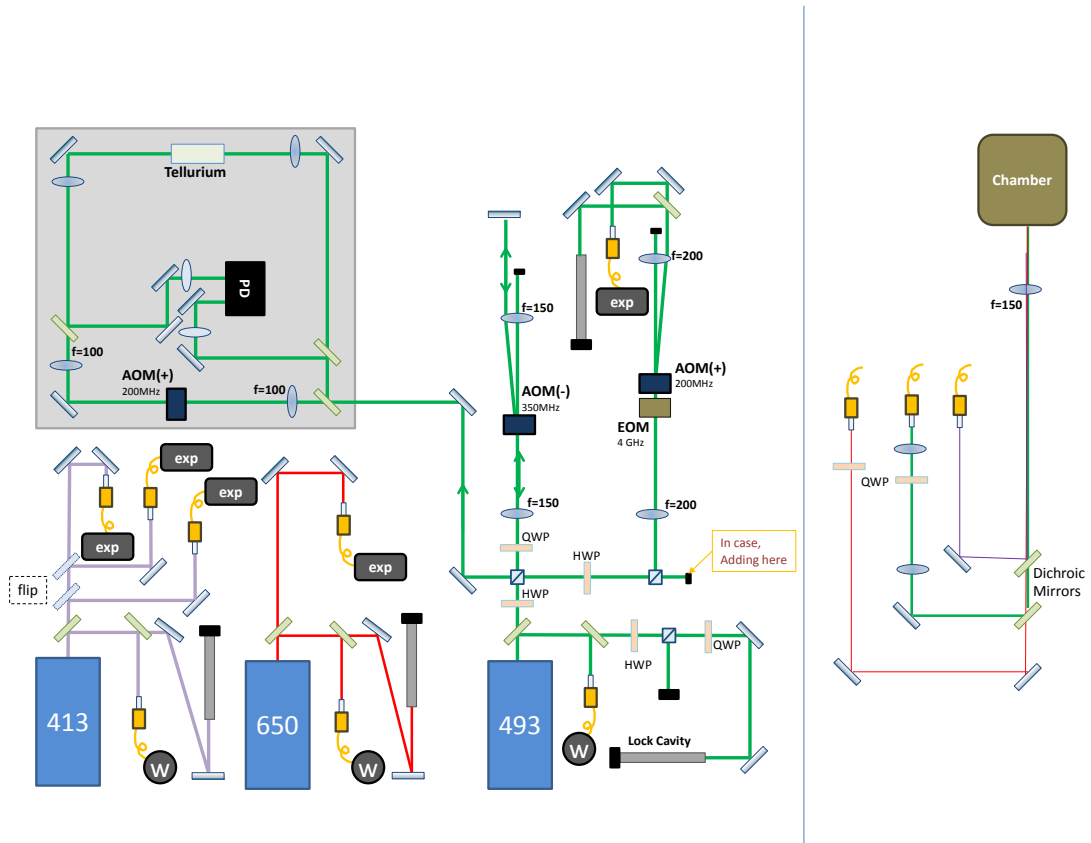


图 2.5 Diagram of the laser system used for $^{138}\text{Ba}^+$.

ions, we can see each ion with different image system. For every CCD, we can only see one ion showing in the Fig. 2.7

2.5 Control system

You can roughly think the trap ion system consisting of vacuum system, laser system, analog signal system. The control system combine these three system working together so that we can run the experiment. The control system is divided into three part:

1. **Digital control part** This part control the timing sequence of every equipment, such as the AOM switch of laser, the microwave switch and etc. The time precision of our system is 5 ns.
2. **Analog control part** This part control part of the analog signal through DDS or AWG. Sometime we need complicate control of our analog signal.
3. **Data acquisition** This part take care of the data taking. We may collect the digital or analog signal.

Almost every operation in our system is time related, so the time sequence control

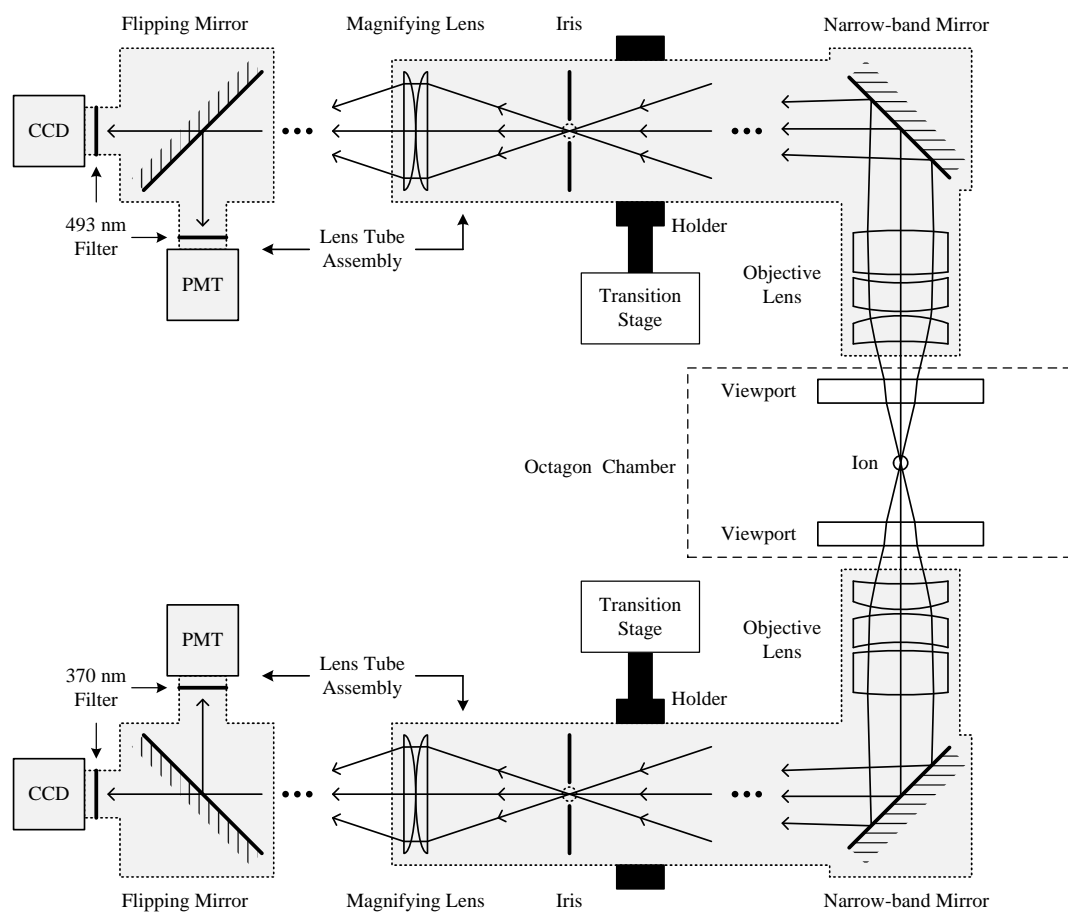


图 2.6 Image system for $^{171}\text{Yb}^+$ and $^{138}\text{Ba}^+$ ions.

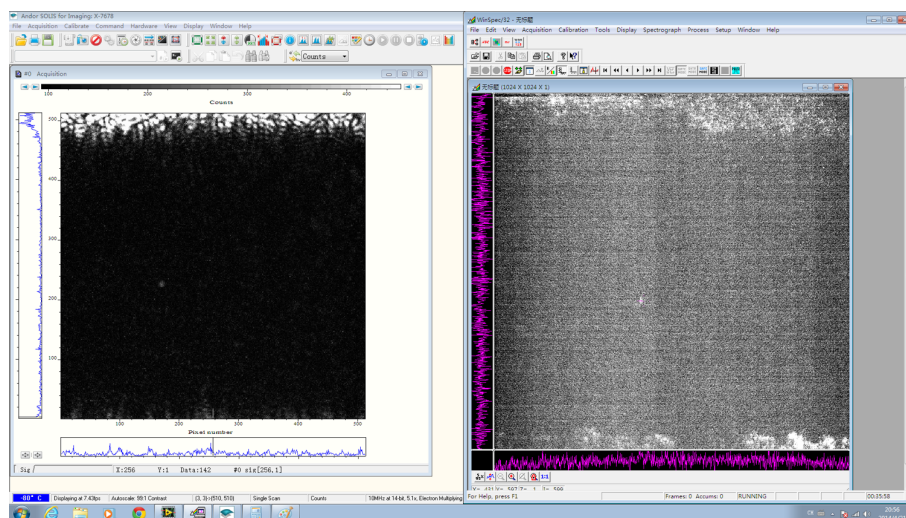


图 2.7 Camera image of two ions

is very important. We are using a Altera CycloneIII EP3C25 FPGA board designed by Dizmitry to generate TTL signals. The FPGA is referenced with a 50 MHz TTL signals generated from a arbitrary function generator referenced to the Rb clock. A PLL is used to make the clock frequency to 200MHz, which means the minimal segment duration of our system is 2 ns. We have 32 out put port, which can be used to control 32 different equipments, and 5 input port, which can collect 5 digital signal. Every single experiment sequence can last for 5497.5 s with a maximum of 7680 segments. The start time of the sequence can be controlled by the outside trigger, which can be used for line trigger method and serial connected multi FPGA boards.

We are using the same FPGA board to collect the data. In our system, the photon is almost the only signal we can detect from ion. So most of the data the TTL signal from the PMT, which can be collected by the FPGA.

Sometimes, we need to switch the frequency or phase of the signal quickly, complexly and accurately. This can not be done with the normal commercial function generator. We need to use AWG or DDS with good synchronization with FPGA. The complex altering sequence is generated by our control software.

We also make a software system to translate our intuitive representation of the experiment sequence to a machine language so that the FPGA and AWG can understand the sequence. We use Mathematica to be the top layer of our control system. We can generate the waveform and the time sequence of the experiment, translate them, then send them to the FPGA or AWG.

第3章 Single ion quantum memory

3.1 Background of quantum memory

For trapped ion qubits, in particular, hyperfine qubits, the intrinsic relaxation with time T_1 is much longer than dephasing with time T_2^* induced by the fluctuation of magnetic fields and the phase noise of the local oscillator in the experiment. The current records of single-qubit coherence time in trapped ion systems is mainly limited by not the coherence itself but the decreasing state-detection efficiency associated with the motional heating of the ion without laser cooling^[16,17]. Due to the motional heating, the wavepacket of the ion is expanding with time, which reduces the count of fluorescence photons and makes the state-discrimination inefficient^[16,17]. The motional heating of ions can be significantly suppressed by cleaning the surface of the ion-trap^[54] or locating the trap in low-temperature environment^[55]. Here, we principally eliminate the ion heating during long-time storage by the sympathetic cooling of a different species of atomic ions.

The long coherence time of a trapped ion qubit would be the essential element for practical quantum computation and quantum communication^[8,56]. The trapped ion system constitutes one of the leading candidates for the realization of large-scale quantum computers^[7]. It also provides a competitive platform for the realization of quantum networks which combines long-distance quantum communication with local quantum computation^[8]. One scalable architecture for ion-trap quantum computer is to divide the system into operation and memory zones and to connect them through ion shuttling^[23,24]. For this architecture, the basic unit of operation zone has been demonstrated^[57,58]. As the size of the system scales up, the needed storage time of the qubits in the memory zone will correspondingly increase. To keep the qubit error rates below a certain threshold for fault-tolerant computation, it is crucial to extend the coherence time of qubits. For the quantum network based on probabilistic ion-photon mapping^[59], the basic units of ion-photon and ion-ion entanglement have been demonstrated^[60–62]. The required coherence time of qubits increases in this approach as the size of the system grows.

3.2 Sympathetic cooling

When we started the experiments, it was not fully clear why more than 20 years old experiments with ensemble of ions showed much longer coherence time (around 10 min) than recent results with single ions (around 1 min at the best). We know now that the motional heating of ions degrades the capability of discriminating the qubit states, because the fluorescence of ions is reduced by motional heating. The ensemble experiments had been performed in much bigger trap, which cannot be used for quantum information processing, or with a sympathetic cooling similar to our demonstration. In the big ion trap, the motional heating from the noise of the electrodes would be a few million times smaller than those of the current typical ion-traps for the quantum information processing. In short, we believe ensemble of ions or single ions should have the equivalent coherence time. As long as the motional heating without laser cooling is managed to be suppressed, we may be able to observe similar levels of long coherence time for either ensemble qubits or single qubits. Simply before us, no one performed such sympathetic cooling for single ions to observe the long coherence time in a trap for quantum information processing.

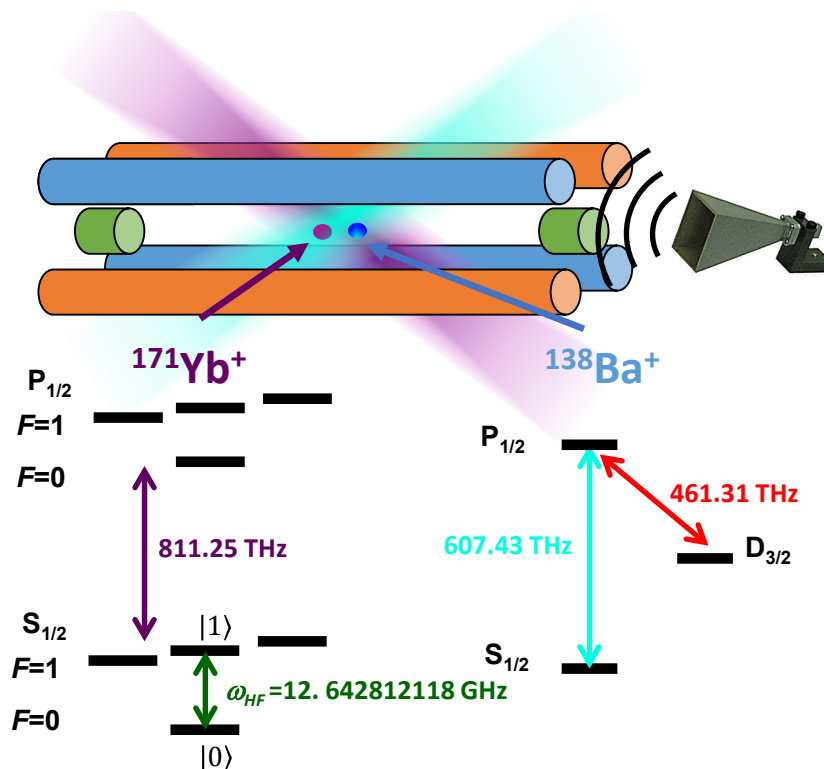


图 3.1 Schematic diagram of a trapped-ion system with two species.

In the experiment, we use two species of ions, $^{171}\text{Yb}^+$ as the qubit ion and $^{138}\text{Ba}^+$ as

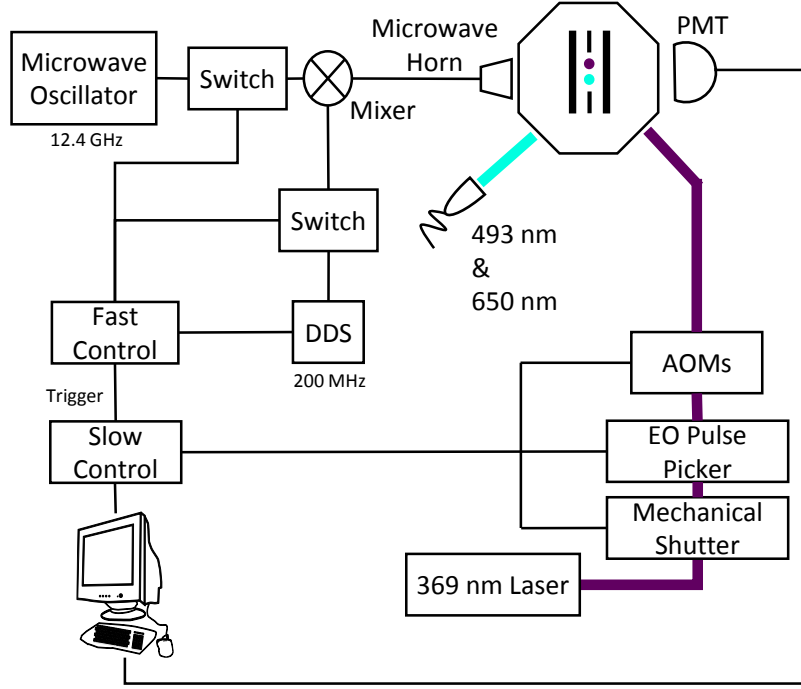


图 3.2 The microwave and laser control system.

the cooling ion, confined together in a standard Paul trap as shown in Fig. 3.1a. We choose $^{138}\text{Ba}^+$ ion as the refrigerator since it has similar mass to $^{171}\text{Yb}^+$, which makes the sympathetic cooling efficient.

3.2.1 Laser system

The two hyperfine levels of $^{171}\text{Yb}^+$ ion in the $^2S_{1/2}$ manifold are used as a qubit represented by $|\downarrow\rangle \equiv |F=0, m_F=0\rangle$ and $|\uparrow\rangle \equiv |F=1, m_F=0\rangle$, which is separated by $12642812118 + 310.8B^2$ Hz, where B is magnetic field in Gauss. In experiment, we initialize the qubit state to $|\downarrow\rangle$ by the standard optical pumping method and discriminate the state by the fluorescence detection scheme. We perform the coherent manipulation of qubit by applying the resonant microwave.

The main part of the laser system for $^{171}\text{Yb}^+$ and $^{138}\text{Ba}^+$ is introduced in the chapter 2.2.3 and chapter 2.3.3. But we need make some small modifies for the long coherence time qubit memory experiment.

The first thing we should care about is the leakage of 369nm lasers, which are the Doppler cooling, detection and pumping lasers for $^{171}\text{Yb}^+$ ion. Since the wavelength is very close to qubit transition, the little leakage of these lasers will cause huge decoherence. In the experiment, we use three stages of switches: AOMs (Acousto-Optic Modulator),

EO (Electro-Optic) pulse picker and mechanical shutter as shown in Fig. 3.2. We shut down three switches sequentially in the order of AOM, EO pulse picker and mechanical shutter.

The AOM switches is controlled by TTL signal generated by FPGA and a RF switch which has 60 dB suppression. So the AOM switches leave a few nW of laser beam leakage. If we only use AOM switches, the coherence time can only be 50 ms. The EO pulse picker provides 200 times of attenuation for the leakage which can enhance the coherence time to seconds level. To have minutes level of coherence time, we need the mechanical shutter to completely block the laser for the most of time.

We test the response time of the mechanical shutter we have, which model is ??????. The response time dependence on the hit location of the laser on the block. So the response time varies a lot from 1 ms to tens of ms. Also the response time of open and shut down is also different. After testing we decide to use 50 ms as the shutter safe time for the sequence design, which means we will open mechanical shutter 50 ms before the final detection laser. By the way, the response time of AOM and EO pulse picker is ns level, so no switching time is reserved for them. The diagram of control switches is show as Fig. 3.3

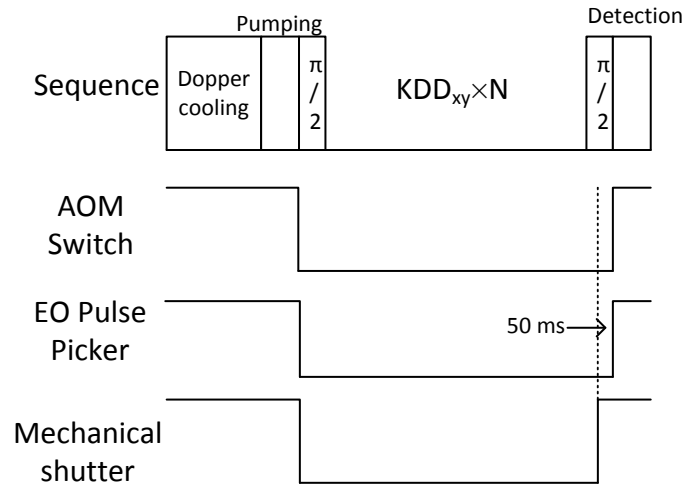


图 3.3 Time sequence of switch control. Mechanical shutter should open 50 ms before AOM and EO pulse picker.

The other thing we may carefully consider is the effect of $^{138}\text{Ba}^+$ laser on qubit ion. The Doppler cooling laser and the repumping laser for $^{138}\text{Ba}^+$ are detuned by more than 200 THz from the corresponding transitions of $^{171}\text{Yb}^+$ ion. We calculate the scattering

rate between $^2S_{1/2}$ manifold and $^2P_{1/2}$, $^2P_{3/2}$ manifold of $^{171}\text{Yb}^+$ due to the cooling laser beams, 493 nm and 650 nm, for $^{138}\text{Ba}^+$ ion. The scattering rate is calculated by the model of Raman scattering and Rayleigh elastic scattering^[63–65], which is given as

$$\Gamma_{\text{scat}} = \frac{g^2\Gamma}{6} \left(\frac{1}{\Delta_{D1}^2} + \frac{2}{(\Delta_{D1} + \Delta_{fs})^2} \right), \quad (3-1)$$

where $\Gamma \approx 2\pi \times 20$ MHz, $g = \frac{\Gamma}{2} \sqrt{\frac{I}{2I_{\text{sat}}}}$, $\Delta_{fs} \approx 2\pi \times 100$ THz. For the 493 nm laser, the parameters are as follows: laser power $P = 40 \mu\text{w}$, beam waist $\omega = 22 \mu\text{m}$, $I_{493} = 49.6I_{\text{sat}}$ and $\Delta_{D1} = 203.8$ THz, which yields a scattering rate of 2.37×10^{-6} Hz. For the 650 nm laser, the parameters are as follows: laser power $P = 10 \mu\text{w}$, beam waist $\omega = 20.7 \mu\text{m}$, $I_{650} = 14.0I_{\text{sat}}$ and $\Delta_{D1} = 349.9$ THz, which yields a scattering rate of 2.6×10^{-7} Hz. Therefore, 493 nm and 650 nm laser beams have negligible effect on the coherence of $^{171}\text{Yb}^+$ ion hyperfine qubit during hours of storage.

3.2.2 Loading $^{171}\text{Yb}^+$ and $^{138}\text{Ba}^+$ ion

We load the $^{171}\text{Yb}^+$ and $^{138}\text{Ba}^+$ simultaneously, first $^{138}\text{Ba}^+$ ion, then $^{171}\text{Yb}^+$ ion. After we have loaded the $^{138}\text{Ba}^+$ ion, we need to carefully load the $^{171}\text{Yb}^+$ ion. The process is open $^{171}\text{Yb}^+$ oven, turn on the loading laser for $^{171}\text{Yb}^+$ and observe the $^{138}\text{Ba}^+$ ion on the screen. Whenever you see the shaking of $^{138}\text{Ba}^+$ ion, you need to stop the loading of $^{171}\text{Yb}^+$ and wait. Most of the time, $^{171}\text{Yb}^+$ ion is already in the trapping potential but not fully cooled. Waiting for several minutes with strong 369 nm beam, which has 200MHz blue detune and strong power, we can see the stop of shaking and position shift of $^{138}\text{Ba}^+$ ion. We can check the $^{171}\text{Yb}^+$ image system to see it's the $^{171}\text{Yb}^+$ ion or the dark ion. We use very small current for the $^{171}\text{Yb}^+$ oven and the $^{138}\text{Ba}^+$ oven, so the total load time is always around 10 minutes.

3.2.3 Cooling effect

At the time for this experiment, we haven't develop the 1.7 μm laser or the Raman laser system. So we don't have a good way to measure the temperature of this ion chain with sympathetic cooling. We observe that the hopping happens every 5 minutes and the ions are never gone with the $^{138}\text{Ba}^+$ cooling laser on. During the data taking process, we can have the ions more than one week. (Theoretical calculation?)

Because of the hopping, the position of $^{171}\text{Yb}^+$ sometime changes. We need to make

sure about that the detection and pumping effect is same at two position. So we need align these two laser with single $^{171}\text{Yb}^+$ ion first. Then check with the $^{171}\text{Yb}^+$ and $^{138}\text{Ba}^+$ ion chain.

Due to the hopping, we need to check the homogeneousness of the magnetic and microwave field. We use Ramsey measurement to measure the qubit transition for two position. We can't see any different within 1 Hz level.(Without dynamical decoupling, we can have around 800 ms of coherence time, which gives us the measure resolution around 1.2 Hz.) The distance between two ions is three orders of magnitude smaller than the wavelength of the operational microwave. The microwave field is quite homogeneous in this small area.

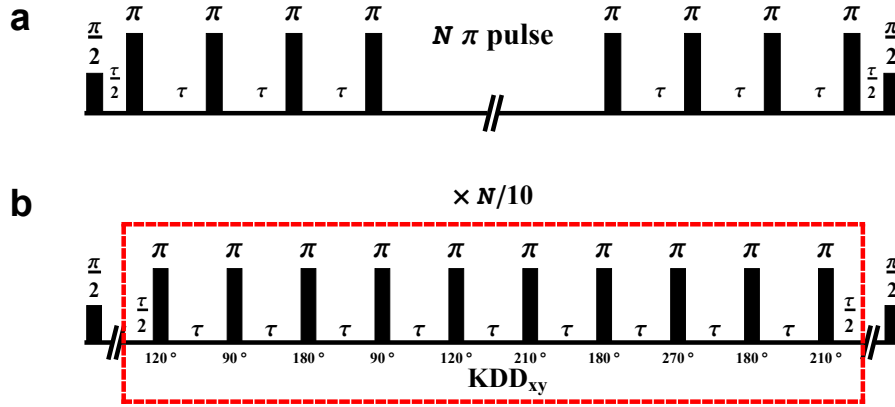
3.3 Dynamical decoupling

3.3.1 Introduction

With the help of sympathetic cooling, the remaining dominant factor of decoherence is the magnetic field fluctuation and the phase noise of the qubit operational microwave, which leads to phase randomization^[19]. We can write the Hamiltonian of the qubit system as $H = \frac{\hbar}{2}(\omega_0 + \beta(t))\sigma_z$, where ω_0 is the splitting of the qubit, $\beta(t) = \beta_B(t) + \beta_{LO}(t)$ is the random phase noise that consists of the magnetic field fluctuation β_B and the phase noise β_{LO} of the qubit operational microwave^[66], σ_z is the Pauli operator. The accumulation of the random phase causes dephasing of the qubit state.

A standard technique to preserve the qubit coherence against random phase noise is dynamical decoupling, which consists of multiple spin-echo pulses^[14,15,18-22]. Since the performance of the sequence is sensitive to the characteristics of noise environment, we study the noise spectrum of our system, which guides us to choose the proper dynamical decoupling pulses.

The dynamical decoupling sequence we used in the experiment is CPMG (Carr, Purcell, Meiboom and Gill)^[22] and KDD_{xy} ^[15,21]. The diagram of this two sequence is shown if the Fig. 3.4. For the CPMG sequence, all the π pulses have the same phase of $\pi/2$. Interval between every π pulses is τ . And the KDD_{xy} sequence consist of the Knill pulse, which consists of five π pulses with angles $\phi + \pi/6, \phi, \phi + \pi/2, \phi, \phi + \pi/6$. The KDD_{xy} consists of two Knill pulses equally spaced with $\phi = \pi/2$ and $\phi = \pi$. We apply $N/10$ sets of the KDD_{xy} , which leads to the total number of N pulses. Note that N should be a multiple of 20 to form an identity operation^[21].


 图 3.4 Diagram of CPMG and KDD_{xy}

3.3.2 Calculation of the filter function

To calculate the evolution under arbitrary dynamical decoupling sequence, we use the unitary transformation to describe our rotation. Because all the rotation axis we used is in xy -plane. We can write rotation as

$$\begin{aligned} D_\phi(\gamma) &= D_z(\phi)D_x(\gamma)D_z(-\phi) \\ &= e^{-\frac{i}{2}\sigma_z\phi} e^{-\frac{i}{2}\sigma_x\gamma} e^{\frac{i}{2}\sigma_z\phi} \end{aligned} \quad (3-2)$$

where ϕ is the angle between rotating axis and x axis, γ is the rotating angle along the axis. In dynamical decoupling sequence, γ is always π , $D_x(\pi) = \cos(\pi/2) + i\sigma_x \sin(\pi/2) = i\sigma_x$. Below we will use σ_x only because the factor i is an irrelevant global phase shift.

We start from initial state $|\psi(0)\rangle = |\downarrow\rangle$. We apply a $\pi/2$ pulse to rotate state in xy -plane. Then we apply dynamical decoupling sequence. After this, we apply another $\pi/2$ and measure Ramsey fringe contrast. Meanwhile, state is evolve under the noise influence. The final state is show as

$$|\psi(T)\rangle = D_x(\pi/2)\tilde{R}(T)D_x(\pi/2)|\psi(0)\rangle \quad (3-3)$$

$$\tilde{R}(T) = e^{-i\sigma_z \int_{T\delta_n}^T \beta(t)dt} D_{\phi_n}(\pi) \cdots D_{\phi_2}(\pi) e^{-i\sigma_z \int_{T\delta_1}^T \beta(t)dt} D_{\phi_1}(\pi) e^{-i\sigma_z \int_{T\delta_0}^T \beta(t)dt} \quad (3-4)$$

which $\tilde{R}(T)$ is the evolution during total time T , N is the total number of π pulse, T_i is the application time of the i th π pulse, $T_0 = 0$, $T_{n+1} = T$, ϕ_i is the phase of i th π pulse. We expand $D_\phi(\gamma)$ in Eq. 3-4 to have

$$\tilde{R}(T) = e^{-i\sigma_z \int_{T_N}^{T_{N+1}} \beta(t)dt} e^{-i/2\sigma_z\phi_N} \sigma_x e^{i/2\sigma_z\phi_N}$$

$$\begin{aligned}
 & e^{-i\sigma_z \int_{T_{N-1}}^{T_N} \beta(t) dt} e^{-i/2\sigma_z \phi_{N-1}} \sigma_x e^{i/2\sigma_z \phi_{N-1}} e^{-i\sigma_z \int_{T_{N-2}}^{T_{N-1}} \beta(t) dt} \\
 & \dots e^{-i\sigma_z \int_{T_1}^{T_2} \beta(t) dt} e^{-i/2\sigma_z \phi_1} \sigma_x e^{i/2\sigma_z \phi_1} e^{-i\sigma_z \int_{T_0}^{T_1} \beta(t) dt}
 \end{aligned} \tag{3-5}$$

$$\begin{aligned}
 & = e^{-i\sigma_z (\int_{T_N}^{T_{N+1}} \beta(t) dt + \phi_N/2)} \sigma_x e^{-i\sigma_z (\int_{T_{N-1}}^{T_N} \beta(t) dt - \phi_N/2 + \phi_{N-1}/2)} \\
 & \dots e^{-i\sigma_z (\int_{T_1}^{T_2} \beta(t) dt - \phi_2/2 + \phi_1/2)} \sigma_x e^{-i\sigma_z (\int_{T_0}^{T_1} \beta(t) dt - \phi_1/2)}
 \end{aligned} \tag{3-6}$$

Normally n is even for dynamical decoupling. Since only σ_x flip the spin in $\tilde{R}(T)$. We can have

$$\tilde{R}(T) |\downarrow\rangle = e^{-iF_N(T)} |\downarrow\rangle \tag{3-7}$$

$$\tilde{R}(T) |\uparrow\rangle = e^{iF_N(T)} |\uparrow\rangle \tag{3-8}$$

$$\tilde{R}(T) = e^{iF_N(T)\sigma_z} \tag{3-9}$$

which

$$\begin{aligned}
 F_N(T) & = -\left(\int_{\delta_0 T}^{\delta_1 T} \beta(t) dt - \phi_1/2\right) + \left(\int_{\delta_1 T}^{\delta_2 T} \beta(t) dt - \phi_2/2 + \phi_1/2\right) \\
 & -\left(\int_{\delta_2 T}^{\delta_3 T} \beta(t) dt - \phi_3/2 + \phi_2/2\right) + \dots + (-1)^n \left(\int_{\delta_{n-1} T}^{\delta_n T} \beta(t) dt - \phi_n/2 + \phi_{n-1}/2\right) \\
 & + (-1)^{n+1} \left(\int_{\delta_n T}^{\delta_{n+1} T} \beta(t) dt + \phi_n/2\right)
 \end{aligned} \tag{3-10}$$

$$= \sum_{i=0}^n (-1)^{i+1} \int_{\delta_i T}^{\delta_{i+1} T} \beta(t) dt + \sum_{i=1}^n (-1)^{i+1} \phi_i \tag{3-11}$$

So we can have $|\psi(T)\rangle = e^{iF_N(T)\sigma_z} |\psi(0)\rangle$. For normal dynamical decoupling, like CPMG, XY-16 and KDD_{xy}, we may have $\sum_{i=1}^n (-1)^{i+1} \phi_i = k\pi$, which k is an integer. That means $\sum_{i=1}^n (-1)^{i+1} \phi_i$ can only donate a global phase in the evolution. So we can ignore this term. We can have

$$F_N(T) = \sum_{i=0}^n (-1)^{i+1} \int_{\delta_i T}^{\delta_{i+1} T} \beta(t) dt \tag{3-12}$$

$$\equiv \int_{-\infty}^{\infty} s_N(t') \beta(t') dt' \tag{3-13}$$

which

$$s_N(t') = \begin{cases} 0 & \text{for } t' \leq 0, \\ (-1)^j & \text{for } \delta_j T < t' \leq \delta_{j+1} T \\ 0 & \text{for } t' > T \end{cases} \quad (3-14)$$

According to Eq. 3-9, the signal we measured is^[67]

$$\begin{aligned} \langle \psi(T) | \sigma_z | \psi(T) \rangle &= \langle \psi(0) | D_x(\pi/2)^\dagger R(\tilde{T})^\dagger D_x(\pi/2)^\dagger \sigma_z D_x(\pi/2) R(\tilde{T}) D_x(\pi/2) | \psi(0) \rangle \\ &= \langle \cos(2F_n(T)) \rangle \end{aligned} \quad (3-15)$$

$$\approx e^{2\langle F_n(T)^2 \rangle} \quad (3-16)$$

If we assume the noise as the continuously model, which can be described by noise spectrum $S_\beta\omega$. The Fourier transform of $s_N(t')$ is given by $\tilde{y}(\omega, T)$

$$\tilde{y}(\omega, T) = \int_{-\infty}^{\infty} s_n(t') e^{i\omega t'} dt' \quad (3-17)$$

$$= \frac{1}{\omega} [1 + (-1)^{n+1} e^{i\omega T} + 2 \sum_{j=1}^n (-1)^j e^{i\delta_j \omega T}] \quad (3-18)$$

So $\langle F_n(T)^2 \rangle$ is written in

$$\langle F_n(T)^2 \rangle = \int_{-\infty}^{\infty} \int_{-\infty}^{\infty} dt_1 dt_2 s_n(t_1) s_n(t_2) \langle f(t_1) f(t_2) \rangle \quad (3-19)$$

$$= \frac{1}{\pi} \int_{-\infty}^{\infty} S_\beta(\omega) |\tilde{y}(\omega T)|^2 d\omega \quad (3-20)$$

So we can write the signal we measure as $e^{-\chi(T)}$, which

$$\chi(T) = \frac{2}{\pi} \int_0^{\infty} S_\beta(\omega) |\tilde{y}(\omega, T)|^2 d\omega. \quad (3-21)$$

Here we consider $|\tilde{y}(\omega, T)|^2$ as a frequency domain filter for $S_\beta(\omega)$. We call $|\tilde{y}(\omega, T)|^2$ the filter function.

If we assume the noise as the discrete model, which can be described by $\tilde{\beta}(\omega) =$

$\sum_{k=1}^d \beta_k \delta(\omega - \omega_k)$, where β_k is the strength of the noise. The signal we measure is^[20]

$$\langle \cos(2F_N(T)) \rangle = \prod_k^d J_0(|\beta_k \tilde{y}(\omega_k, T)|), \quad (3-22)$$

where J_0 is the 0th of Bessel function, $\tilde{y}(\omega, T) = \frac{1}{\omega} \sum_{j=0}^N (-1)^j [e^{i\omega T_j} - e^{i\omega T_{j+1}}]$.

Especially, we find KDD_{xy} and CPMG have the same filter function.

3.3.3 Filter function of CPMG and KDD

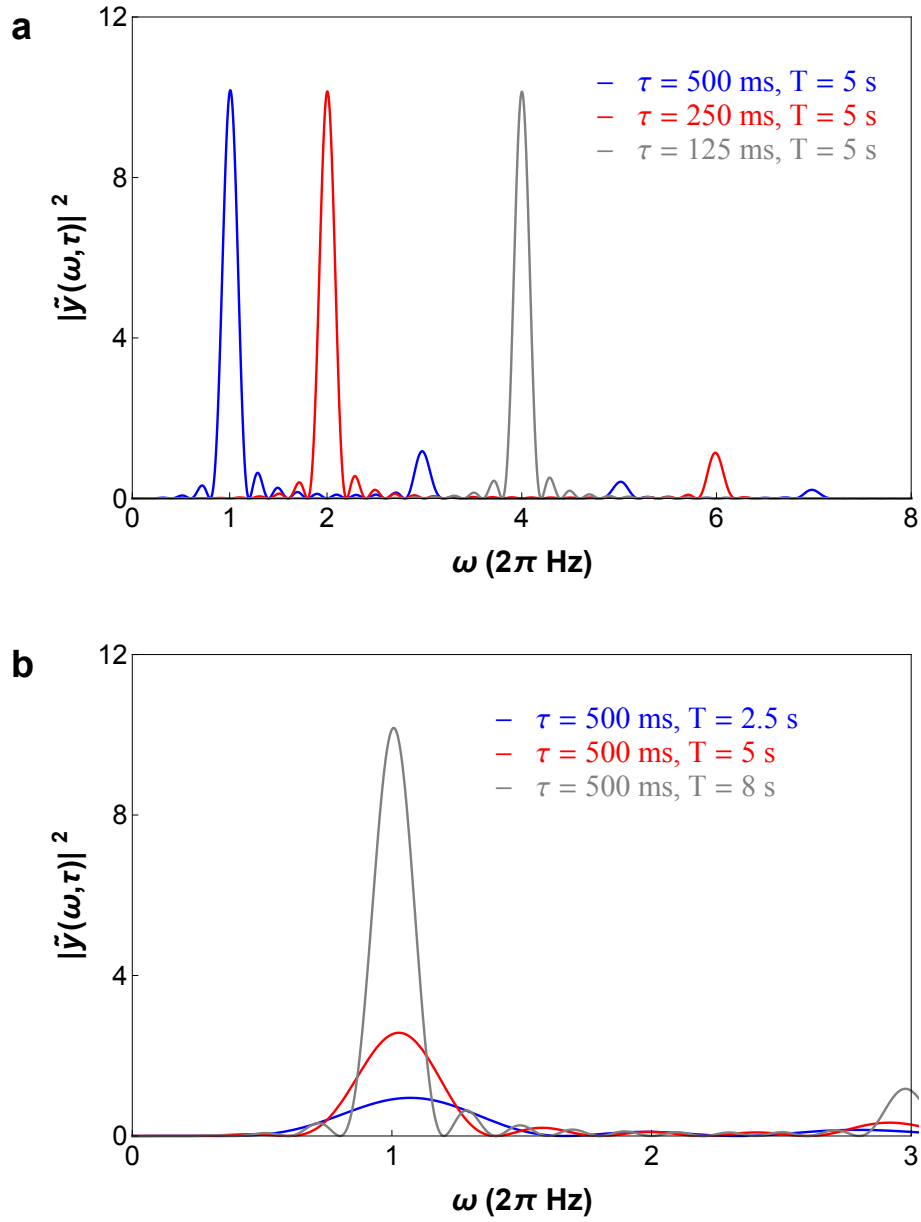


图 3.5 Filter function

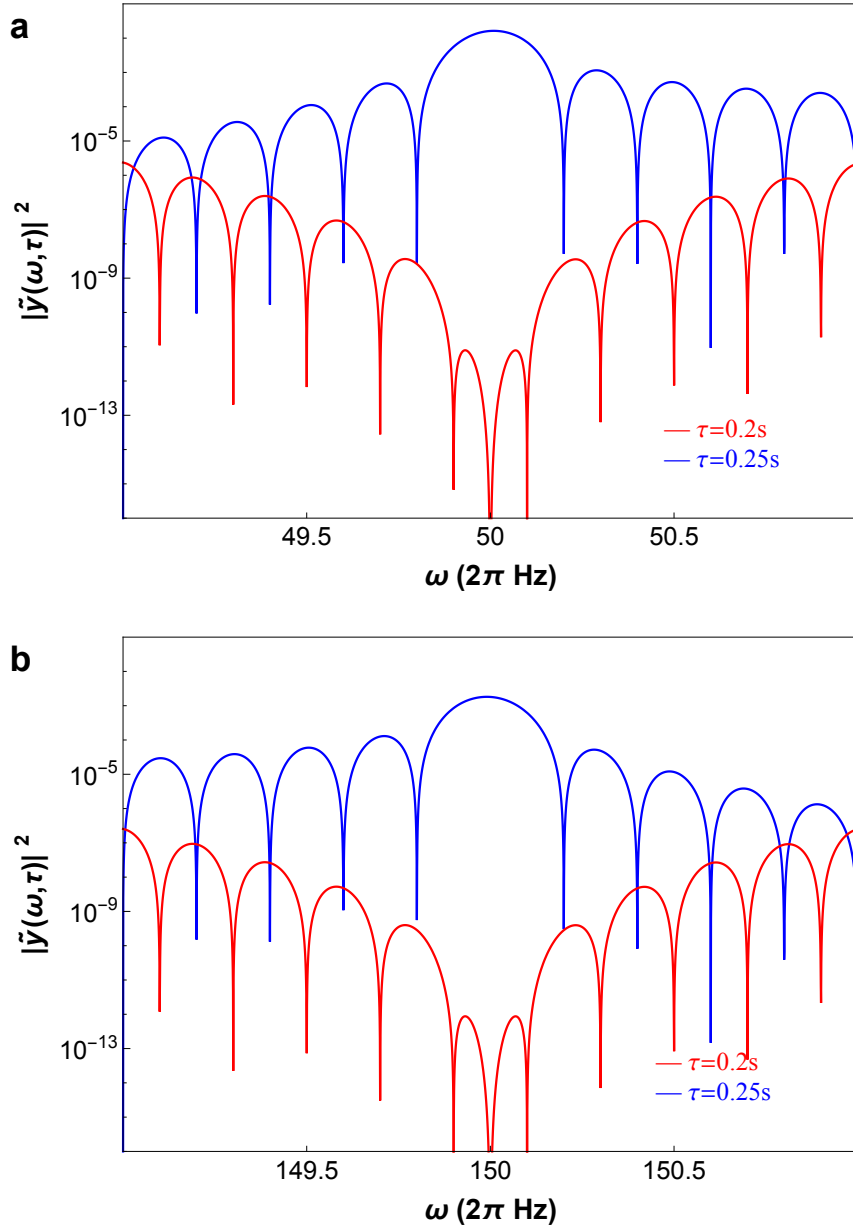


图 3.6 Filter function

As we mentioned, KDD_{xy} and CPMG have the same filter function. Let's see what's the filter function $\tilde{y}(\omega, T)$ looks like for CPMG. According to Eq. 3-18

$$\tilde{y}(\omega, T) = \int_{-\infty}^{\infty} s_n(t') e^{i\omega t'} dt' \quad (3-23)$$

$$= \frac{1}{\omega} [1 + (-1)^{N+1} e^{i\omega T} + 2 \sum_{j=1}^N (-1)^j e^{i\delta_j \omega T}], \quad (3-24)$$

We take in the parameter with $\delta_0 = 0$, $\delta_1 = T/2N$, $\delta_2 = 3T/2N$, ... $\delta_N = (2N - 1)T/2N$,

$\delta_{N+1} = T$, $\tau = T/N$ and even number N for CPMG. This can simplify the filter function as

$$\tilde{y}(\omega, T) = (1 + e^{i\omega T}) \frac{(1 + e^{i\omega T/(2N)})^2}{1 + e^{i\omega T/N}}, \quad (3-25)$$

According to 3-29, $|\tilde{y}(\omega, T)|^2$ determine the suppression effect of dynamical decoupling on the environment noise. We can calculate $|\tilde{y}(\omega, T)|^2$ as shown in Fig. 3-18. We notice that the function $|\tilde{y}(\omega, T)|^2$ is similar to a band pass filter with the center frequency of $\frac{1}{2\tau}$ (Shown in Fig. 3.5a) and the width proportional to $\frac{1}{2\pi T}$ (Shown in Fig. 3.5b)

By the calculation, we can also see the suppression for some specify frequency, like 50 Hz and its harmonics coming from the power line, which is the dominant components of noise. For example, Fig. 3.6a and b shows the filter function near 50 Hz and 150 Hz. The red curve is the filter function with interval $\tau = 200$ ms and the blue curve is the filter function with interval $\tau = 250$ ms. You can see red value is around 10 orders of magnitude lower than the blue value near 50 Hz and 150 Hz. So we may choose $\tau = 200$ ms instead of 250 ms to suppress the 50 Hz and 150 Hz noise.

3.3.4 Environment noise

As we mentioned, the remaining dominant factor of decoherence is the magnetic field fluctuation and the phase noise of the qubit operational microwave. We can write the Hamiltonian of the qubit system as $H = \frac{\hbar}{2}(\omega_0 + \beta(t))\sigma_z$, where ω_0 is the splitting of the qubit, $\beta(t) = \beta_B(t) + \beta_{LO}(t)$ is the random phase noise that consists of the magnetic field fluctuation β_B and the phase noise β_{LO} of the qubit operational microwave^[66], σ_z is the Pauli operator. We need to study the noise spectrum of our system, which guides us to choose the proper dynamical decoupling pulses. $\beta_{LO}(t)$ is related to the local oscillator quality. We use our best Agilent source referenced to a Rb clock and DDS to generate the operational microwave, whose phase noise is measured by Agilent PXA spectrum analyzer shown in Fig. 3.7.

We can hardly adjust $\beta_{LO}(t)$, but we can easily adjust $\beta_B(t)$. We consider the second order Zeeman effect of the $^{171}\text{Yb}^+$ qubit transition^[31] is described by $\Delta f_{2OZ} = K\langle B^2 \rangle$ Hz, $K = 310.8$ Hz/G². In the Hamiltonian $H = \frac{\hbar}{2}(\omega_0 + \beta_B(t) + \beta_{LO}(t))\sigma_z$, where ω_0 and $\beta_B(t)$ are given by

$$\omega_0 = \omega_{\text{HF}} + K(B_x^2 + B_y^2 + B_z^2), \quad (3-26)$$

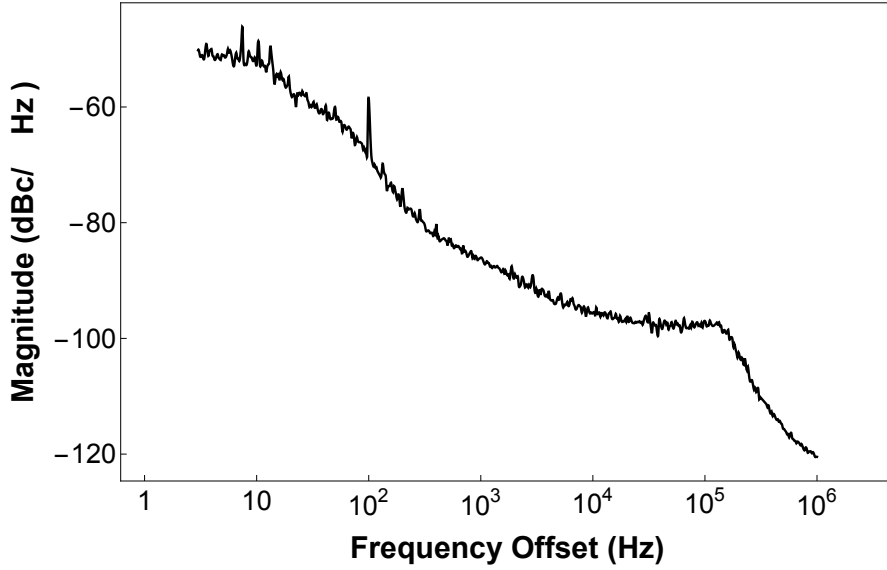


图 3.7 Phase noise measured by Agilent PXA spectrum analyzer

$$\begin{aligned} \beta_B(t) = & K(2B_x\langle b_x(t) \rangle + 2B_y\langle b_y(t) \rangle + 2B_z\langle b_z(t) \rangle \\ & + \langle b_x(t)^2 \rangle + \langle b_y(t)^2 \rangle + \langle b_z(t)^2 \rangle), \end{aligned} \quad (3-27)$$

and ω_{HF} is the hyperfine splitting, B_x, B_y, B_z represent the average values of the magnetic field in three directions and $b_x(t), b_y(t), b_z(t)$ describe fluctuations in the corresponding directions. The fluctuations come from mainly the surrounding electronics and environment, not much from the current sources generating the magnetic field. Therefore, we can simply assume the reducing average magnetic-field B does not increase the fluctuations $b_x(t), b_y(t), b_z(t)$. Thus we can use smaller B to obtain smaller $\beta(t)$, thereby archiving longer coherence time. Since $b_x(t)$ is much smaller than $b_y(t)$ and $b_z(t)$ according to the flux gauge measurement, we put the magnetic field along x-axis. In the experiment, we set $B_z = 0, B_y = 0$ and $B_x = 3.5$ G, which is the smallest magnetic field strength to maintain detection efficiency in our system. To study noise spectrum of our system, we use the setting of $B_z = 0, B_y = 0$ and $B_x = 8.8$ G.

In our system, the dominant components of noise are at 50 Hz and its harmonics coming from the power line, which is modeled as the sum of discrete noises $\tilde{\beta}(\omega) = \sum_{k=1}^d \beta_k \delta(\omega - \omega_k)$. Here β_k is the strength of the noise. The Ramsey contrast of the final state becomes^[20]

$$\langle \cos(2F_N(T)) \rangle = \prod_{k=1}^d J_0(|\beta_k \tilde{y}(\omega_k, T)|), \quad (3-28)$$

where J_0 is the 0th of Bessel function, $\tilde{y}(\omega, T) = \frac{1}{\omega} \sum_{j=0}^N (-1)^j [e^{i\omega\tau_j} - e^{i\omega\tau_{j+1}}]$, $\tau_0 = 0$, $\tau_{N+1} = T$. With 31 CPMG pulses, the resultant coherence as a function of the pulse interval is shown in Fig. 3.8. By fitting, we obtain the discrete noise spectrum as $B_{50\text{Hz}} = 18.3 \mu\text{G}$, $B_{150\text{Hz}} = 57.5 \mu\text{G}$ with no significant components at other frequencies.

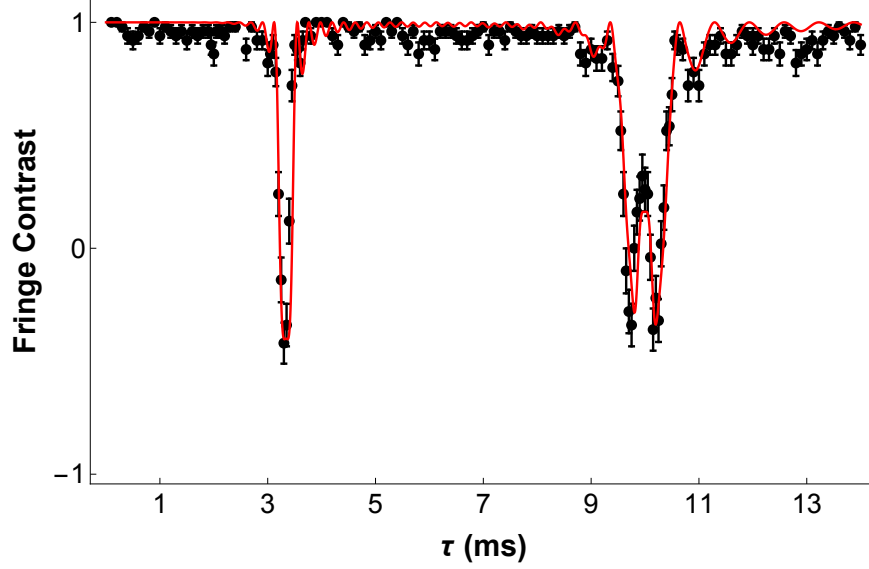


图 3.8 Measured result and fitting result for 50 Hz and 150 Hz

We further study the rest of the noise spectrum by using the continuous noise model. Given an arbitrary noise spectrum $S_\beta(\omega)$, the Ramsey contrast is given by $e^{-\chi(T)}$, where $\chi(T)$ is written as^[19]

$$\chi(T) = \frac{2}{\pi} \int_0^\infty S_\beta(\omega) |\tilde{y}(\omega, T)|^2 d\omega. \quad (3-29)$$

As we showed in the last section, the function $|\tilde{y}(\omega, T)|^2$ can be viewed as a bandpass filter with the center frequency of $\frac{1}{2\tau}$ and the width proportional to $\frac{1}{2\pi T}$, where τ is the pulses interval. We have some way to estimate the $S_\beta(\omega)$ by measure the $\chi(T)$.

According to Eq. 3-18, we know $\tilde{y}(\omega, T)$ is the the Fourier transform of $s_N(t')$. Based on Plancherel theorem, we know

$$\int_{-\infty}^\infty |s_N(t')|^2 dt' = \frac{1}{2\pi} \int_{-\infty}^\infty |\tilde{y}(\omega, T)|^2 d\omega \quad (3-30)$$

Connect with Eq. 3-14, we know $\int_{-\infty}^{\infty} |s_N(t')|^2 dt' = T$. So

$$\int_{-\infty}^{\infty} |\tilde{y}(\omega, T)|^2 d\omega = 2\pi T \quad (3-31)$$

If we assume $S_\beta(\omega)$ is flat in the area near $\omega = 1/(2\tau)$, we can estimate

$$S_\beta(1/(2\tau)) \approx \chi(T)/(4T) \quad (3-32)$$

This is the way we estimate $S_\beta(\omega)$. As shown in Fig. 3.9a, we observe the Ramsey contrasts depending on the total evolution time T with various total number of CPMG pulses as $N = 2, 10, 100, 500, 400, 6000$ and 10000 . Because we have some gate error, the data are normalized to the contrast of the data of the same number of pulses without waiting times. Applying Eq. (3-32) to the results of Fig. 3.9, we obtain $S_\beta(\omega)$ as shown in Fig. 3.9b. We observe sharp increase of noise strength below $(2\pi) 2$ Hz, which is consistent with the result of flux gauge measurement. We also observe slow increase of the noise above $(2\pi) 100$ Hz, which comes from the phase noise of the operational microwave^[66].

In order to extend coherence time with the CPMG type of sequence under our current noise environment, we carefully choose the interval of the pulse sequence. We can locate the bandpass frequency between 2 Hz and 100 Hz, where the noise spectrum has lowest value, which means $5 < \tau < 250$ ms. In this range, a larger τ is preferred, which reduces the number of pulses and leads to smaller accumulation of gate errors. We choose the pulse interval τ properly so that the noise components at 50 Hz and 150 Hz are suppressed to a negligible level. Considering all the factors, the optimal $\tau = 200$ ms.

3.3.5 Slow magnetic field drifting

3.4 Microwave gate

We use microwave to drive the qubit transition. Microwave is generated by mixing a fixed 12.442812 GHz signal from an Agilent microwave oscillator and the signal around 200 MHz signal from a DDS (Model is AD9910). After amplified by one amplifier, we use a horn placed near one viewport to apply the microwave. The microwave gate fidelity is one of the most important factor to realize a long time quantum memory since the dynamical decoupling may need thousands of gates. The gate error will cause the

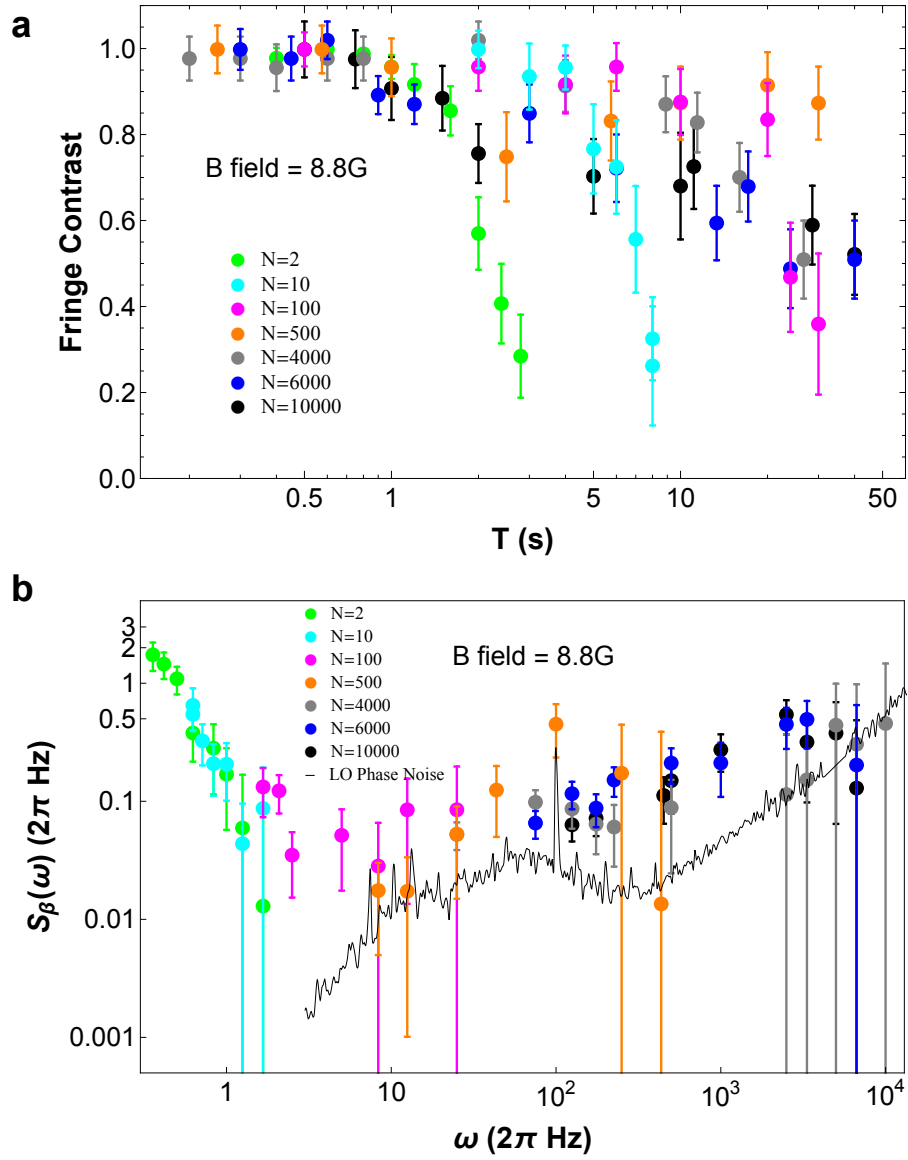


图 3.9 Ramsey contrasts $\langle \cos(2F_N(T)) \rangle$ depending on the total evolution time for various numbers of pulses.

decoherence and lose of the Ramsey contrast. Actually, we do a lot of check to guarantee we have a good microwave gate.

3.4.1 Control of DDS

We are using the AD9910 evaluation board, which is a 1 GSPS DDS with a 14-bit DAC, to generate the 200MHz signal. The evaluation board has one filtered output port, one reference clock port and the USB port for communication with computer. We use a 1 GHz signal generated by an Agilent microwave oscillator to be the reference. We use the software provided by Analog Devices to set the initial parameter. AD9910 can have 8 different profile, which can be choose and switched in 100 clock cycle. This function is very good for the composite gate we may use in dynamical decoupling since we can change the phase very fast and accurate.

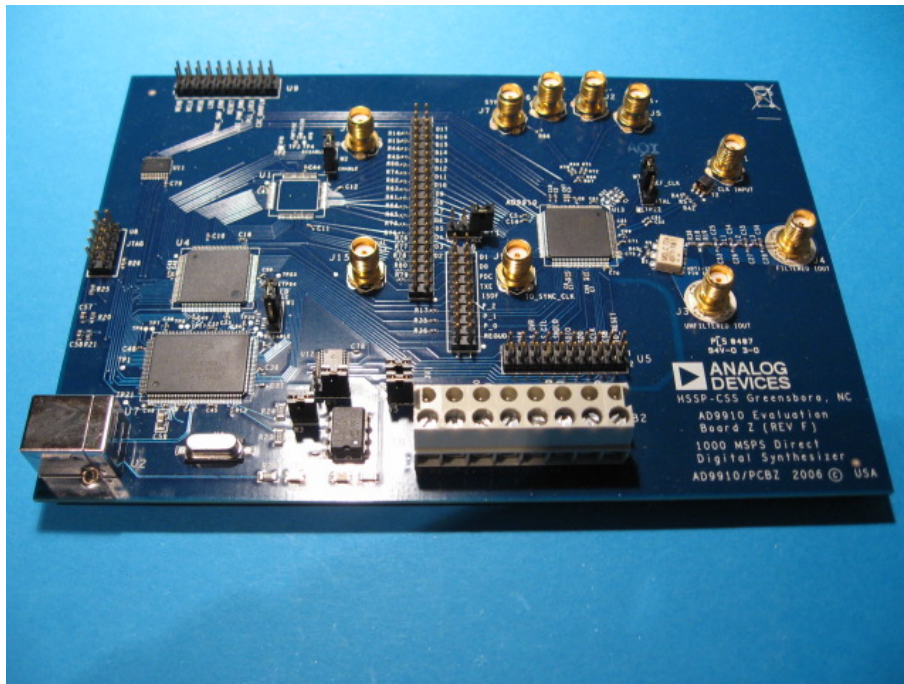


图 3.10 AD9910 evaluation board

We are using the Knill pulse^[15,21] to composite the flip error and phase error of the microwave gate. The Knill pulse consist of five π pulses with angles $\phi + \pi/6, \phi, \phi + \pi/2, \phi, \phi + \pi/6$. The KDD_{xy} consists of two Knill pulses equally spaced with $\phi = \pi/2$ and $\phi = \pi$. So actually we need 5 different phases for KDD_{xy} , which is $\pi/2, 2\pi/3, \pi, 7\pi/6$ and $3\pi/2$. We also need the π pulse with phase 0. We need 6 different phases π pulse. Beside these 6 profile, we need one profile for the totally shutting the 200MHz signal.

表 3.1 DDS Profile

| Number | Profile [2:0] | Phase | Amplitude |
|--------|---------------|----------|-----------|
| 1 | 000 | 0 | 0 |
| 2 | 001 | 0 | 1 |
| 3 | 010 | $\pi/2$ | 1 |
| 4 | 011 | $2\pi/3$ | 1 |
| 5 | 100 | $3\pi/2$ | 1 |
| 6 | 101 | $7\pi/6$ | 1 |
| 7 | 110 | π | 1 |

If we only use one switch on the RF side or the microwave side in the Fig. 3.2 without totally shutting, the leakage of the signal will slowly drive the qubit transition, which is observed in the experiment. So we need 7 profile total, which is perfect matched with AD9910 chip.

We use the software to set the 7 profile and a particular profile is activated by providing the appropriate logic levels to the profile control pins. The switch time for profiles is less than 100ns. We connect this three pins to the C6 (Porfile[0]), C7 (Porfile[1]) and C8 (Porfile[2]) port of FPGA. The profile setting is shown in the below Table. 3.1.

One of the importance thing is the trigger missing for the profile pin. The trigger missing is because of the arriving time different with different profile pin. For example, if we want to change the profile from 000 to 011 and change the C6 and C7 in the same time with FPGA, the C6 signal may arrive to Profile[0] a little bit earlier than C7 to Profile[1]. Sometimes, this will cause chip change the profile from 000 to 001 and ignore the Profile[1] signal. This will introduce some mistake in the phase control of DDS, affect the gate fidelity and dynamical decoupling effect. So if we really want to guarantee the profile changing from 000 to 011, we should separate it into two steps: 000 \rightarrow 001 \rightarrow 011.

3.4.2 DDS performance

3.4.3 Random benchmarking test

We want to check the single qubit gate fidelity of our system. We see a very clean Rabi oscillation with our microwave gate even after 100 periods as shown in the Fig. 3.11. We adjust the power of the microwave signal, to make the π time around 40 μ s. We simply

check the gate quality with seeing the population with 1 π gate, the average population is around 98.5%. But this is not the gate fidelity, because the detection efficiency and pumping efficiency involved. We use the random benchmarking method to test the gate fidelity^[68].

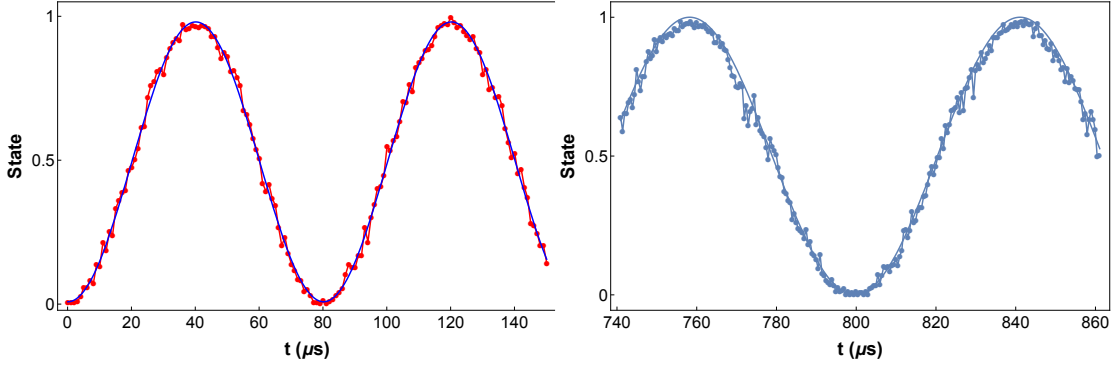


图 3.11 Rabi oscillation till 100 period

To make the random benchmarking test of our single qubit gate, we need to generate some random sequence of either major axis π pulses or identity operators (“Pauli randomization”) and $\pi/2$ pulses (“computational gates”). The Pauli randomization is the form of $e^{\pm i\sigma_b\pi/2}$, where the sign \pm and $b = 0, x, y, z$ are randomly chosen uniformly. The computational gates are $\pi/2$ pulses in the form $e^{\pm i\sigma_u\pi/4}$, where $u = x, y$. Also the sign and the u are chosen uniformly. In our microwave gate system, it’s easy to control the phase of DDS as we mentioned, so it is easy to realize the $e^{\pm i\sigma_b\pi/2}$ with $b = 0, x, y$ and $e^{\pm i\sigma_u\pi/4}$ with $u = x, y$. For the σ_z axis rotation, we consider it as a perfect rotation in the experiment with some global phase.

We generated $N_G = 4$ random computational sequences and truncated them to the $N_l = 15$ lengths $\{2, 5, 10, 25, 40, 60, 80, 100, 150, 200, 250, 300, 350, 400, 500\}$. Each truncated sequence was Pauli randomized $N_P = 8$ times. Each final pulse sequence was applied to an ion a total of 500 times. As shown in the Fig. 3.12, there are 32 points for each number of steps, corresponding to $N_P=8$ randomizations of each of $N_G = 4$ different computational sequences. We used $N_e = 500$ for these experiments. Different symbols are used for the data for each computational sequence.

As shown in the Fig. 3.13, the points show the average randomized fidelity for four different computational gate sequences. The fit was consistent with a simple exponential decay, which suggests that these gates behave similarly in all computational contexts. The error bars represent standard deviation. Our single qubit gate fidelity is measured to be

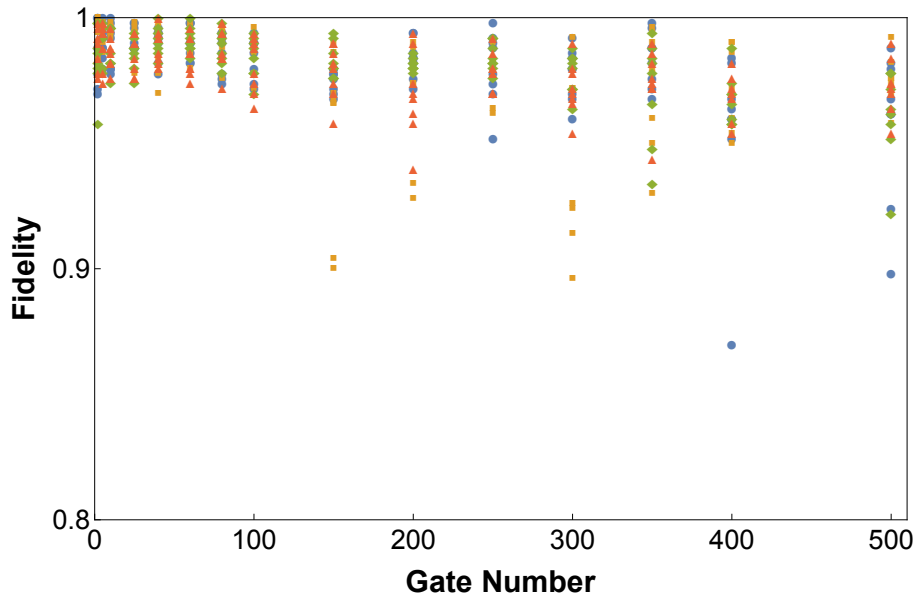


图 3.12 Fidelity as a function of the number of steps for each randomized sequence.

$99.994 \pm 0.002\%$.

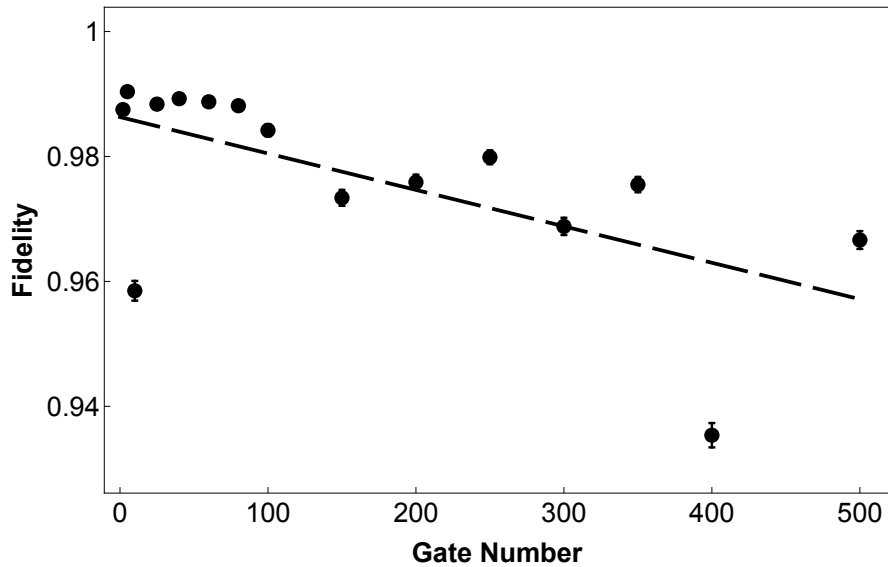


图 3.13 Average fidelity as a function of the number of steps for each computational sequence.

3.5 Control system and Data taking

It is very painful to take this kind of very long time data, especially when your system is not stable enough. In the normal ion trap system experiment, like the random benchmarking test, we write the sequence into our control FPGA, let the system repeat hundreds of time and readout the average population of final state. This process always

takes second-level time, which is comparatively short for the stable time of our system. But in this experiment, the single shot of one data point may need minutes of time, so we need to limit the repeat time for one round.

The other issue is the memory problem for our FPGA. We are using Cyclone III FPGA chip. The memory bits inside the chip is 608256 bits. Besides the register for the system, we can use 552960 bits for the sequence storage. Each sequence segment need 72 bits to store the duration information. So we can only have 7680 segments with one FPGA. Unfortunately, we set the interval $\tau = 200$ ms. We need 3000 pulses, each pulse need 2 or 3 segments because of the issue discussed in the Chapter 3.4.1, to achieve 10 minutes of experiment time and we have interval between pulses. So it is not possible to use only one FPGA to realize this 10 minutes experiment. We may use two FPGA serially connected to control the whole system.

3.5.1 FPGA control system

We used two FPGA together to control the whole system, as shown in Fig. 3.2. Two FPGAs are synchronized in less than 10 ps of time jitter. The first FPGA control the timing of laser switch, including the Doppler cooling laser, pumping laser and the final stage of the detection laser. It control the DDS to make the first and the final $\pi/2$ pulse. It also send the trigger to the second FPGA, this trigger set the starting time of a certain period of KDD_{xy} . The second FPGA control the two switches for microwave and DDS, the DDS signal phase through the profile pins, so that the mixed signal can realize the certain period of KDD_{xy} . For example, we want to apply 3000 pulses of KDD_{xy} . We divide 3000 pulses into 5 part, each part has 600 pulses. We use the first FPGA send 5 triggers at the beginning time of each part. We write the sequence for 600 KDD_{xy} sequence with interval $\tau = 200$ ms into the second FPGA. Every time the second FPGA receive the trigger, it will control the DDS to apply 600 KDD_{xy} pulses. This can realize 3000 pulses with our certain FPGA board. The time diagram is shown in the Fig. 3.14

3.5.2 One shot data taking

One distinction between single qubit system and ensemble system is the detection. The ensemble system detect the global signal from all small units at one time. This signal present the average state of all the small units, which can be consider as the average on the space instead of the average on the time. But in the single qubit system, every time

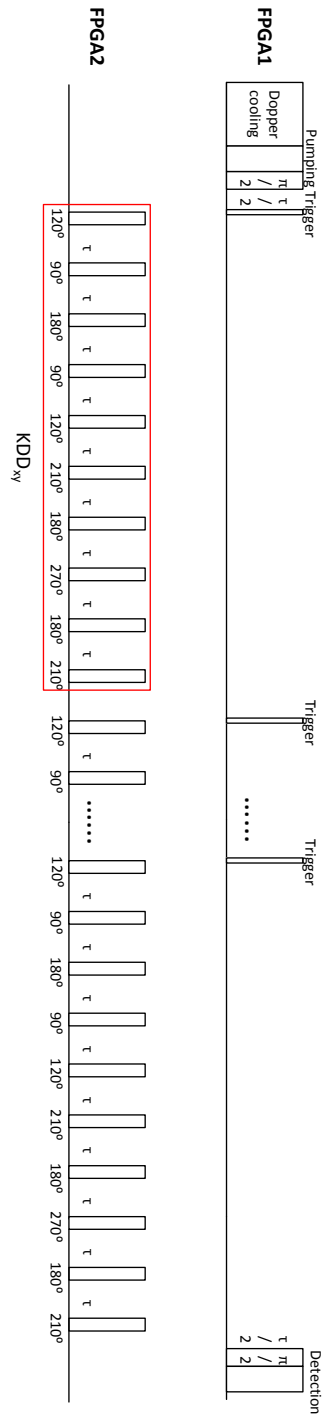


图 3.14 The time diagram of two FPGA.

you can only detect one single qubit signal. We need to do a lot of repetition to have a reliable result of the state we may have, which can be consider as the average on the time. It need less time to take the data for the long time experiment in the ensemble system than the single qubit system. But in the other way, the single qubit system is able to see each result for each process.

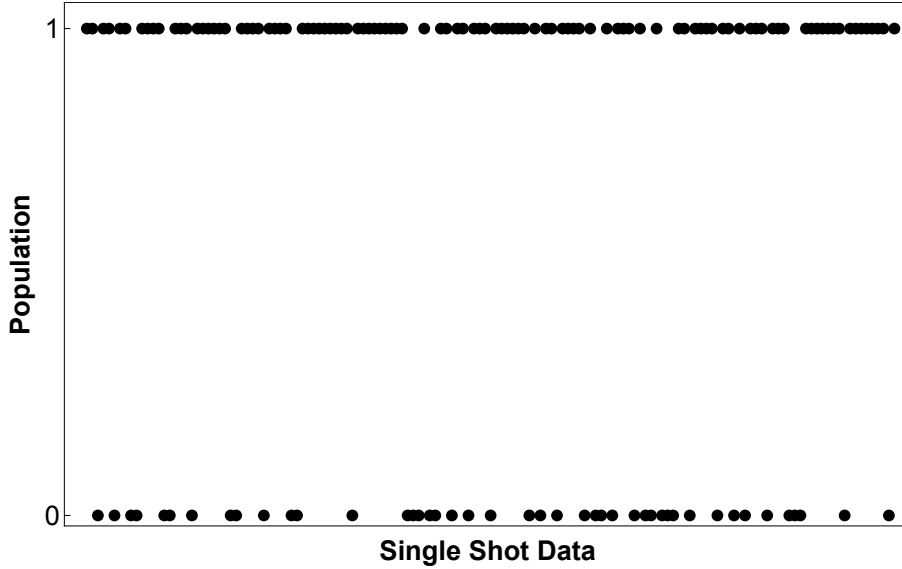


图 3.15 All the single shot population results after 10 minutes with dynamical decoupling

To measure how long is the coherence time of our single qubit, we prepared six initial states, which are $|\uparrow\rangle$, $|\downarrow\rangle$, $1/\sqrt{2}(|\uparrow\rangle + |\downarrow\rangle)$, $1/\sqrt{2}(|\uparrow\rangle + i|\downarrow\rangle)$, $1/\sqrt{2}(|\uparrow\rangle - |\downarrow\rangle)$ and $1/\sqrt{2}(|\uparrow\rangle - i|\downarrow\rangle)$, apply dynamical decoupling pulse and measure the Ramsey contrast in the end. For each initial state, we will measure the Ramsey contrast after a fix time of dynamical decoupling. We choose the total evolution time to be $\{16, 64, 128, 360, 480, 600\}$ seconds in the experiment. So each initial state have 6 points with vary evolution time. We can fit the 6 points with exponential decay to see the coherence time.

For each data point, we repeat the experiment for 30 to 50 times. Each time we measure the final population, which is either 0 or 1. For example, we plot all the raw data we measured after 10 minutes evolution with dynamical decoupling for four initial state together in Fig. 3.15.

After average the raw data with same initial state and same evolution time, we can plot the coherence decay with increasing of the time for each initial state. All the data is show in Fig. 3.16. We see no significant relaxation for the initial states of $|\uparrow\rangle$ and $|\downarrow\rangle$ under KDD_{xy} sequence. The reduction of their contrasts mainly comes from the

accumulation of gate errors. The other four initial states have a similar decoherence rate, which corresponds to a coherence time of 667 ± 17 s from the exponential decay fitting. The demonstrated coherence time is primarily limited by non-vanishing noise strength at the bandpass filter frequency of 2.5 Hz.

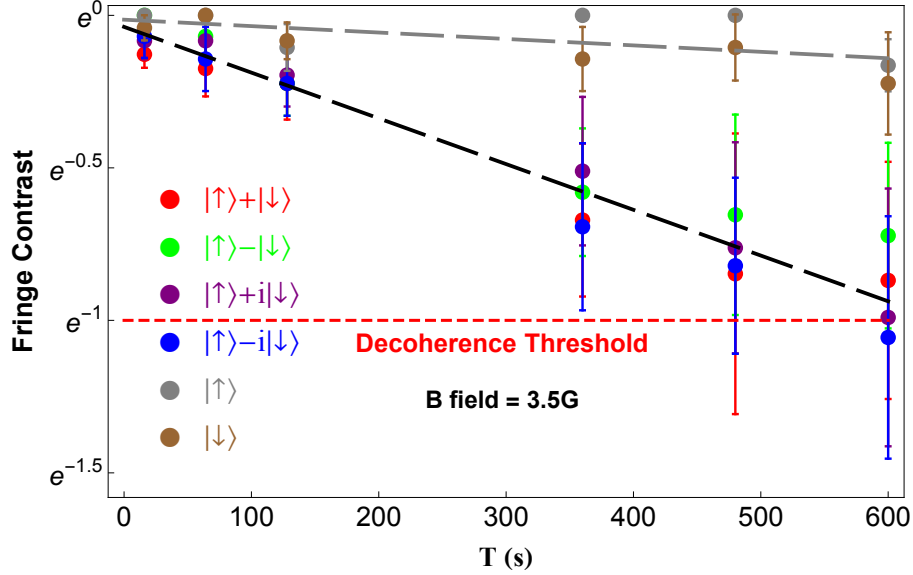


图 3.16 min10

3.5.3 Process tomography

We also perform the process tomography on our dynamical decoupling process for the duration of 8 minutes. The results shown in Fig. 3.17 and 3.18. Here the tomography is obtained from the entire process including initialization, storage and detection. Identity is the dominant diagonal part with $\chi_{II} = 0.699 \pm 0.058$, with the main error corresponding to pure dephasing, in agreement with our knowledge about the hyperfine qubit of the trapped ion system. Fig. 3.18 shows the transformation from the initial states lying on the meshed surface to the final states lying on the solid surface after 8 minutes of storage.

3.5.4 Outlook

We note that our measured coherence time over 10 minutes is not fundamentally limited. The coherence time can be further increased by decreasing $S_{\beta}(\omega)$ at the bandpass frequency, which can be achieved by installing a magnetic field shield, using a magnetic field insensitive qubit at zero crossing regime or using a better microwave oscillator. The number of memory qubits can be increased with sympathetic cooling for quantum

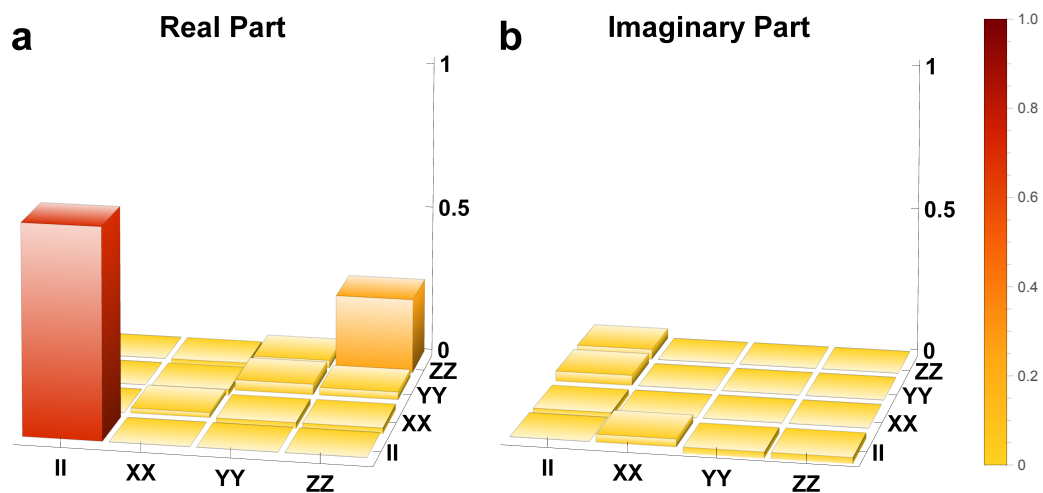


图 3.17 processt

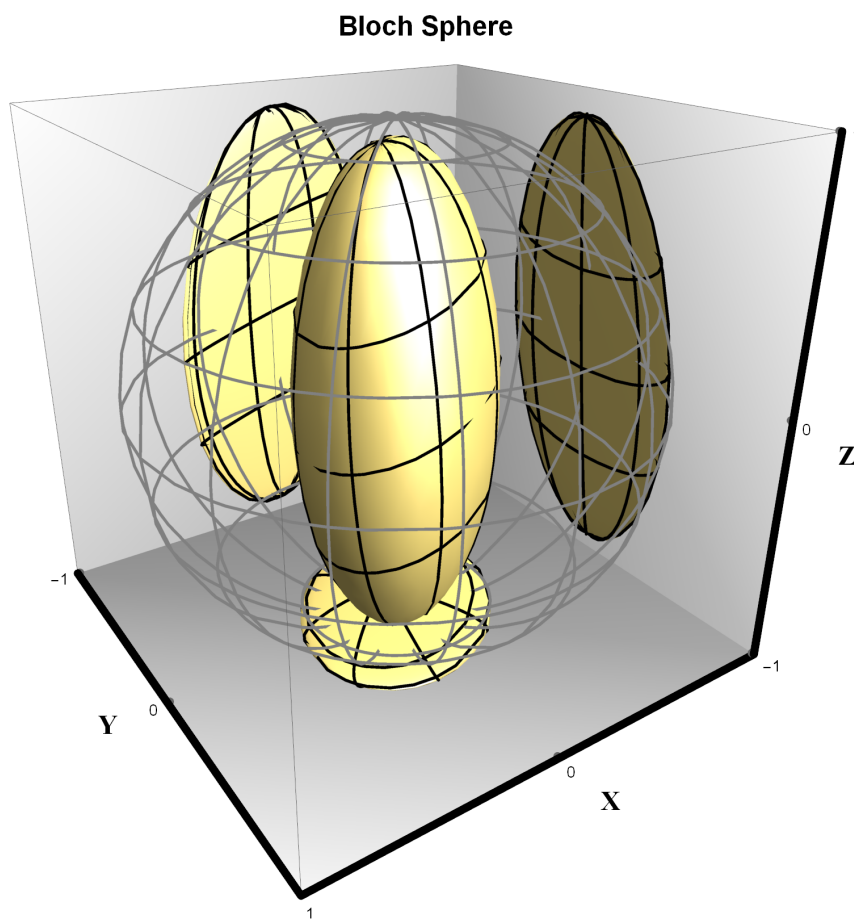


图 3.18 BlochSphere

cryptographic applications including quantum money^[9,10]. Our demonstration of long coherence time would stimulate the development of hybrid setups that map a quantum information in systems with limited quantum memory including superconducting qubits into the trapped ion qubit^[69,70].

第4章 Monolithic 3D ion trap design

4.1 Background

In the past, most ion trap experiments have been performed using traps of bulk metallic electrodes. While this has been successful for several important quantum information and entanglement experiments, there is now an international drive to create microfabricated ion traps which have the possibility of being scaled up to contain many arrays of ions in a single chip. Microfabricated ion traps made of alumina, where the electrodes are laser-machined and gold-coated, were the first type of 'microtraps' to become operational. Wineland's group at NIST Boulder used this type of trap to perform successful experiments such as quantum teleportation^[71], amongst others. Monroe's group at Maryland were the first group to demonstrate ion transport around a 90-degree corner^[72], and achieved this using a gold-coated alumina trap. The first monolithic microfabricated trap was a structure based on GaAs^[73] and is the first step towards using existing sophisticated device fabrication technology. There has been a lot works on the 2D planar trap developments recently. This geometry is easily miniaturized, which is advantageous for scaling both because more electrodes may be fit into a given area.

Despite the advantages of planar trap architectures, a number of issues remain unsolved. To achieve reasonably large trap frequencies, planar traps require shorter ion-electrode distances than conventional three-dimensional traps. This results in high motional heating rates for the ions and causes charge buildup via stray light hitting the trap electrodes. In addition, the proximity of the charges increases the effect of charge buildup as compared to macroscopic three-dimensional traps. Finally, planar traps do not shield stray electrostatic fields from the environment surrounding the trap as well as the three-dimensional trap geometries tend to do. Combined, these effects make the operation of planar traps much more sensitive to uncontrolled charging effects.

Compared to the trap of a 2D array of electrodes, 3D trap geometries can provide a superior potential for confining the ions. . However, previous realizations of 3D geometry traps required post-processing assembly, and serial fabrication process, which means that it is unlikely to be used for a large-scale ion trap quantum processor. Recently, there was a report on a monolithic 3D ion microtrap array etched from a silica-on-silicon wafer using conventional semiconductor fabrication technology^[74,75]. Here, we propose the

implementation of a monolithic 3D ion trap on gold-plated alumina substrate, which is already successful technique for the ion-trap.

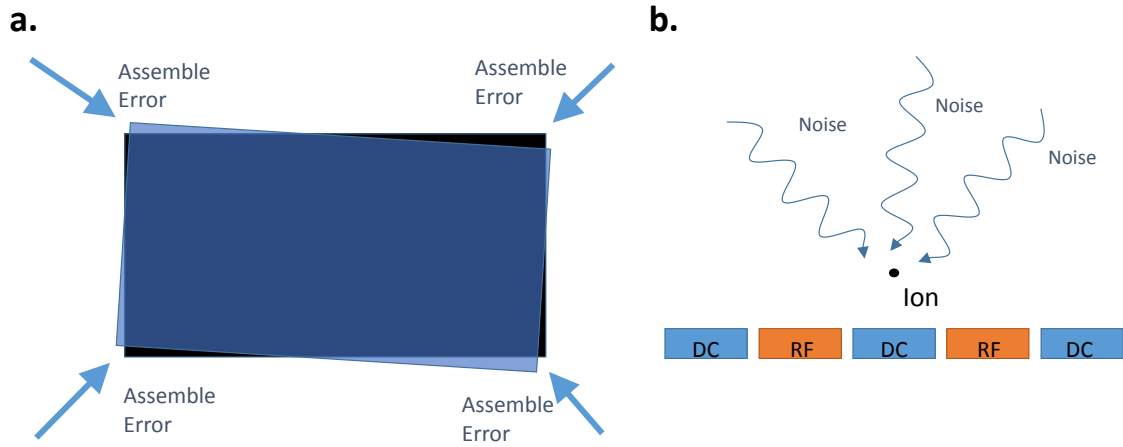


图 4.1 **Weakness of other type of trap.** a, Assemble error b, Surface trap has relatively weak potential. It is subject to environmental noises.

4.2 Design of the monolithic trap

At the first step of designing, we are pretty sure about two techniques to use, one is the gold coating technique for all electrodes, the other is laser cutting technique for making 3D trap structure and separate the electrodes. To construct the 3D structure, we consider the 3-layer trap in Maryland^[72] as a reference. As show in Fig.4.2a, they use three gold coated alumina substrates to realize three layer of electrodes. But if we want to realize the similar structure on one piece, we need to push back the top and bottom electrodes. Since we need to reserved the space for laser to cut the center structure. As show in Fig.4.2b, it is the cutaway view of the substrate for our design. The center corner is the RF electrode, the top part and the bottom part, which is separated with the center part by laser cutting, is the DC electrodes.

Let's think about the potential in the cutaway view, which we can treat it as the xy plane. As mentioned in the Chapter 2.1.1, we may have the pseudo-potential to trap the ion in the middle of the RF electrodes. Since we have DC electrodes in the four position, we have the capability to push the ion in four direction, which is good for the xy plane

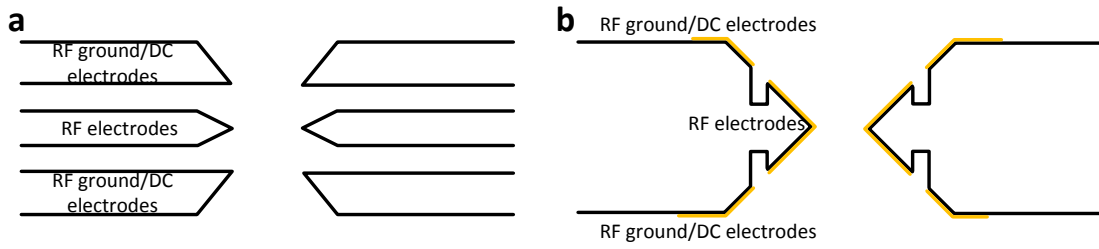


图 4.2 Cutaway view of three-layer trap and our new designed trap

micromotion compensation. We have all the important elements in the xy plane.

We also need to consider the potential in the axial direction, which we define it as z direction. The potential is the static electronic potential generate by the DC electrodes. We want the flexible capacity for the potential control, so we need several segments in the axial direction. We decide to cut each DC electrodes part into 5 segments, so that we can have $4 \times 5 = 20$ independent control DC electrodes. Due to the laser cutting technique limit, we set the with of separate slot as $40 \mu\text{m}$. The diagrammatic figure of the center part of this trap is shown in the Fig.4.3a.

We have one RF electrode, 20 DC electrodes in the design. We want to extend all these electrodes to the margin of the subtract for the out connecting. So we use a $25 \text{ mm} * 20 \text{ mm}$ alumina subtract, extend the electrodes as shown in Fig.4.3b.

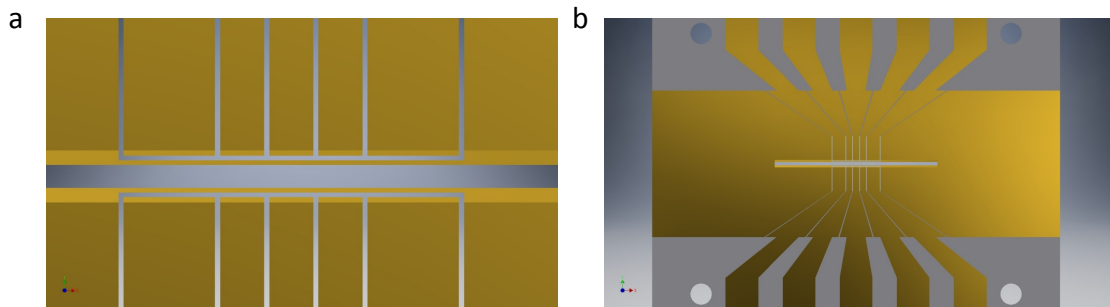


图 4.3 3D model of the structure design in Auto Inventor.

4.3 Trap simulation

We only briefly design the structure of the trap in the xy plane. We need more carefully consideration for all the parameters, like the angle of the RF electrode, the with of the RF electrode, the distance between two RF electrodes, etc. It's important to simulate the trap performance with these uncertain parameters to find a good set of parameters.

In the previous Chapter 2.1.1, we describe the ideal quadrupole potential for trapping charged particles and the pseudo-potential for the traditional four-rod trap. However, the new design structure is quite far away from the four-rod trap. Nevertheless, as long as we keep the overall symmetry, then the potential near the trap center can be approximated by the hyperbolic potential given in Eq. 2-8^[37]. The non-hyperbolic electrodes effect can be treat as an addition of a geometric scaling factor η_{sc} . The modified potential is approximately represented by^[76]

$$\phi_{nonhyp} = \frac{\eta_{sc} V_0}{2} \cos(\Omega_T t) \left(1 + \frac{x^2 - y^2}{R^2}\right) \quad (4-1)$$

The procedure of the simulation is first enter the trap structure design into the simulation software. Then we run the electrostatic simulation with 1 V applied to one of the electrodes, while holding the rest at ground. We do this process for each electrode in the trap structure, thereby producing a set of "electrode basis function", which describe the spatial properties of the potential produced by each electrodes. We export the simulated potential by a grid of points in the space so that we can use it for further analysis. In a analysis program, potential of each electrode can be scaled to a certain voltage by multiplying the electrode basis function by the value. Then we can have the total potential by summation of all electrode basis function. The effect of the RF drive potential is modeled by pseudo-potential approximation of Eq. 2-7, using the gradient of the electrode basis function of RF electrode. Actually, the fact we can do the summation of the electrode basis functions is based on the linearity of the Laplace's equation^[77].

In the following section, we use this method to simulate the four-rod trap as a demonstration of the method and our new designed trap.

4.3.1 CPO simulation

We are using 3D Charged Particle Optics program(CPO-3D) produced by CPO Ltd to do the electrostatic simulation. We will introduce how to use this software to model the trap structure.

To make a new 3D model to simulate, we can open an example data file to edit by clicking

File \implies Open for running and databuilding

and select a sample file. We can use "save as" function to make it a new file.

Then, we need to modify the electrodes parameters to input our structure by clicking

Databuilder \implies Electrodes

so that the "Edit electrodes" window appears as shown in Fig.4.4a. There are some old electrodes data to be deleted by clicking **Delete** button. After delete all the old data, we can add our own design of structure by clicking **Add** button. In the subsequent dialog box, we can choose the shape of the electrode. We can enter in the parameters for this electrodes in the next window as shown in the Fig.4.4b.

We have several items can be adjust, like "Comment line", "Radius", "Centre of 1st end", "Centre of 2st end" and etc. These items varies with different kind of electrode. You can put the right parameter inside. We can choose the address of the voltages to be applied to this electrode,

Addresses of two voltages that will be applied (usually the same)": 1, 1

If we want to use same voltage, we may use same address in two blank space. We can also create a voltage gradient across the electrode. We can change the voltage value by clicking

Databuilder \implies Voltages and magnetic fields

For each voltage address, we can set the voltage value and comment. For the trap simulation, we need at least three voltage, which is ground, DC electrode and RF electrode.

Finally, we need to choose how to segment the electrodes. In general, the large the number of segments, the more precise the simulation will be, the longer time it takes. And it is not good to put a small segment near a big segment. After editing the electrodes, you can save your file.

There is one function may help you saving the calculation time. You can access the symmetries options by clicking

Databuilder \implies Symmetries

You can choose the symmetries method to use. But you need to be careful about the position of all electrodes. The structure should be in the symmetries way.

We are ready to run the simulation now to create the basis function for each electrode. We choose one electrode and set the voltage to be 1, all the other voltage to be 0. Run the simulation bu clicking

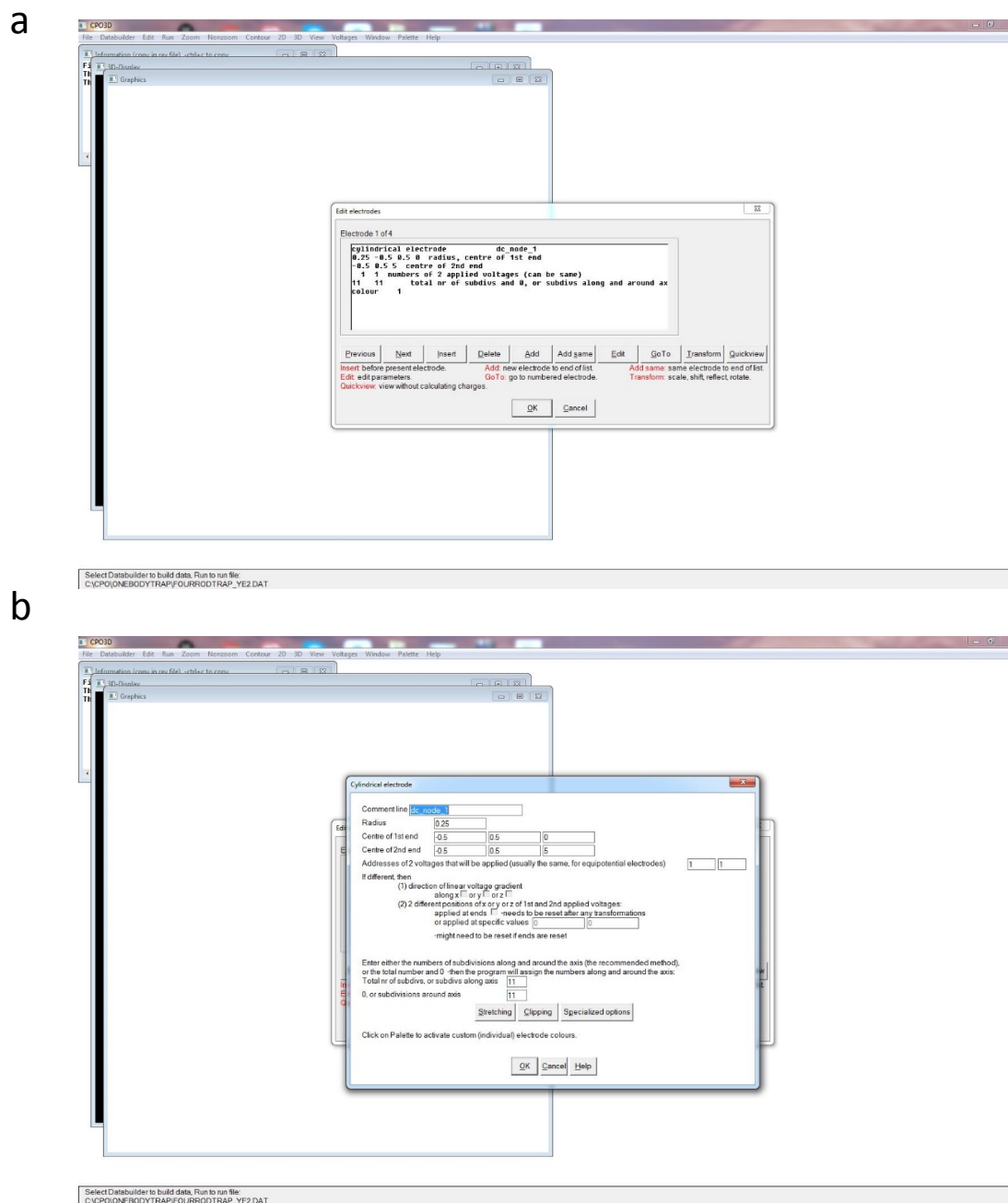


图 4.4 Editing electrodes in CPO

Run \implies All 3 views

The simulation take for some time. It will show a three dimensional rendering of the structure, shown in the Fig.4.5a. You can also see the 3D view by using the button in the "3D view" window.

There are very few analysis tools in CPO. So we need to export the two-dimensional grid data calculated by CPO and use other software to analyze them (which is Mathematica for us). For the DC electrode basis functions, we need the calculated potential data. To export the grid data, we first click **2D** to return to a planar view. Next, choose the plane you want to export by clicking(for example)

View \implies ZX

Then, export a grid of points by first click

Contour \implies Potential \implies Grid

making the "Output grid of values" window appear, as shown in Fig.4.5b. You can choose the point in the third dimension, the range of the grid in the plane you want to see, the number of points to calculate in the range, and the accuracy.

For RF electrode, according to Eq. 2-7, if we want to simulate the pseudo-potential, we need the electric field vector data. So in the second step we need to click

Contour \implies Electric field \implies Grid

The setting is similar with the potential one. You can choose the point in the third dimension, the range of the grid, the number of points, and the accuracy.

Generate all the electrode basis functions by changing the voltages, returning the simulation, and exporting the grid data for each electrode.

4.3.2 Simulation analysis

After calculating the electrode basis function in CPO, we import the data into Mathematica to analyze. A sample of the analysis code is in given in the App. A.

We import the simulation data generated by CPO for each electrode basis function. The pseudo-potential is calculating by Eq. 2-7 with the electric field data. The total effective potential of the trap is created by multiplying the pseudo-potential by a scale

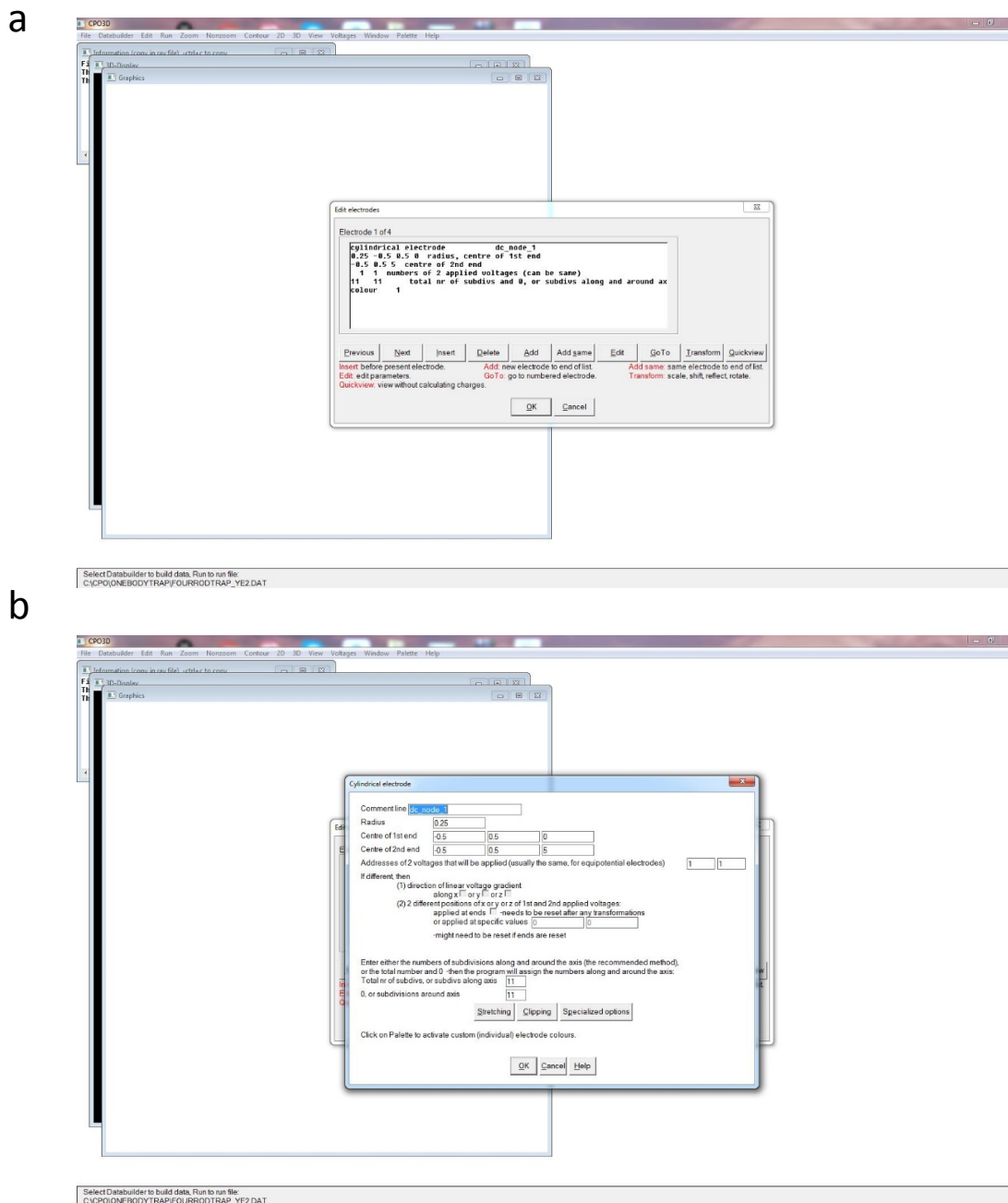


图 4.5 Views and exporting data in CPO

factor representing the voltage value, and adding this to the other electrode basis functions multiplied by the voltage value. The full potential is given by

$$\phi_{sim} = \frac{e}{4m\Omega_T^2} \sum_{j=1}^{N_{rf}} (V_{rf,j} \nabla \phi_{rf,j})^2 + \sum_{k=1}^{N_{dc}} (V_{dc,k} \phi_{dc,k}) \quad (4-2)$$

where N_{rf} and N_{dc} are the number of RF and static electrodes, V_{rf} is the RF voltage, V_{dc} is the static voltage, ϕ_{dc} is the electrode basis function.

We make the four-rod trap model in CPO and follow the steps we have described to verify the simulation method. We use this four-rod trap to do a lot of experiment in our lab^[21]. Each rod diameter is 0.5 mm, the distance between the center of two neighbor rod is 1 mm. We set the drive frequency $\Omega = 2\pi \times 38$ MHz, voltage $V = 1000$ V. The simulated electric field is shown in Fig.4.6a, and the calculated pseudo-potential is shown in Fig.4.6b.

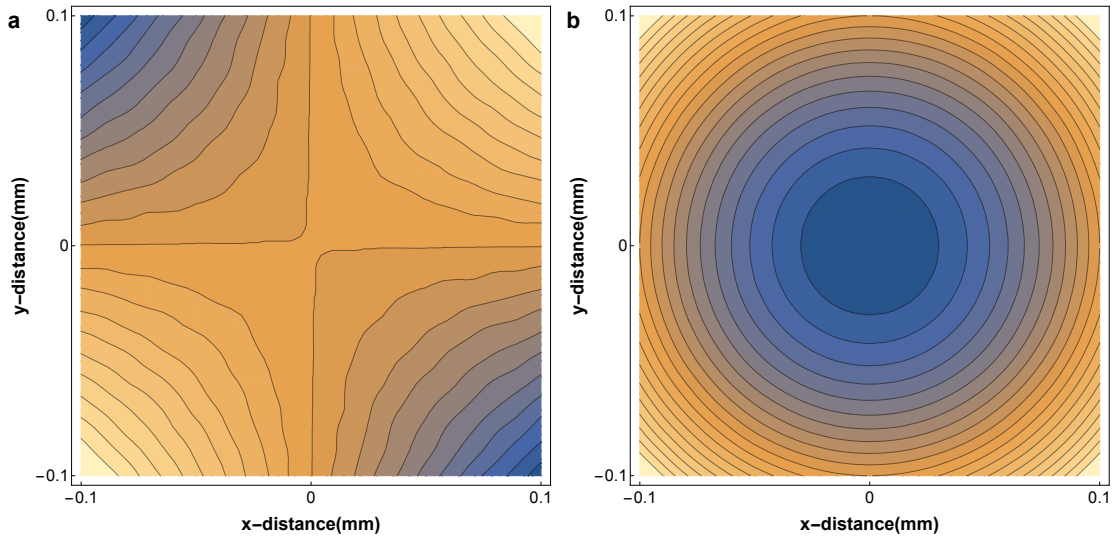


图 4.6 Electric field and pseudo-potential simulated by CPO

The motion of a charged particle in a trap can be treated as a three-dimensional uncoupled harmonic oscillator. The motion of the particle along one principal axes is independent of the other two axes. While in the simple trap such as the four-rod trap, the orientation of the principal axes is very clear. But in general, we decide the principle axes of the trap by using Hessian matrix of the potential, which is^[78]

$$H(\phi_{sim}(x_0, z_0)) = \begin{pmatrix} \frac{\partial^2 \phi_{sim}}{\partial x^2}(x_0, z_0) & \frac{\partial^2 \phi_{sim}}{\partial x \partial z}(x_0, z_0) \\ \frac{\partial^2 \phi_{sim}}{\partial z \partial x}(x_0, z_0) & \frac{\partial^2 \phi_{sim}}{\partial z^2}(x_0, z_0) \end{pmatrix} \quad (4-3)$$

表 4.1 Simulated and practical data for three-layer trap

| | Simulated | Practical |
|----------------------|-----------|-----------|
| Radial Frequency | 4.6 MHz | 5.0 MHz |
| Axis Frequency(100V) | 2.4 MHz | 2.5MHz |

Here x_0 and z_0 are the point where the Hessian matrix is evaluated. In our case, the point would be the center of the trap. The eigenvalues are related to the direction of the principle axes. The Hessian matrix seeks out the directions of the greatest and the least curvature, which are the principal axes.

After determine the principle axes, we can fit the potential along this axes to a parabola. The quadratic coefficient of the fit, which is A_{axis} , determine the secular frequency along this axis

$$\omega = \sqrt{\frac{2eA_{axis}}{m}} \quad (4-4)$$

We can calculate the secular frequency with the ideal hyperbolic case. We can also measure the secular frequency by adding a modulation on the DC electrode and checking the resonance of the ion motion. We set the drive frequency $\Omega = 2\pi \times 38$ MHz, voltage $V = 1000$ V. The measured result is 1.26MHz, the theoretical calculated result is 1.25MHz, and the simulated result is 1.17MHz. We can know the geometric scale factor, η_{sc} .

We also make the three-layer trap model to test our simulation result and to be compared. The practical result is taking from the Ref.^[79]. We compare the simulated and practical results for radio frequency and axial secular trap frequency with $\Omega = 2\pi \times 38$ MHz, $V = 360$ V. The results is shown in the Table. 4.1

4.3.3 Trap performance simulated with different parameters

We use four-rod trap and three-layer trap to test the simulation method. The result shows the reliability of the CPO software and the analysis using Mathematica. The next step is using the simulation to check our new designed trap. The 3D model in CPO is shown in the Fig.4.7. We have 20 DC electrodes, but not all of them is controllable. Half of them are connected to ground, the other half in green color can be individual controlled. There are three important parameter for the design: the distance between two RF electrodes D , the hight of RF electrodes H , and the angle of the slope θ .

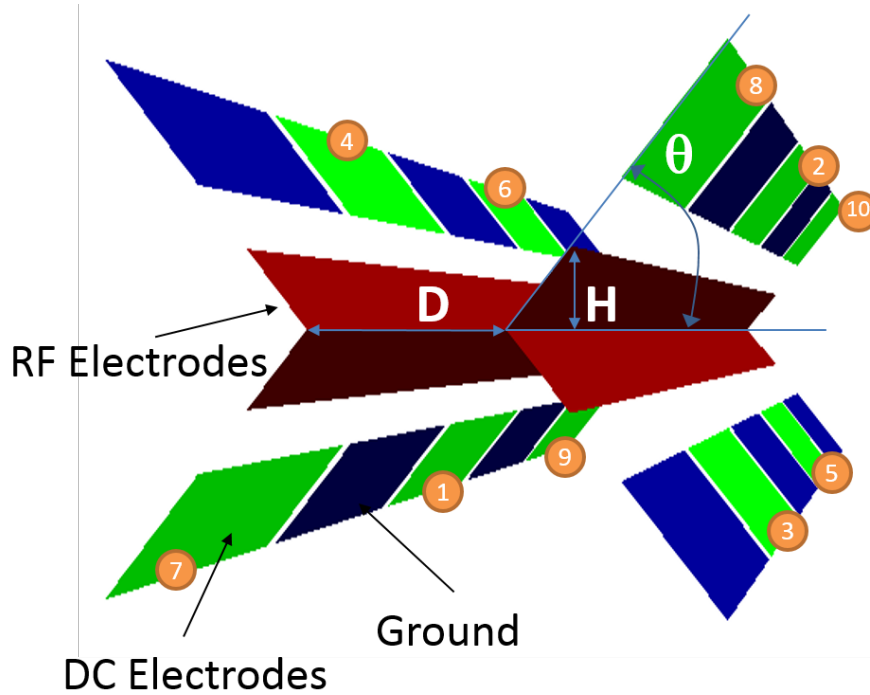


图 4.7 3D model of our monolithic trap.

The most important thing we want to know is the secular frequency ω in the radial plane. In principle, we want the secular frequency as large as possible, as long as the trap is in the stable regime^[2]. In the simulation, we set the drive frequency $\Omega = 2\pi 39$ MHz, the voltage of RF electrode $V = 200$ v, and all the DC electrode is 0 v. We want to check the relationship between these parameters and the secular frequency. The first parameter we want to check is D . Compare to the Eq. ??, we may guess the the relationship is $\omega \propto 1/D^2$.

We write a Python program to generate the different model with different distance D , but same $\theta = \pi/4$ and $H = 10 \mu\text{m}$. The code is show in App. A.2. We generate 30 models, run everyone in CPO and export the electric field grid data for RF electrodes. We have 30 grid data. Then we use Mathematica to analyze these data. We have the results shown in Fig.4.8. The data shows the relationship between D and ω is more like $\omega \propto 1/D$.

To have large secular frequency, it's better to have smaller D . But small D will cause huge laser scattering, which will increase the background of the ion florescence and reduce the pumping and detection efficiency. So we choose $D = 200 \mu\text{m}$ to be the distance.

Next step, we set $D = 200 \mu\text{m}$ and $H = 10 \mu\text{m}$, and generate 20 different models with different angle θ to see the relationship between θ and ω . The data is shown in the

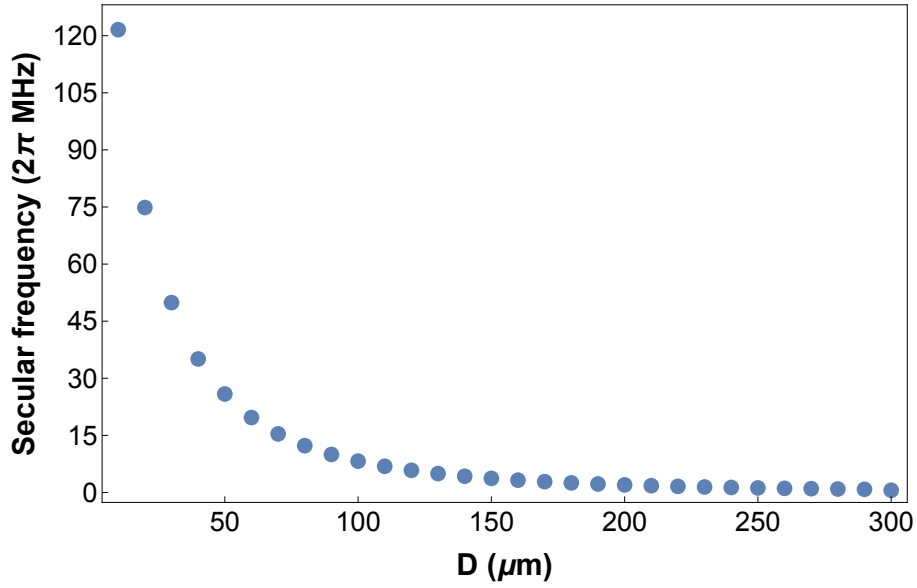


图 4.8 The secular frequency ω depends on the distance D

Fig.4.9.

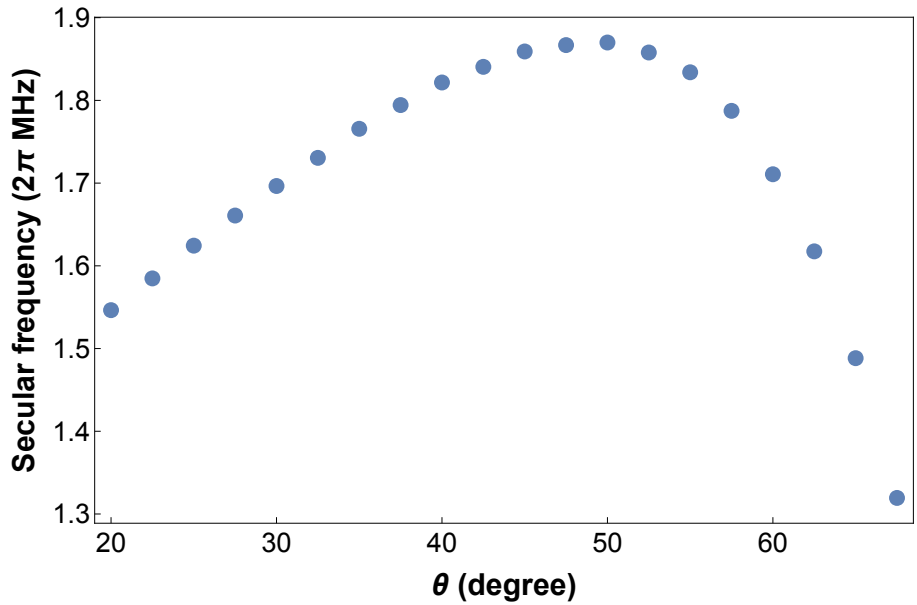


图 4.9 The secular frequency ω depends on the angle θ

You can see there are some extreme value near 50° . This is good for the fabrication since it is easy to make the angle close to 45° by laser cutting. So we choose $\theta = \pi/4$.

We also want to check the relationship between H and ω . We set $D = 200 \mu\text{m}$ and $\theta = \pi/4$, generate several models with different H value. The result is shown in the Fig.4.10

The result shows we may have the extreme value near $H = 25 \mu\text{m}$. This is also an

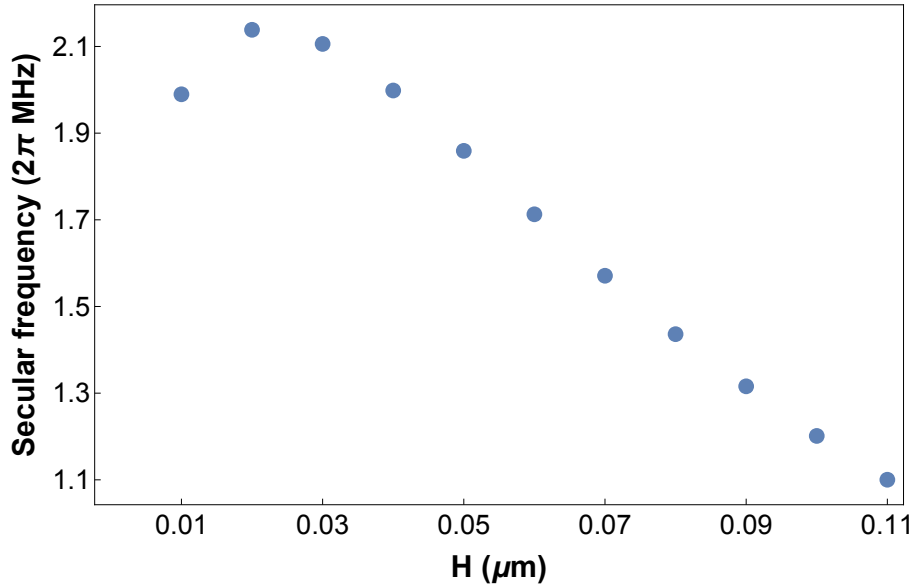


图 4.10 The secular frequency ω depends on the RF electrode height H

acceptable parameter for the laser cutting. In practice, we may have H in the 20 μm to 50 μm range.

Since we can do the generation, exporting, analyzing process automatically, we can have the function $\omega(D, H, \theta)$ with one day calculation by the normal laptop. Some two-dimensional scan result is show in the Fig.wholescan. With the setting $H = 200 \mu\text{m}$, $\theta = \pi/4$, $H = 20 \mu\text{m}$, we may have a trap with reasonable performance. The length of DC electrodes is 375 μm .

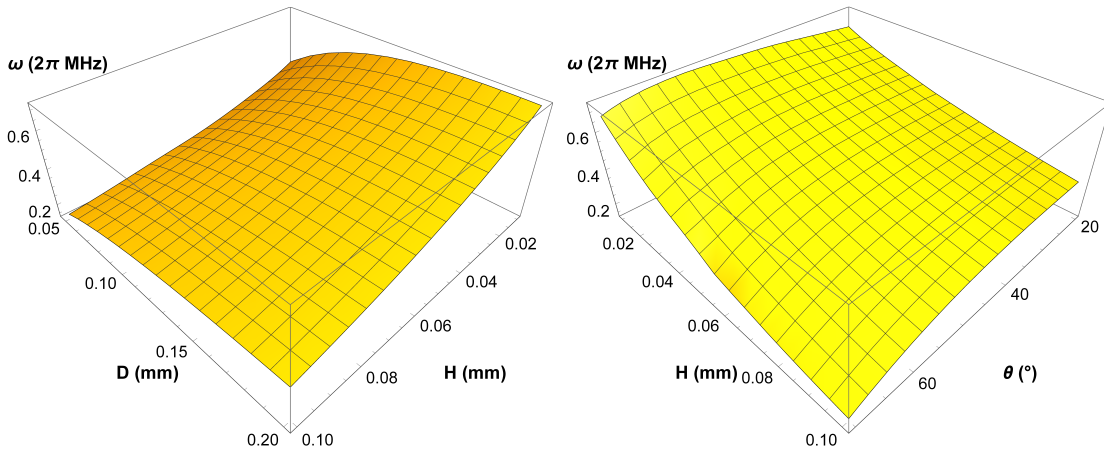


图 4.11 The secular frequency ω depends on all three parameters.

4.3.4 Compare with other traps

We may have two advantage for our own design monolithic trap. One is the monolithic structure without assemble error, the other one is the three-dimensional structure with strong potential. We have decided the detail parameters for our new design trap. We want to compare the performance of our trap to the other success trap in the world.

One of the success three-dimensional trap is the three-layer trap in Monroe's group^[72]. A lot of great results are done in this trap^[41-45]. This trap can hold up to 50 ions for a long time^[80].

The other good trap is the GTRI trap. This trap is fabricated with semiconductor technique.

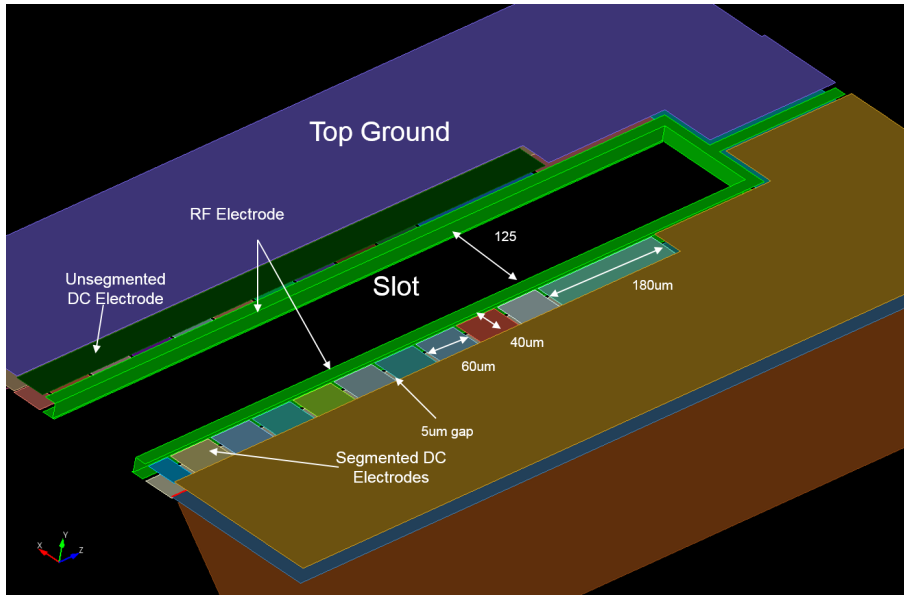


图 4.12 Design of the GTRI trap

We set $\Omega = 2\pi \times 39$ MHz, $V = 200$ v, $V_{dc} = 10$ v. The compare of the these three trap is shown in the Table. We show the compare results of out trap and GTRI trap in Table. 4.2. The RF electrodes distance is $125 \mu\text{m}$ in GTRI trap, so we set the same $D = 125 \mu\text{m}$ for the compare. We set the x axis along the connection of RF electrodes, and y axis perpendicular to the Rf electrodes and the chip surface. We can see Ω_x is similar for two traps but our trap has bigger Ω_y than GTRI trap. This means we have the bigger confinement in y direction. We also see the bigger axial frequency in our trap than GTRI trap. This means the electrodes structure in our design is better than GTRI trap.

We show the compare results of out trap and GTRI trap in Table. 4.3. The RF electrodes distance is $200 \mu\text{m}$ in GTRI trap, so we set the same $D = 200 \mu\text{m}$ for the

表 4.2 Simulated data for our trap and GTRI trap

| Trap | Ω_x | Ω_y | Axis frequency 70 μm | Axis frequency 200 μm |
|-----------|------------|------------|---------------------------------|----------------------------------|
| Our trap | 5.81 MHz | 5.38 MHz | 1.44 MHz | 1.18 MHz |
| GTRI trap | 5.88 MHz | 4.92 MHz | 1.3 MHz | 0.91 MHz |

表 4.3 Simulated data for our trap and three-layer trap

| Trap | Ω_x | Ω_y | Axis frequency |
|------------------|------------|------------|----------------|
| Our trap | 1.68 MHz | 1.68 MHz | 0.43 MHz |
| Three-layer trap | 2.04 MHz | 2.04 MHz | 0.61 MHz |

compare. We can see all Ω_x , Ω_y and axial frequency is smaller in our trap than three-layer trap, about 0.8 times smaller. This reduction of trap frequency is in the tolerable range. With these compare results, we have good confidence to make a trap with good performance.

4.4 electrode control

We have verified the simulation method and used it to determine the design of our monolithic trap. We want to study more carefully about the control of the electrode and the DC electrodes influence on the pseudo-potential. The voltage of DC electrodes is one of the most important parameter, which can be adjust easily, to change the radial potential and do the ion shuttling^[23,24].

4.4.1 Control of the axial potential

We first see the axial potential. We have 20 DC electrodes, 10 of them are ground, 10 of them can be controlled separately. The DC electrodes number and distribution is shown in the Fig.4.7. We show the electrode basis function in the Fig.4.13

We can set the voltage of each electrode and see the summary of all the potential. This may help us to see the whole axial potential in different setting of the DC electrodes. This can help us to realize the ion chain with uniform spacing^[2]. We can also use this tool to simulate the ion shuttling, which should be a very important technique in the trapped ion based quantum computer.

You can see the electrode coding in Fig.4.7. We tried one setting in the real experiment

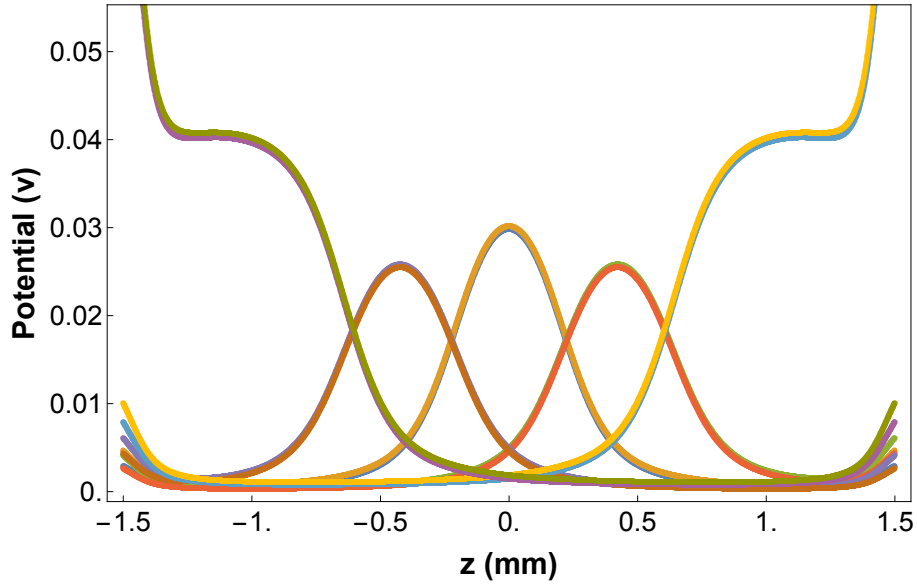


图 4.13 10 electrodes basis function

表 4.4 Simulated data for our trap and three-layer trap

| Index | V_1 | V_2 | V_3 | V_4 | V_5 | V_6 | V_7 | V_8 | V_9 | V_{10} |
|-------|-------|-------|-------|-------|-------|-------|-------|-------|-------|----------|
| 1 | 0 | 10 | 0 | 30 | 3.3 | -7.5 | 20.4 | 15.3 | 10.1 | 5 |
| 2 | 0 | 13.5 | 0 | 30 | 3.3 | -26 | 20.4 | 15.3 | 12.1 | 10 |
| 3 | 0 | 18.7 | 0 | 30 | 3.3 | -26 | 20.4 | 15.3 | 16.1 | 15 |
| 4 | 0 | 22.8 | 0 | 30 | 3.3 | -26 | 20.4 | 15.3 | 18.1 | 20.2 |
| 5 | 0 | 31.6 | 0 | 30 | 3.3 | -26 | 20.4 | 15.3 | 31.6 | 19.7 |
| 6 | 0 | 37.6 | 0 | 30 | 3.3 | -26 | 20.4 | 15.3 | 37 | 23 |

in the Table. 4.4. You can see we didn't use the number 1 and number 3 electrodes. This is because we short-circuit these two electrodes to the ground during the loading process. In the experiment, the loading position is agree with the simulation as shown in Fig.4.14.

4.4.2 Control of the radial frequency

The voltage of DC electrodes will not only affect the the axial potential. It will also affect the radial potential. We can see this effect in the simulation.

Let us first see the radial potential with no voltage on the DC electrode as shown in Fig.4.15a and Fig.4.15b. Two figure are in different scale. We set $\Omega = 2\pi \times 21$ MHz, $V_{rf} = 200v$. The radial potential is the pseudo-potential, which is symmetric in all direction. We can add the potential generated by DC electrodes on this basic pseudo-potential to get the final potential.

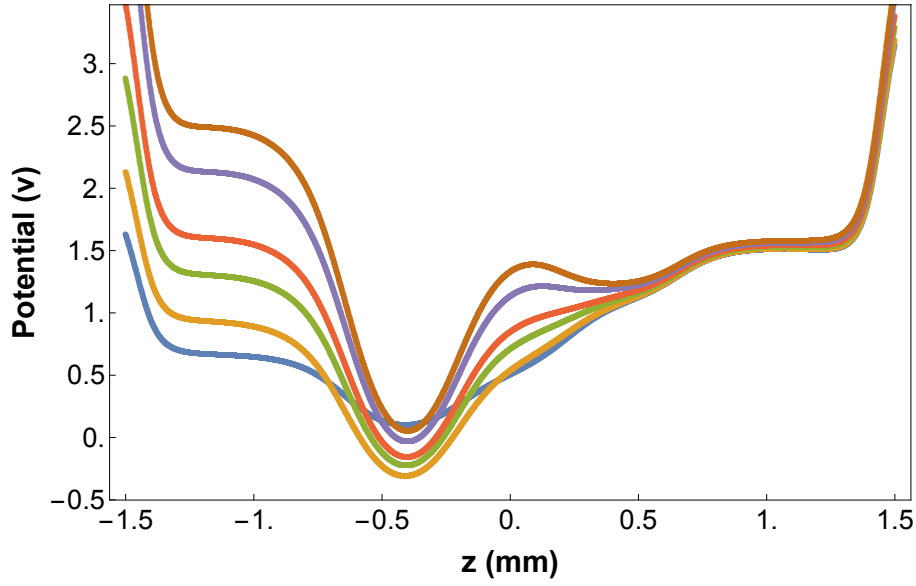


图 4.14 Potential for 10 setting of DC electrodes voltage

We try the voltage setting as $V_1 = V_2 = 10v$, $V_3 = V_4 = V_5 = V_6 = -10v$, and $V_7 = V_8 = V_9 = V_{10} = 0v$. The Fig.4.15c shows the pure static potential generated by all DC electrodes. The Fig.4.15d shows the total potential adding by pseudo-potential and static potential.

There is one thing we may pay attention to. The large voltage on DC electrode will destroy the radial potential which means there is no trap in the radial plane. For example, if we set $\Omega = 2\pi \times 21$ MHz, $V_{rf} = 200v$, $V_1 = V_2 = -50v$, $V_3 = V_4 = V_5 = V_6 = 10v$, and $V_7 = V_8 = V_9 = V_{10} = 0v$. We may see the pure static potential and the total potential in Fig.4.15e and Fig.4.15e. Fig.4.15e is the pure radial potential only generated by DC electrodes. Fig.4.15f is the combination with static potential with DC electrodes and pseudo-potential. This results remind us to carefully set the DC electrode voltage. If we set a large absolute value of the voltage for some DC electrode, it may destroy the trap.

4.4.3 Rotate the axis angle

You may already see the effect of rotating of the principle axes in Fig.4.15d and Fig.4.15f. The combined static and pseudo-potentials that determine the motion of a ion in our trap are written as a three-dimensional uncoupled harmonic oscillator potential:

$$\psi_{radial} = \psi_p + U_{dc} \quad (4-5)$$

$$= \frac{eV_{rf}^2}{4m\Omega_T^2}(x^2 + y^2) \quad (4-6)$$

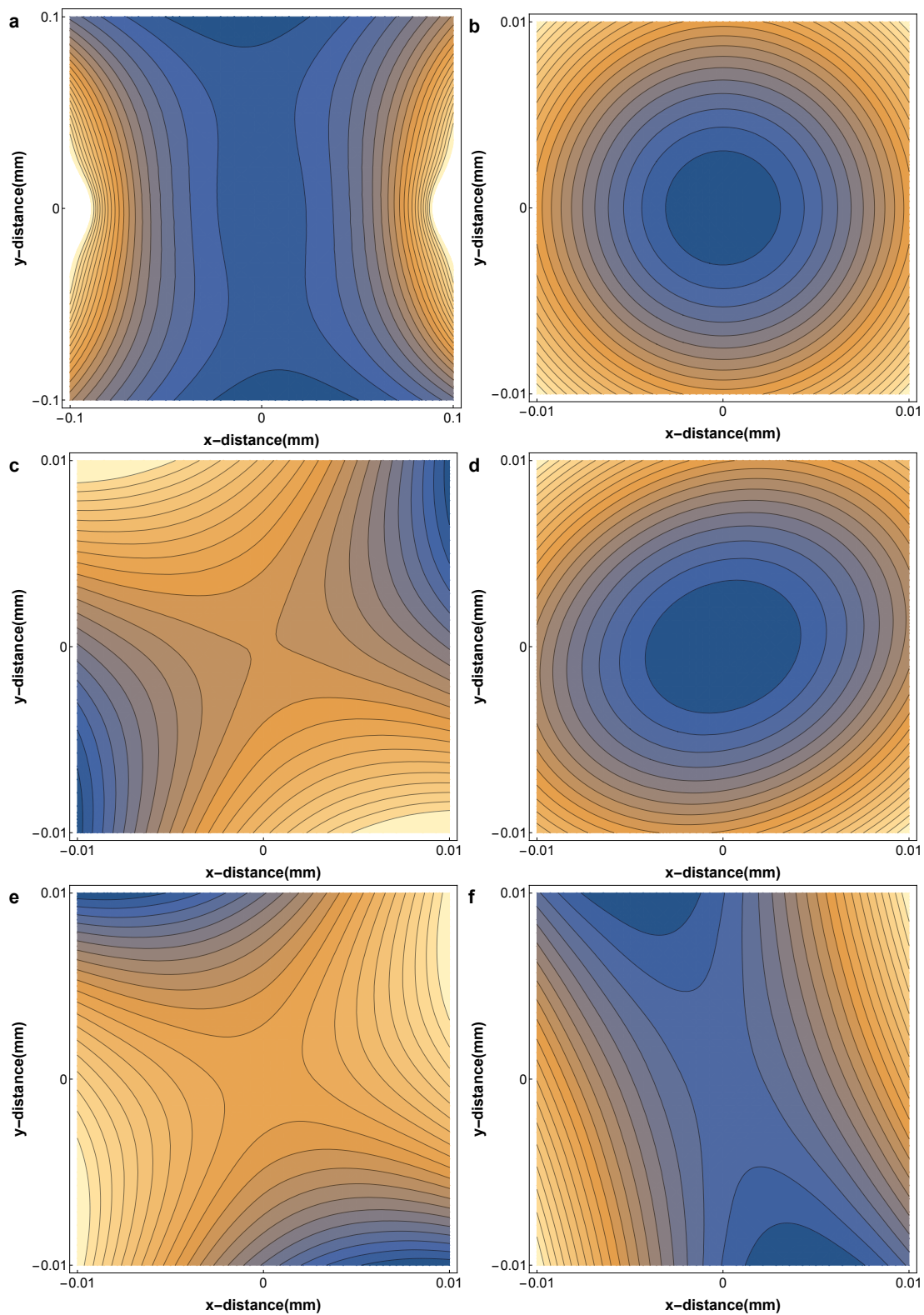


图 4.15 Pure radial potential for DC electrodes and total radial potential

$$+\frac{U_{dc}}{d^2}(-\epsilon x^2 - (1 - \epsilon)y^2 + \lambda xy + z^2) \quad (4-7)$$

where λ is the xy cross term. This cross term comes from the angle of DC electrodes in the xy coordinate system. This cross term will also affect the rotating of principle axes for the final potential. We can use the Hessian matrix (Eq. 4-3) to calculate the principle axes or finding the greatest and least curvature in the simulated potential.

The rotating of principle axes is necessary for the experiment. In the experiment, the Doppler cooling laser is aligned along the y direction to passing through the trap. If we don't rotate the principle axes, the x axis motion is barely cooled by the laser. This will cause the shaking in the x direction which is observed in the experiment. Further more, in the limiting case, we can rotate the axes near $\pi/2$ and make the separation real big. This will allow us to realize a two-dimension ion crystal in the yz plane, which is good for imaging in the existing imagine system.

第5章 Trap Fabrication and assembling

In the last Chapter, we discuss the design of our monolithic three-dimensional trap. We see the the acceptable range for three important parameters, which are distance between RF electrodes D , the angle of the slope θ , and the hight of the RF electrodes H . We will discuss the fabrication details of this trap and the assembling details in this chapter.

5.1 Fabrication technique

We plain to use laser cutting and gold coating to realize the structure discussed in the last chapter. There are lots of technique details in the fabrication process. There are several important requirement we want to achieve.

1. We want the structure as precise as possible to the design, especial the RF electrodes. We want the RF electrodes parallel as soon as possible, otherwise the oscillating electric field will cause redundant axial pseudo-potential.
2. We want cutting surface quality as smooth as possible. When we apply high voltage on the electrode, the burr on the cutting surface may cause the electric spark damaging the electrode.
3. We want the surface of the gold coating as clean as possible. The rough or dirty surface may increase the heating rate of the trap.
4. We want the insulating surface exposing to the ion as small as possible. The insulating surface may have some accumulative charge problem, this problem may change the electric condition in the trap day by day.

5.1.1 Steps to make the trap

We want to make the three-layer structure in one piece. The most difficult part is the slope part. It's difficult to make the slope with certain precision. It's even more difficult to make small structure on the slope. We follow these steps to make the slope. We are using the alumina subtract with surfaceness < 30 nm.

1. We make a $200 \mu\text{m}$ slot in the center of the chip, as shown in the Fig. 5.1a.
2. As shown in Fig. 5.1b, we use laser to cut out some steps on the edge, then cut out more steps on the original steps. We repeat this process many times to make every

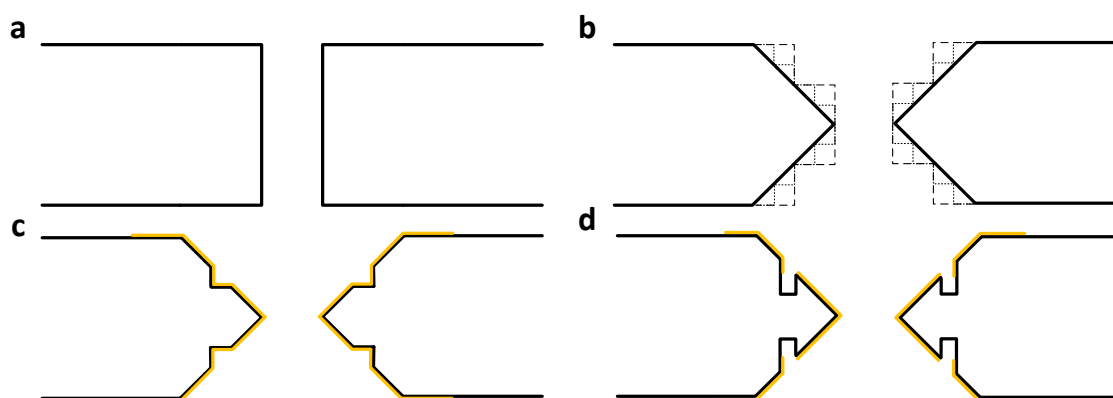


图 5.1 Three step to make the slop

step small enough, so that the total structure looks like a 45 °C chamfer. The width for the smallest steps is 10 μm .

3. As shown in Fig. 5.1c, we make a very small groove on each slope.
4. Do the gold coating on both two side of the chip as we showed in Fig. 4.3b. We also do the gold coating on the slope and groove surface.
5. As shown in Fig. 5.1d, we use laser to cut deeper on the groove position. This will separate the center gold part and top and bottom gold part, so that we can use the center part as the RF electrodes, the top and bottom electrodes as the DC and ground electrodes. Further more, step 3 reduce the insulating area where ion can see, this will make the trap condition more stable.
6. We use laser cut some slot on the both surface of the chip to separate all the DC and ground electrodes.

5.1.2 Laser cutting

We cooperate with Delong laser Ltd. for the laser cutting part and with Dayu electronic Ltd. for the gold coating part. We iterated many times to have the best cutting effect.

We struggled a lot about the cutting depth for the laser cutting. At first we only cut the gold. Like the SEM image shown in Fig. 5.2. This is easy for the laser, and the edge of the cutting is also very clean. But when we test this chip, we find some problem.

When we first test the chip, we are not sure about the laser alignment and the electric situation in the trap. So use a big current for the atom oven. A lot of atom spray to the center area of the trap. After hours of loading, some bad things happened: the center electrodes are shorted by the atom coating. This effect destroy two of the center part

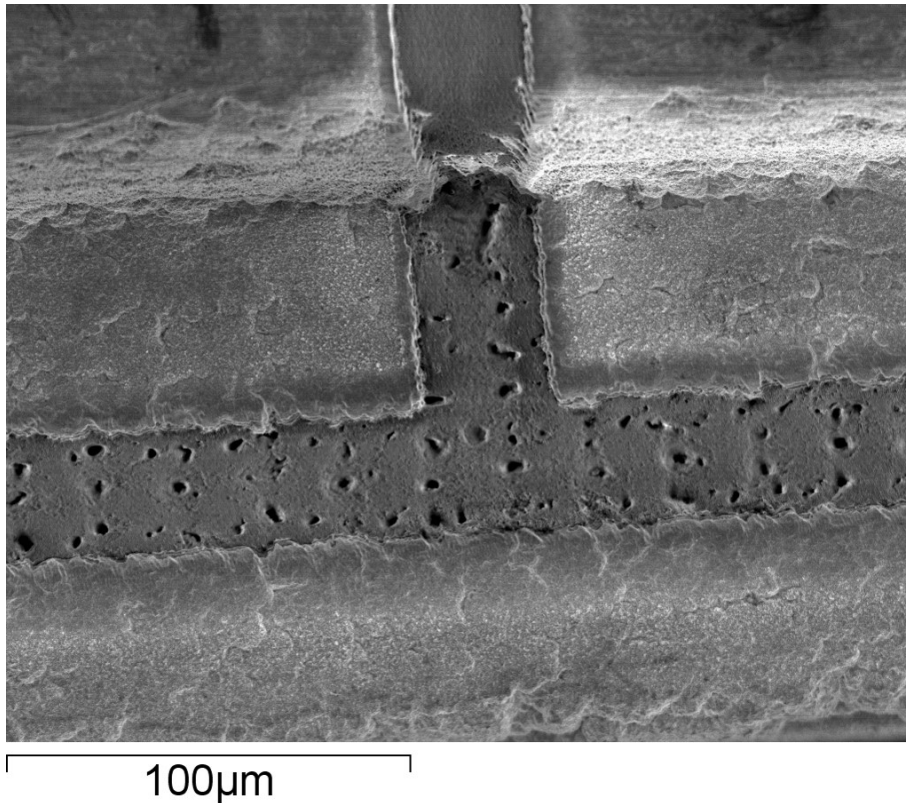


图 5.2 SEM image of only cutting the gold

electrodes. Even we load the ion finally, we lose two important control of the ion. That's the reason we use such a strange voltage in the Table. 4.4. We need to cut deeper.

So in the second version, we cut through the alumina for all the cutting part. This need more carefully control on the laser than only cut the gold. After month of time, we find the right parameter to make a clean cut as shown in the Fig. 5.3. This picture shows a really clean cut for both gold and alumina. But we find another problem for this version.

Cutting through make the center RF electrode very narrow. It's a 3 mm long and 20 μm wide strip. When we apply the small power for the RF signal, like 0.2 W. Everything looks good. But when we apply a big power for the RF signal, like 2 W, the electrode start to shake. This shake change the ion position and almost every condition for the trap. When we have multiple ions, sometime we need to low the RF signal power to make the ion cloud into a crystal. This process will make the trap unstable. Cutting through is not a good idea.

In the third version, we decide not to cut through, but definitely deeper than only cut the gold. We cut one side, which is facing the atom oven, deeper than the other side, which is facing viewport. You can see the optical microscope image of this version in Fig. 5.4. The cutting is still very clean, But you can see the is still some connection between

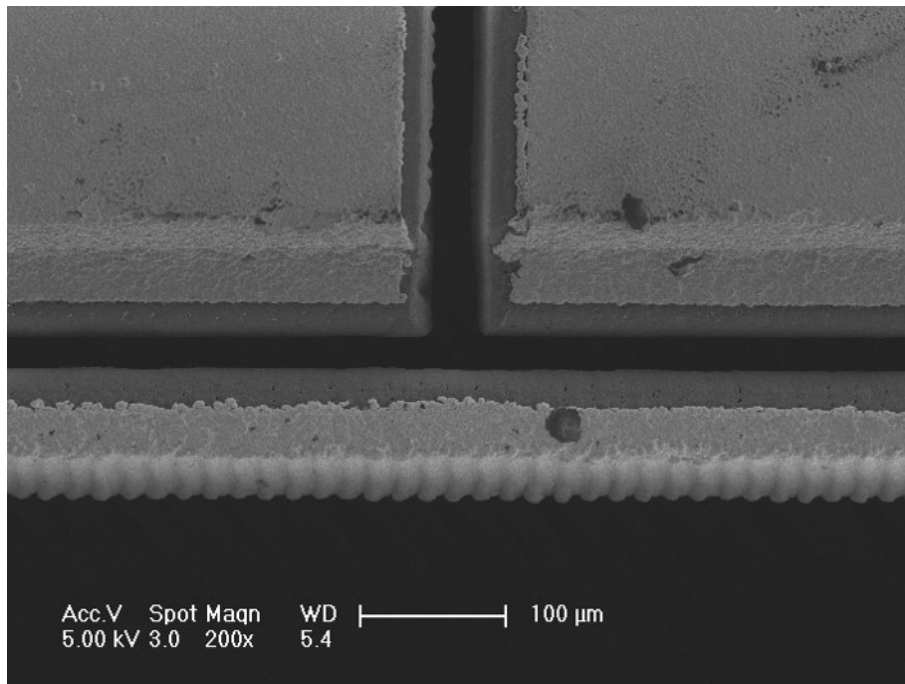


图 5.3 SEM image of cutting through the alumina

the RF electrode and the main part of the chip. Finally, this version works well.

The parameter for laser cutting:

Power 2W

Cutting speed 100mm/s

repetition rate 74KHz

The information about the laser cutting system is list as follow:

Model PH1-10

Average power > 2.5 W

Wavelength 355 nm

Repetition rate 200KHz

Pulse width 290 ps ~ 10 ps

Energy stability < 1% RMS over 24 hours

Beam quality $M^2 < 1.2$

Beam waist 15 μm

Repeat precision of worktable ±1 μm

Positioning precision of worktable ±1 μm

Galvanometer precision ± 10 μm

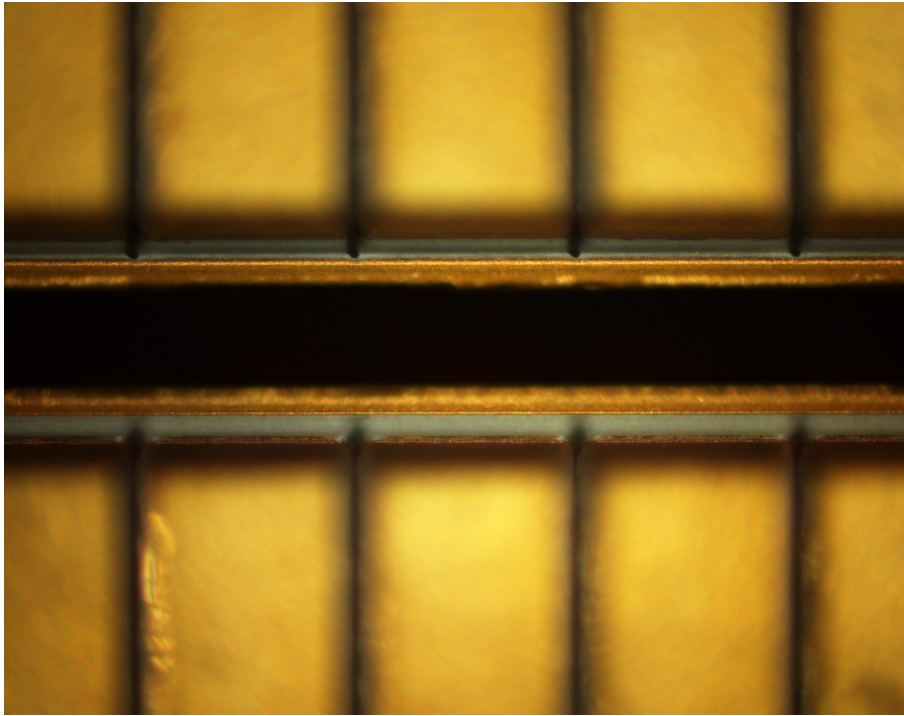


图 5.4 Optical microscope image of cutting deep

5.1.3 Gold coating

Gold coating procedure:

1. Make the mask according to the design. The precision is $\pm 1 \mu\text{m}$.
2. Use acid and alkali with ultrasonic clean machine to clean the substrate.
3. Sputtering coating titanium for the whole area with 50 nm.
4. Sputtering coating copper for the whole area with 3 μm .
5. Sputtering coating titanium for the whole area with 10 nm.
6. According to the film circuit graphics, do photoresist, exposure, removing glue and other processes.
7. Plating gold with potassium cyanide gold plating solution. Thickness is 3 μm .
8. Removing the unnecessary metal without gold.

The gold coating thickness and quality is good. There are no unexpected exposure area in the center part for all electrodes.

5.2 Design of the main chamber

After we have a good chip of our monolithic trap, we need to assemble it into the vacuum system and connect all the electrode to the electronic feed through. We choose a hemisphere chamber from Kimble Physics Inc to be the main chamber. We choose

hemisphere because it has a big port for collecting photon from the ion and also 4 port in the other side for laser alignment. These four port allow us to

I will describe the chamber design in the following sections.

5.2.1 Low-pass filter

The static electrodes has two function which are both confinement electrodes and the RF grounding electrodes. The Rf ground function is done by connecting a low-pass filter to the electrode, which can shunt the RF signal back to the ground.

We are using the pi-network low-pass filter for all ten electrodes. The schematic diagram is shown in the Fig. 5.5. We are using the surface resistance directly on the chip and the surface mount capacitors from Novacap (model is 0402B102J251P). The resistors used are 1 k Ω and the capacitors used are 1000 pF.

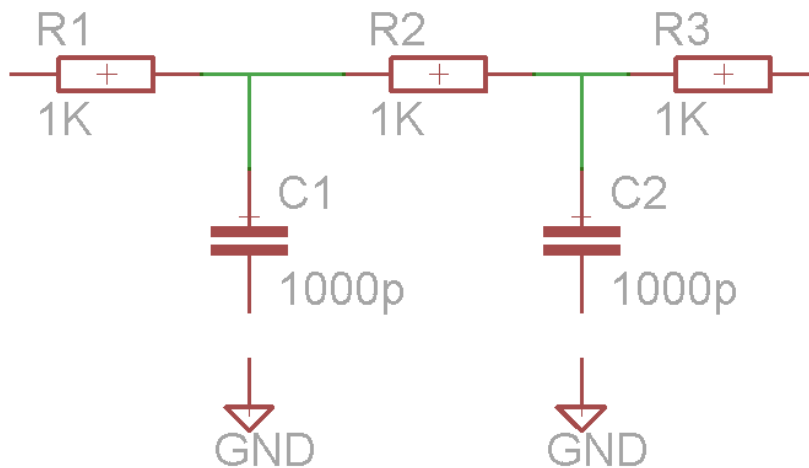


图 5.5 Schematic diagram of the low-pass filter

5.2.2 Electronic connection

We make two kind of low-pass filter chip for the connection for all 10 electrodes. Since we intervein 10 static electrodes and 10 ground electrodes in one side of surface, as shown in the Fig. 5.6, we have different pattern on the left and right side. Two different pattern need two different low-pass filter chip. One of them has three ground and two low-pass filter, the other one has two ground and three low-pass filter. We connect the main part of the trap and low-pass filter by gold ribbon bonding.

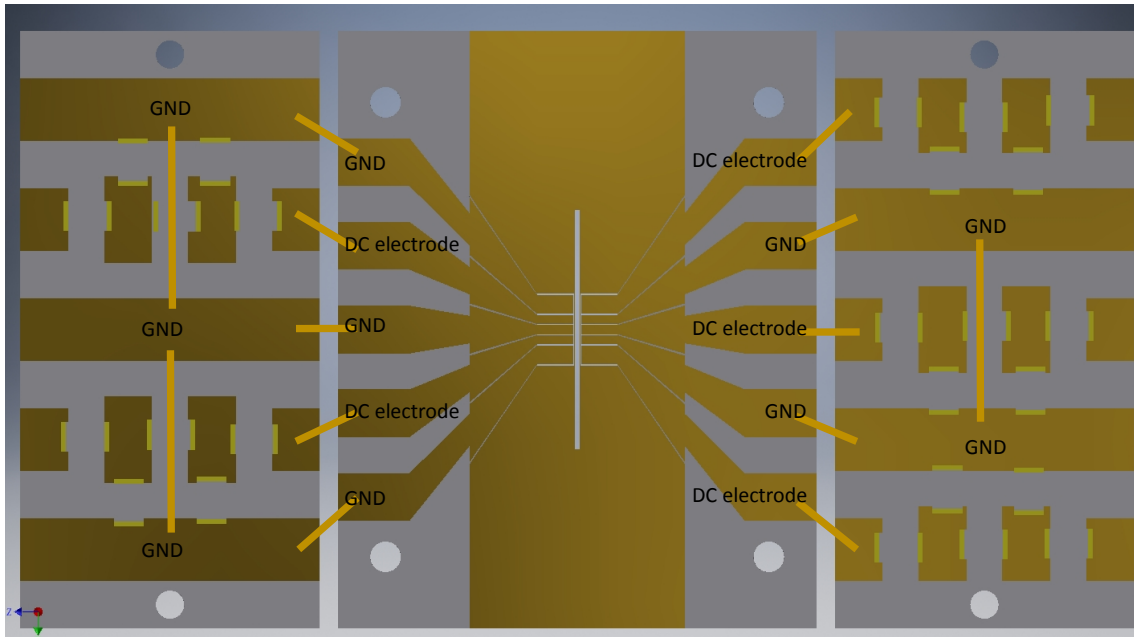


图 5.6 Schematic diagram of the low-pass filter

We are using the machine from West Bond Inc. which model is 7603D to do the ribbon bonding. The machine can attach the $50\ \mu\text{m}$ width gold ribbon to the gold surface by pressuring the ribbon on the surface and applying the vibration at the same time. The gold surface should be heated around $200\ ^\circ\text{C}$ to help the process. There is a holder with the machine which can hold the chip and heat the chip.

This brings a problem for the connection. When we are going to do the electronic connection on the other side with similar electrode distribution using gold ribbon, it's impossible to put the chip on the bonding machine holder. Since there is already some ribbon and capacitor structure in the back side, the chip can not be placed flat.

This requires a customized holder leaving the space for the back side structure in our case. We design this holder as shown in the Fig. 5.7. Figure a shows the three parts to hold the main chip of trap and two low-pass filters. Figure b shows the place for the back side structure. We can make the electronic connection for both sides of the trap.

There is another tip for the electric connection. We have two or three ground parts in the low-pass filter. We need to connect them by the ribbon as well. So we need to insert a step after we make the first surface electric connection. As shown in the Fig. 5.8, we connect the ground of the third and the fourth low-pass filter chip to the ground of the first and the second low-pass filter. Then we rotate the third and the fourth filter to the back side of the first and the second filter. We turn the whole structure around and put it on the bonding machine holder to finish the final connection.

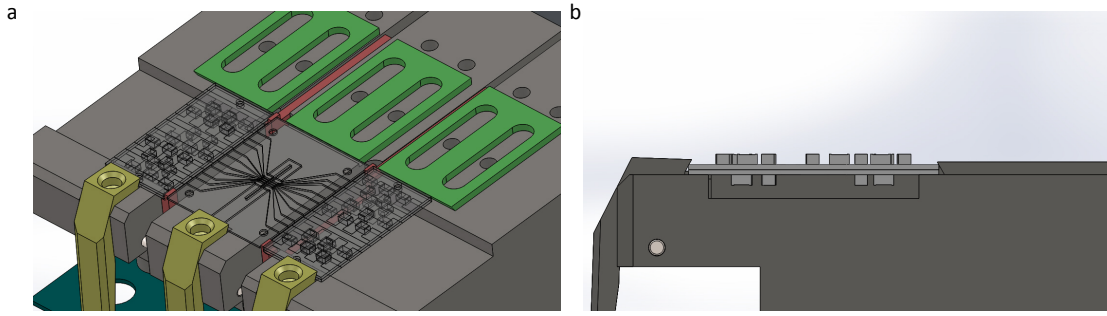


图 5.7 Diagram of customized wire bonding holder

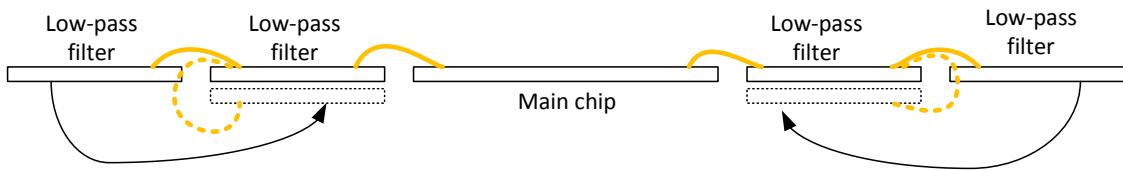


图 5.8 Diagram of how to connect the third and the fourth low-pass filter to the first two.

when we are making the electric connection, we need leave some gold ribbon tail on the outside of the low-pass filter for each electrode. This is for further connecting the gold ribbon with the enameled wire, then connect to the feed through.

5.2.3 Holder design

We design the holder for fixing the main chip and 4 low-pass filter and also mounting to the chamber. In the Fig. 5.9, we show the 3D model of the holder. It has a slot in the center leaving the space for the laser and atom beams. The slot width is 2 mm, with 45° chamfer on the back side. The slot can not be too big, since the atom beam can easily short-circuit the electrodes even we cut deep to separate them. The chamfer is leaving the angle for the laser alignment.

There are eight small pillars with threaded hole in the center for fixing the main chip and four low-pass filter with screws, as shown in the Fig. 5.9c. There are eight threaded hole for the oven connection on the back side. 12 small holes are placed on the two side, which let the enameled wire pass through for the electric connecting. There are three legs on each side for the mounting with the grabber on the chamber.

5.2.4 Oven design

The direction of atom oven is important. We should aim the oven to the center of the trap, otherwise it's hardly to load the ion. To guarantee the angle of the oven, we design a

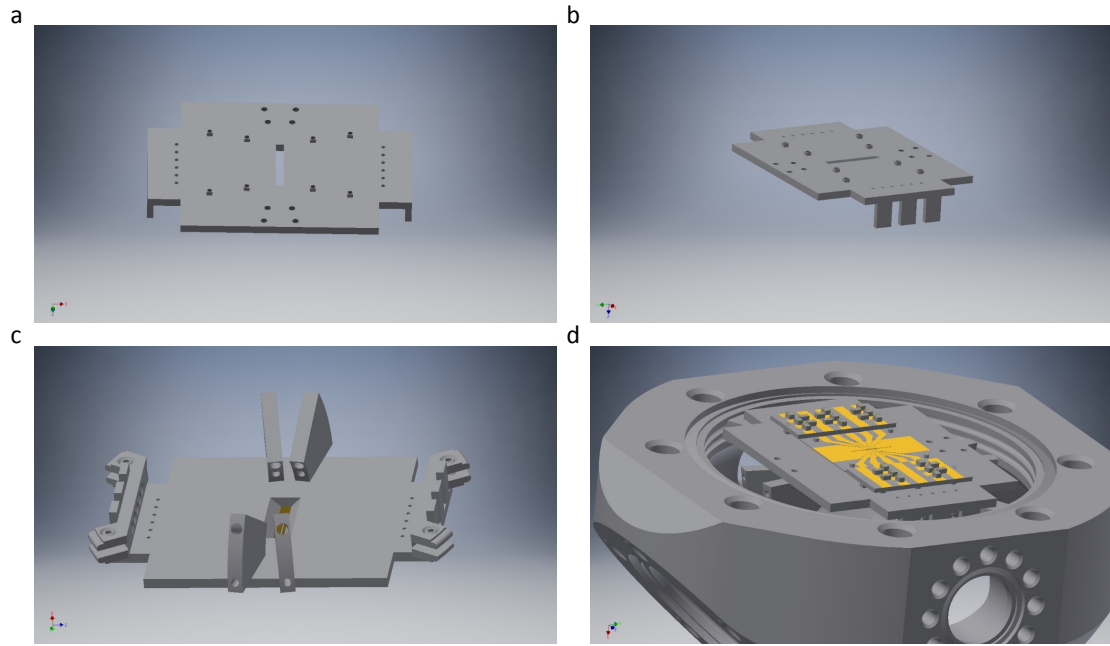


图 5.9 3D model of the holder and connection with trap, low-pass filter and chamber.

sector holder for the oven, as shown in the Fig. 5.9c. The oven holder is connected to the main holder with screw and threaded hole. With the general workshop working accuracy, the oven will aim to the center.

We put a ceramic tube into the hole in the oven holder, then put a stainless tube filled with target materials into the ceramic tube and seal the back side of the stainless tube. We connect the front part of the stainless tube to the oven holder using a stainless wire and connect a wire to the back side of the stainless tube. All the metal connection is done by spot welding.

The bad thing for this design is the conduction of heat. When we load the ion, we heat the oven part to around 480 °C. This heat will spread to the main holder and affect the whole structure a little bit. We observe the small drifting in the 10 minutes after we load the ion, we think this is due to the conduction of heat. In the next version, we will separate the oven and the main holder.

5.3 Assembling process

Assemble process is a delicate process. For the main part assemble, we need to fix every thing on the right position, tight enough but not break the chip. The electric connection part is difficult, we need to connect the electrodes with gold ribbon and connect the gold ribbon to enameled wire with spot welding. It is easy to break the connection

in the after operation like mounting the holder to the grabber. There are near 15 electric connection include RF electrode, 10 DC electrode, 4 oven. We should to be very carefully in the assembling process

5.3.1 Main part assemble

We follow the following steps to assemble the main part together:

1. Connect the main chip and four low-pass filter as we mentioned in Chapter5.2.2.
2. Fix the alumina part to the main holder with screws.
3. Connect the oven holder to the main holder.
4. Fix the enameled wire to main holder through the small holes.
5. Mount the main holder to the grabber on the chamber.
6. Do the spot welding for the gold ribbon and enameled wire.
7. Assemble all the viewport.

For the ribbon bonding connection, we have some small trick to make the connection very strong. We use the ribbon with 500 μm wide and 25 μm thick. We find that the ribbon itself is very strong, but the attached part on the gold surface is very fragile. When we pull the ribbon which is connected to the gold surface, the ribbon never break. So we find some way to increase the connection part on the gold surface, which is shown in the Fig. 5.10a. We increase 3 to 5 crosswise ribbon on the top of the original ribbon, so that we need to break the crosswise ribbon one by one for breaking the attached part for the original ribbon. We also use 3 to 5 ribbon to connect the electrode to increase the strength. Fig. 5.10b shows a example of the connection with the main chip and four low-pass filter on the bonding holder. Both main chip and low-pass filter chip is the old version, but the connection method is same.

When we use the screw to fix the chip on the holder, we would better to use the Pan or Truss or Round head screw, since the head has the flat surface on the chip. This can avoid breaking the chip. We put washers for each screws, but in different side for the ground connection, which is shown in the Fig. 5.11.

The most difficult part for the chamber assembling is the spot welding connecting the gold ribbon and enameled wire. For this connection, we first make a small stainless piece and connect it to the enameled wire using spot welding. Then use the spot welding to connect the gold ribbon and the stainless piece. When we do the spot welding for the gold ribbon, we use almost the smallest current to avoid breakdown of the ribbon.

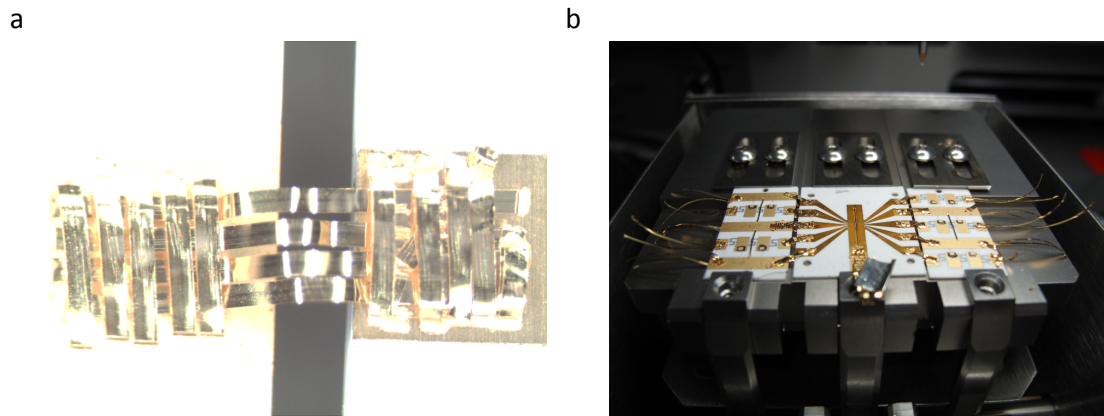


图 5.10 We increase the crosswise ribbon to increase the strength of the attached part.

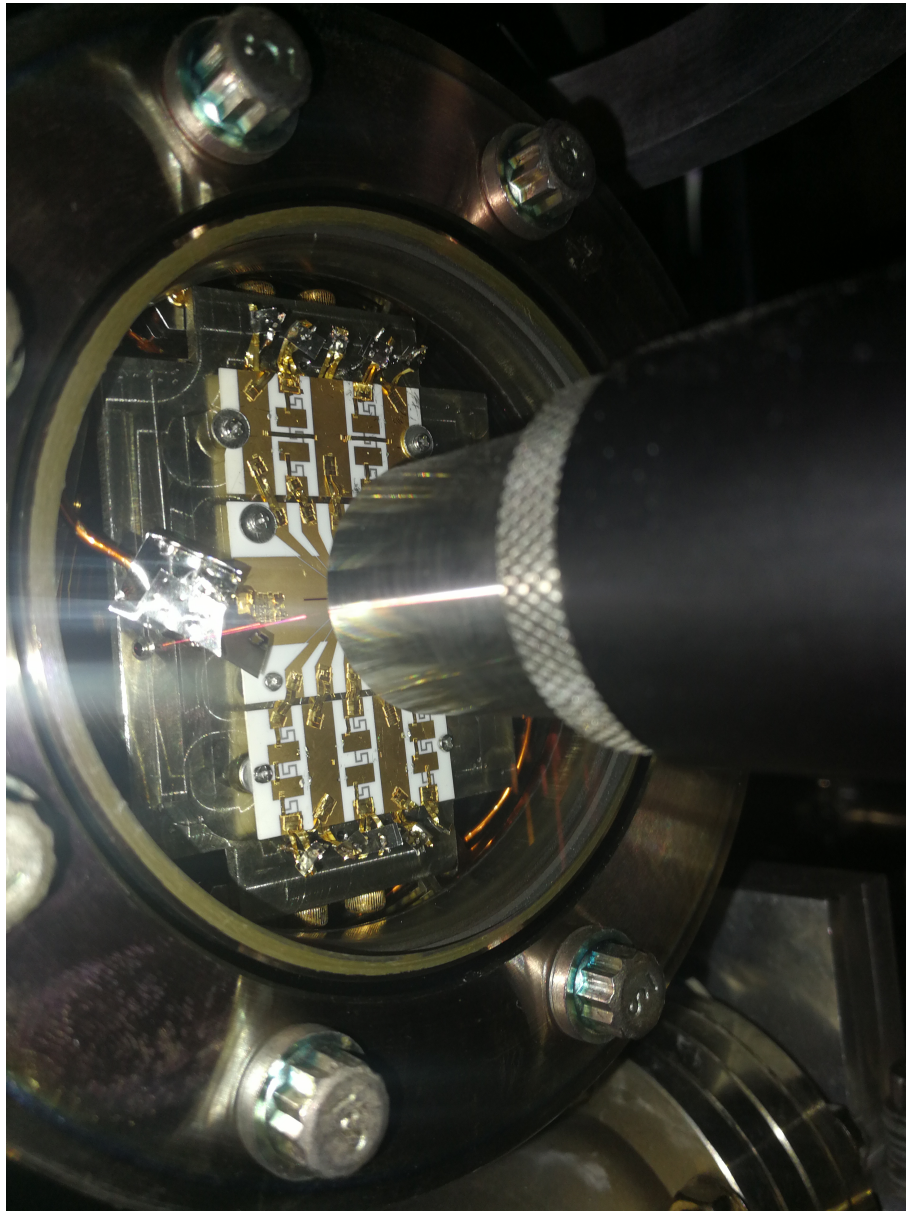


图 5.11 A picture for the trap.

5.3.2 Vacuum system assemble

The main body of the vacuum system consist of a lot of thick stainless steel tubes. A copper gasket is used to seal the connection flange. When we tight the flange bolts and screws, the copper should be clamped and tightly surrounded by the knife edges, and the screws should be tighten in a Zig-Zag way. We should clean all the components except feed-through and view ports several times by ethanol and acetone. We also need to do the air-baking to acquire a chromium oxide coating^[81].

The vacuum system design is shown in the Fig. 5.12. We use a hemisphere for the main chamber part, a Ti pump and a ion pump to keep the UHV. A 19 pin electric feed through is used for the connection of all the DC electrodes.

All the connection component and the ti sublimation pump is from Kert.J.Lesker. The main chamber is from Kimble Physics Inc. The vacuum system need to provide a high vacuum with around 10^{-12} Torr.

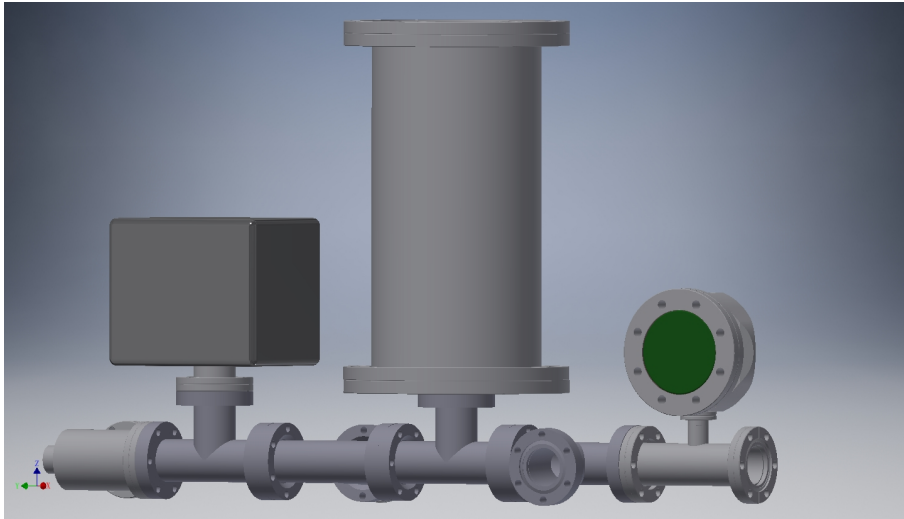


图 5.12 Vacuum system.

5.3.3 Pump and bake process

After we finish the assembling of the vacuum system, we put the system into our big baking oven and connect it to our pumping system, which consist of four level of pumps: mechanical pump, turbo-molecular pump, big ion pump, Ti sublimation pump. We always follow the steps to make the UHV:

1. Connect all 4 level of pump to the vacuum system. Close the valve of big ion pump. Turn off the small ion pump. Open the mechanical pump and turbo-molecular pump

together.

2. Wait 1 or 2 days till the vacuum go to 10^{-6} torr level. Open the baking oven, slowly increase the temperature to 200 °C within 18 hours. Meanwhile, we heat the big ion pump to around 180 °C.
3. During the temperature increasing, the vacuum will increase then decrease. The increasing is because of the increasing temperature and the steam evaporation. The decreasing is because of the pumping out of steam. After 2 or 3 days, the vacuum goes back to 10^{-6} torr level. We do the degassing of Ti sublimation pump and small ion pump.
4. After degassing, We open the valve of the big ion pump and the small ion pump.
5. Wait 2 or 3 days, in general, the small ion pump will show the vacuum in 10^{-7} torr level, the big ion pump will show the vacuum in 10^{-8} torr level, the vacuum level before turbo-molecular pump should be in 10^{-9} torr level.
6. We close the bakeable valve using small torque and disconnect the vacuum system to big ion pump and turbo pump. Turn off the baking oven, cool the system to room temperature within 18 hours.
7. Do the Ti sublimation pump at the room temperature. Close the bakeable valve with suitable torque.

After this process, we can have a UHV system with in one and half week. We have had two accidents in the whole process. They all happened in the step 2, where the vacuum can not reduce to 10^{-6} torr level after reaching 200 °C. This two accidents are all because of the small break on the viewport causing the leakage.

第6章 Trap testing

In the Chapter 5, we describe how we fabricate a monolithic trap and how we make a vacuum system for this trap. After finishing the assembling process, we start to test the performance of the trap. The performance include the loading of the ion, the loading position, control ability of the DC electrodes, secular trap frequency and axial trap frequency, life time of the ion, stable of multiple ions, and heating rate etc. We build a small ion trap system include laser system, control system, image system to load ion, detect ion and measure the parameters of the trap.

6.1 Load $^{171}\text{Yb}^+$ and $^{138}\text{Ba}^+$

Loading ion is the first challenge for the trap test. The first time loading is always difficult because of the uncertainty of laser alignment, image position, and trap potential. You can load the ion only if everything is roughly right. We need to find the reference for each system to make the first ion cloud.

6.1.1 Laser system

We are using a small optical table for the trap testing. The laser is coupled with fiber from the laser system describe in Chapter 2.2.3 and Chapter 2.3.3. We need only 3 laser for loading $^{138}\text{Ba}^+$ ion, which is 493 nm, 650 nm, and 413 nm laser. We put three flipping mirror in the path of these laser and adding three fiber coupler for these three laser. The small table part is similar with the right side in the Fig. 2.5, we use two dichroic mirrors merging three laser, align them to the center of the trap through a lens with $f = 100$ mm. We need to make sure about the overlap of three laser as good as possible.

For loading $^{174}\text{Yb}^+$ and $^{171}\text{Yb}^+$ ion, we need 369 nm, 935 nm, and 399 nm laser. Especially, we need four 369 nm laser with different sideband for Doppler cooling, optical pumping, detection and ionization process of the $^{171}\text{Yb}^+$. So we add a couple part for the system in Fig. 2.3 to couple four 369 nm laser into one fiber. In the small optical table, we only use one fiber collimator for four 369 nm laser. These four laser is absolutely overlap well, which is good for the alignment. We shown the optical system and the image system for $^{171}\text{Yb}^+$ and $^{138}\text{Ba}^+$ in the Fig. 6.1. In order to see $^{171}\text{Yb}^+$ and $^{138}\text{Ba}^+$ together, we make

through these slot even it's not fully cut through. This can be a very important reference for the horizontally alignment. As shown in the Fig. 6.2, when we align the laser near the T structure, we can see the T structure clearly on the CCD. We can recode the four position with the translation state in the image system, so that we can adjust the objective lens to the right regime horizontally. If we make $V_3 = V_4 = V_5 = V_6$, then ion should be at the center position of these four T structure. We adjust the vertical position of the objective lens to see one RF electrode. We adjust the laser hitting the edge of this RF electrode. By changing the horizontal position of laser, we can see the moving of a bright scattering spot on the CCD. When we move the scattering spot in the middle of the CCD, the horizontal position of the laser is roughly right. Then we do the vertical alignment again according to the last paragraph. We can adjust the focus of the image system with the edge of RF electrodes, it should be in the same plane with the ion. We can align the laser and image system roughly right.

6.1.3 Loading procedure

After finish the aligning the laser and the image system. The briefly normal procedure for loading is as follows:

1. Dump the trap to get rid of all unexpected charged particle.
2. Check all the laser: Doppler cooling laser, ionization laser, and repumping laser.
3. Open the oven and keep checking with PMT or CCD.
4. If you see the ion either by CCD or PMT, turn off the oven and block the ionization beam.

For the first loading, even the laser and the image system is align roughly right, it's still not easy to see the ion in the step 3. It's better to use the camera for checking the ion for the first time. Since the alignment of laser and image system is not perfect, we may not see the ion until it become to a big ion cloud. We can increase the all the laser power to reduce the effect of miss alignment. We can use binning function or increase the exposure time of camera to see ion cloud more clearly. During loading process, we need to scan the image system or the laser a little bit to see the ion cloud. According to our experience, scanning the image system could be more helpful for finding the ion cloud. We check if there is a ion cloud by blocking and unblocking the repumping beam. If there is some area shining follow your movement of blocking, it's the ion cloud.

For the first loading, we also need to do the degassing for the atomic oven, especially

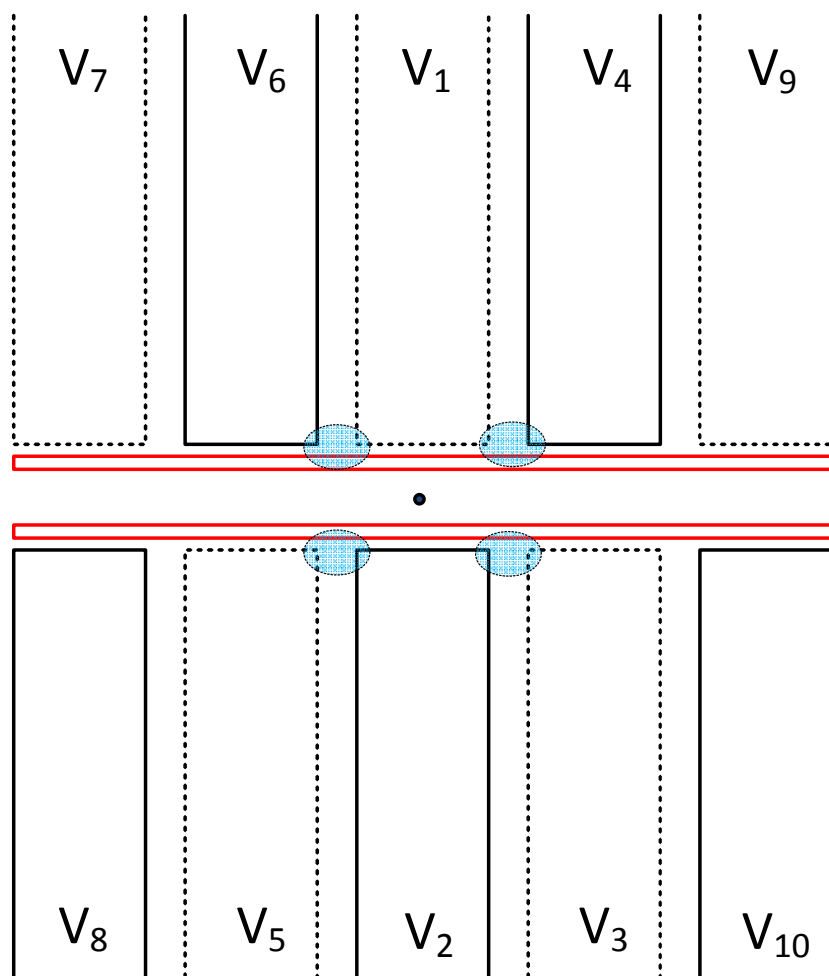


图 6.2 The diagram of the front view of the trap. We can see the RF and DC electrodes in the CCD. The dashed-line electrodes are on the back side in the camera view.

for the $^{138}\text{Ba}^+$ ion. Ba atom is easy to oxidize in the air. There will be an oxide layer on the surface of Ba atom. Only if we heat the atomic oven to the sublimation temperature for oxidize layer or we heat the atomic oven for a long time so that the Ba steam break the oxidize layer. But whenever the oxidize layer is break, there will be a huge atom beam going out of the oven.

When we do the degassing, we need to slowly increase the oven current to keep the vacuum below 10^{-11} torr in the whole process. According to our experience, for Yb ion, the oven current we use to load the ion is around 0.6 of the threshold current when we are testing. For Ba ion, the current is around 0.8 of the threshold current for testing.

After we have the ion cloud, we close the oven, align lasers and image system to find the brightest part, which is the center of the ion cloud. Then we dump the trap and load the ion again. In general, we have have the ion crystal even single ion at this time. If you see the ion cloud, you can lower the RF power to make the cloud crystallize. Then repeat the loading procedure and reduce the oven current to find the right current to load the single ion.

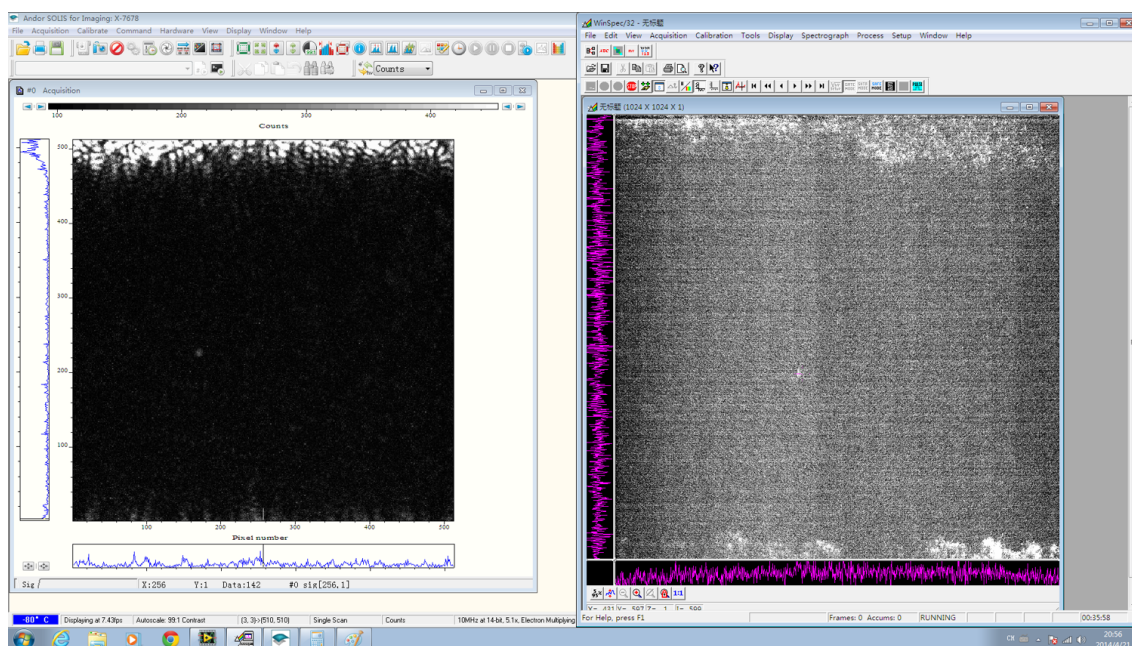


图 6.3 The picture of two camera for Yb and Ba ions. Left side is the Ba ion, right side is the Yb ion.

After we load the single ion, we also need to do several steps to make the trapping condition better. If we do the following step well, we can have a good trap condition. We can have the ion for around half an hour without cooling laser.

1. Adjust the power and the polarization of Doppler cooling laser, detection laser and optical pumping laser.
2. Do the micromotion compensation.
3. Check the angle of principle axes. If the ion is often shaking in one direction, it's better to rotate the principle axes to have more cooling effect on that direction.

6.2 Control ability of the DC electrodes

As shown in the Fig. 6.2, we have 10 DC electrodes can be independently controlled. We briefly introduce how these electrodes affect the axial and radial potential. In this section we will test these effect with ion. We can change the voltage of the electrodes one by one and observe the ion movement to briefly check the function of the electrodes. We use a ISEG High Voltage module to be the voltage source. Since we don't have the enough control precision for ISEG module, we connect the voltage divider to each channel, the ratio is 1:12.

6.2.1 Micromotion compensation

Micromotion compensation is the first thing we need to do after loading of the single ion. Micromotion is the additional term to the motion solution according to the Eq. 2-19. The micromotion terms could be caused by

1. Imperfect geometry configuration.
2. Additional external field.
3. Phase difference between RF electrodes.

These micromotion can not be significantly reduced by cooling^[82], but must be eliminated as small as possible. The ion's equilibrium position is shifted when the first two cases happened. When we change the power of the RF drive signal, the trap depth change, the ion's position will change. This phenomenon can help us to estimate the amplitude of micromotion. We make a switch to change the power of RF field between high level and low level in 8 ns to see the ion moving phenomenon.

We also use a Pico-harp to measure the time correlation of ion's micromotion frequency and its Doppler cooling fluorescence rate. The absorption and emission process of photons will be modulated at the drive frequency due to the micromotion. Pico-harp will show the histogram of the arrival time of the photon on PMT compared to the phase of drive signal as a sine wave, whose frequency equals to the drive frequency. This is a

indicator for the amplitude of the micromotion. If we can reduce the amplitude of the sine curve, we can reduce the micromotion.

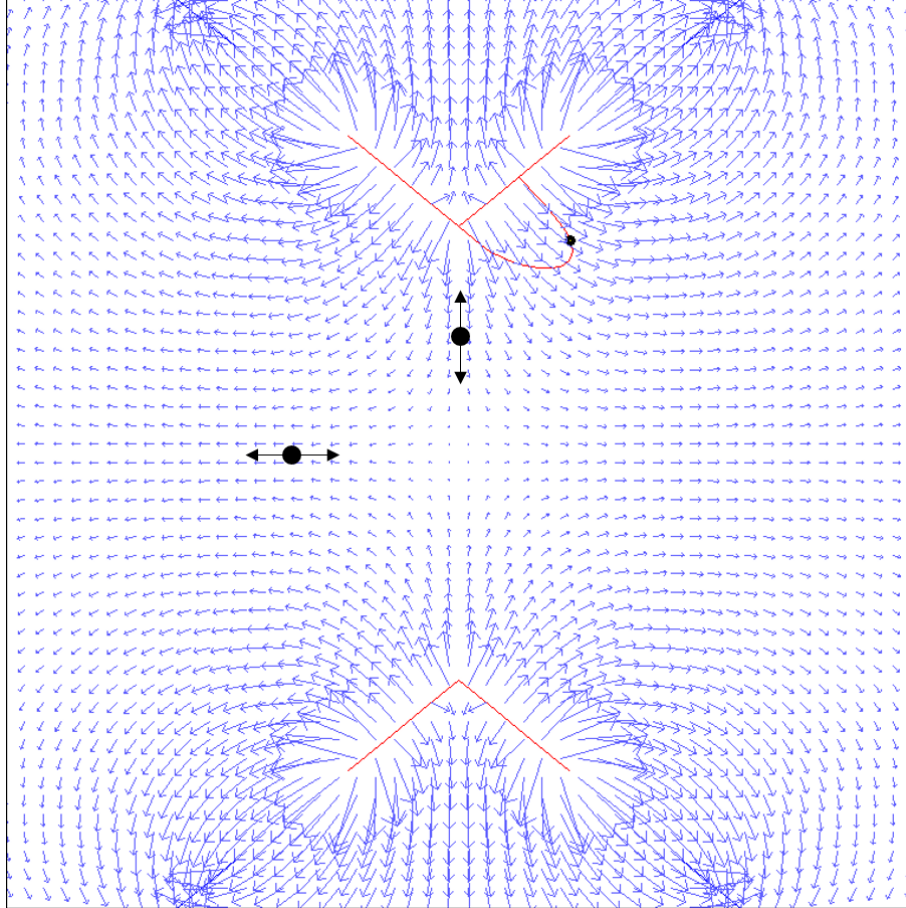


图 6.4 Electric field of the RF electrodes. If ion equilibrium position is at the center, the micromotion direction is show in the figure.

Let's see the micromotion direction in the Fig. 6.4. We show the electric field of the RF electrodes simulated by CPO in the figure. If the ion equilibrium position is not at the center, the micromotion will be along the electric field. The movement phenomenon of ion position with different RF power can indicator the amplitude of micromotion in the vertical direction. The modulated florescence phenomenon can indicate the amplitude of micromotion in the laser direction. If we can eliminate the ion movement and the modulated florescence phenomenon in the same time, we can have a good micromotion condition.

It's better to have the ability for only moving the ion in vertical or horizontal direction. So that we can first move the ion in the vertical direction to eliminate the ion movement phenomenon. Then move the ion in horizontal direction to eliminate the modulated

florescence phenomenon.

We have 10 electrodes, we set the voltage as $V_1 = V_2 = -10$ V, $V_3 = V_4 = V_5 = V_6 = 10$ V for the first loading. The ion shows in the center of the V_1 and V_2 electrodes. We try several combination of electrodes to find the way to move the ion only in vertical and horizontal direction. We use the setting $\delta V_1 = 3$, $\delta V_4 = 10$, $\delta V_6 = 10$ or $\delta V_2 = 3$, $\delta V_3 = 10$, $\delta V_5 = 10$ to move the ion only in vertical direction. We use the setting $\delta V_1 = 2.5$, $\delta V_3 = 10$, $\delta V_5 = 10$ or $\delta V_2 = 2.5$, $\delta V_4 = 10$, $\delta V_6 = 10$ to move the ion only in horizontal direction. We can use these setting to do the micromotion compensation.

6.2.2 Axial and radial frequency measurement

The axial and the radial trap frequency are every important parameter for the experiment. We want to measure the frequency by adding a modulation on the DC electrode. If the modulation frequency is close to the one motion mode frequency of the ion, the ion will be resonance. It's easy measure the axial frequency, We can measure the frequency by this method.

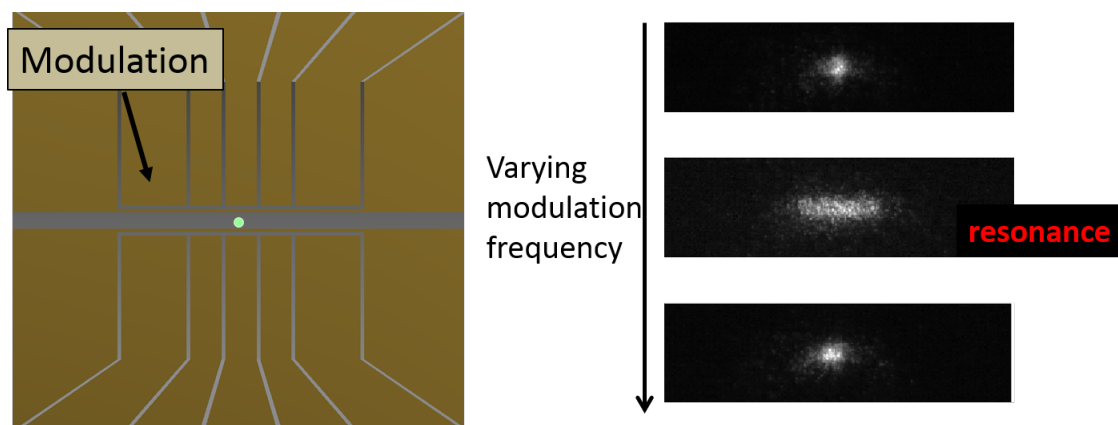


图 6.5 Modulation on the DC electrode. The ion resonance.

We can measure the trap frequency with different voltage setting. We combine V_1, V_2 as a group named center electrode, V_3, V_4, V_5, V_6 as a group named inner electrode, and V_7, V_8, V_9, V_{10} as a group named outer electrode symmetrically. We change the same amount for the electrodes in one group. The data is shown in the Fig. 6.6. When we change the center electrode, the outer and inner voltage is $V_{outer} = 0$ V, $V_{inner} = 4$ V. When we change the inner electrode, the outer and center voltage is $V_{outer} = 0$ V, $V_{center} = -7.4$ V. When we change the outer electrode, the inner and center voltage is $V_{inner} = 4$ V, $V_{center} = -7.4$ V.

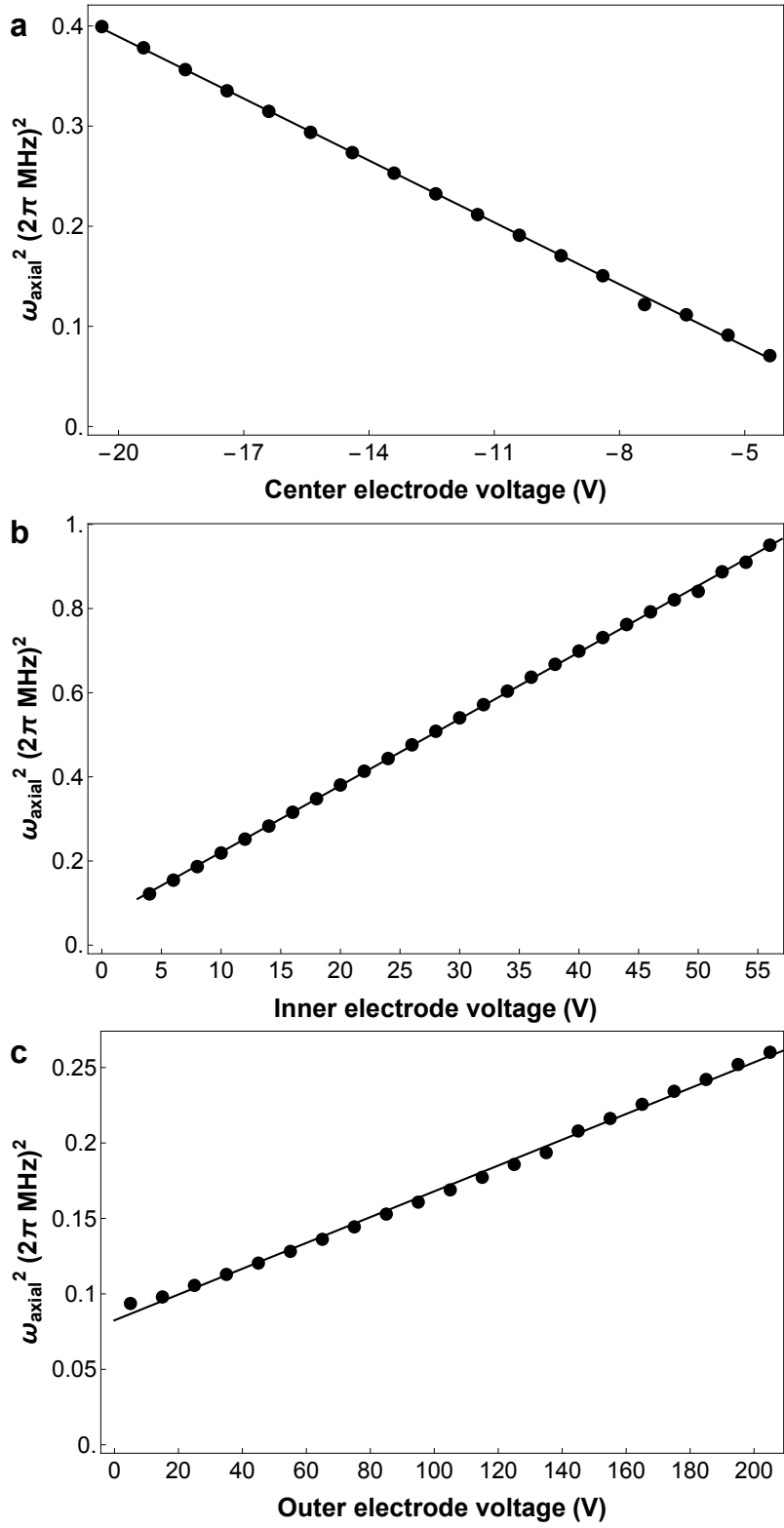


图 6.6 The axial frequency depend on the different voltage setting.

According to the Eq. 4-2, we can write the total axial potential as

$$\phi_{axial} = V_{center}\phi_{center,axial} + V_{inner}\phi_{inner,axial} + V_{outer}\phi_{outer,axial} + \phi_{offset} \quad (6-1)$$

where the ϕ_{axial} is the electrode basis function for three set of electrodes, ϕ_{offset} is some unexpected electric field. Since the axial frequency is proportional to the quadratic coefficient of $\sqrt{\phi_{axial}}$. So we can write the axial frequency as

$$\omega_{axial} = 2\pi\sqrt{aV_{center} + bV_{inner} + cV_{outer} + offset} \quad (6-2)$$

By the fitting of the data show in the Fig. 6.6, we can know $a = 0.0206069 \text{ s}^{-2}\text{V}^{-1}$, $b = 0.015839 \text{ s}^{-2}\text{V}^{-1}$, $c = 0.000854609 \text{ s}^{-2}\text{V}^{-1}$ and $offset = 0.2149809 \text{ s}^{-2}$.

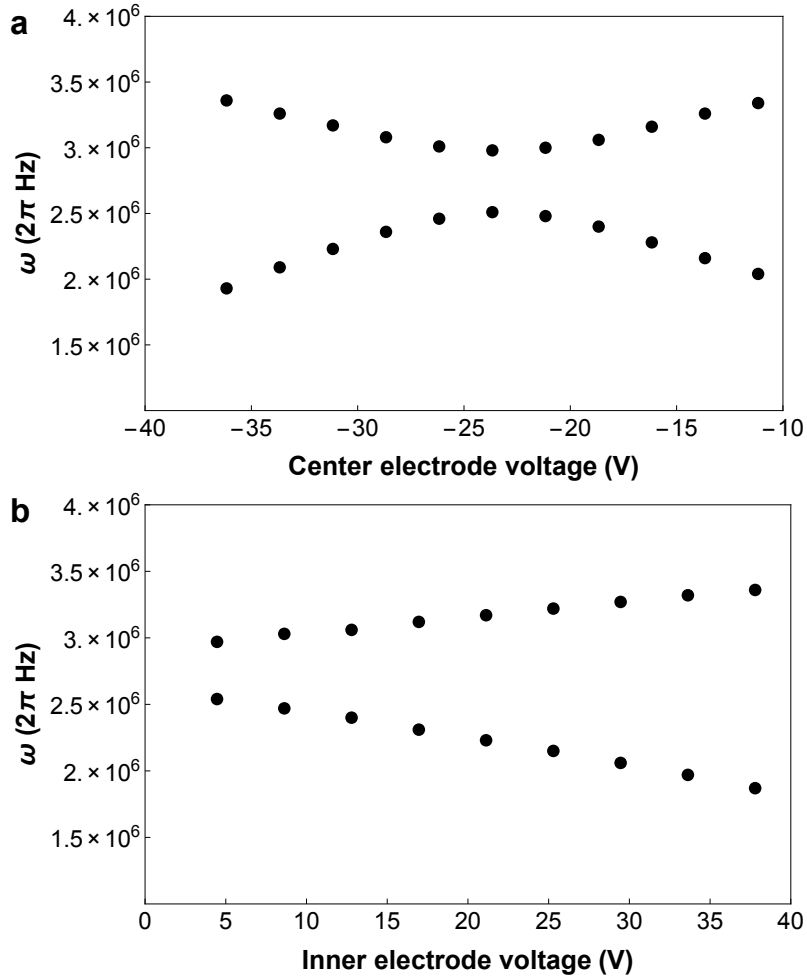


图 6.7 The radial frequency depend on the different voltage setting.

We can use the same method to measure the radial secular frequency. We can see

the resonance twice because we have two radial motion mode, which is along the two principle axes. So we can see the ion resonance in the two direction, shaking in the vertical direction and shaking in the focal direction, at the frequency of two mode.

We can see the separation of two motion mode frequency. This is because of the symmetry break due to the voltage we apply on the DC electrodes. We show the measured data in the Fig. 6.7. In the figure a, we show the frequency of two mode depend on the voltage changing of center electrode. The other setting is $V_{inner} = 11.9583$ V, $V_{outer} = 0$ V, $V_{RF} = 300$ V, $\Omega_T = 39$ MHz. In the figure b, we show the frequency of the two mode depend on the voltage changing of inner electrodes. The other setting is $V_{center} = -18.6667$ V, $V_{outer} = 0$ V, $V_{RF} = 300$ V, $\Omega_T = 39$ MHz.

6.2.3 Compare to the simulation data

We want to compare the measured data to the simulated trap frequency. If we have some model to make the simulated data well fit to the real data, we can use this model to predict the effect of various voltage setting.

We first compare the measured axial frequency result to the simulated result. We can write the measured axial frequency as

$$\begin{aligned} \phi_{axial} = & \eta_1 V_{center} \phi_{center,sim,axial} + \eta_2 V_{inner} \phi_{inner,sim,axial} \\ & + \eta_3 V_{outer} \phi_{outer,sim,axial} + \phi_{offset} \end{aligned} \quad (6-3)$$

where η_1 , η_2 and η_3 is the geometrical parameter indicate the different between the idea and the real structure. We use three linear fitting to fit three value of η , the fitting is shown in the Fig. 6.8. We can know the result as $\eta_1 = 0.970271$, $\eta_2 = 0.875818$, and $\eta_3 = 0.656036$. The linear fitting is quite well as shown in the figure.

Then, we compare the measured data to the simulated data of radial motion mode. We want to find the suitable parameter for the simulation. This part is more difficult than the axial part. We still use the geometrical parameter to describe the different of ideal and real structure. We need to consider the the other effect such as the additional electric field and the rotation of the principle axes. The axes rotation results the change of frequency does not follow linearly with voltage, which is shown in the Fig. 6.7. This makes the fitting more challenging. We can write the radial potential as follow:

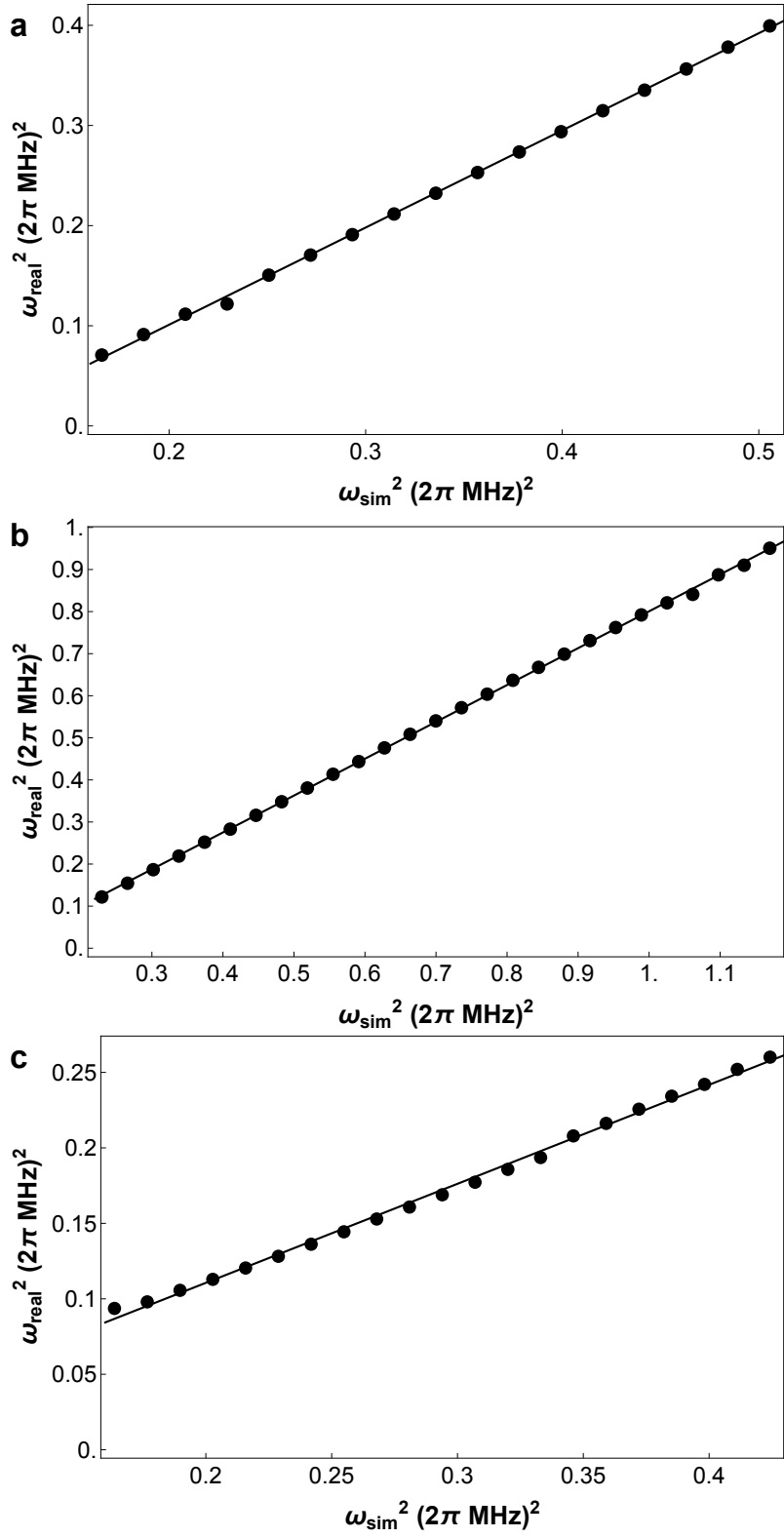


图 6.8 Fitting for the measured data and simulated data.

$$\begin{aligned}\phi_{radial} &= \phi_{pseudo} + \eta'_1 V_{center} \phi_{center,sim,radial} + \eta'_2 V_{inner} \phi_{inner,sim,radial} \\ &+ \eta'_3 V_{outer} \phi_{outer,sim,radial} + \phi_{offset}\end{aligned}\quad (6-4)$$

where $\phi_{pseudo} = \frac{e}{4m\Omega_T^2} (V_{rf,j} \nabla \phi_{rf,j})^2$ is the pseudo potential, $\eta'_1, \eta'_2, \eta'_3$ are the geometrical parameter, the ϕ_{offset} is some additional potential. We need to find the suitable value of $\eta'_1, \eta'_2, \eta'_3$ and ϕ_{offset} to make the simulation close to reality. ϕ_{offset} is not easy to describe in the simulation, but we can decompose the potential to the summation of the potential for center and inner electrodes. This means we can add two term, which are $V_{center,off}$ and $V_{inner,off}$, in the simulation to simulate the ϕ_{offset} . When we do the simulation, we use $V_{center,sim} = V_{center,real} + V_{center,off}$ and $V_{inner,sim} = V_{inner,real} + V_{inner,off}$. So this means we need to fit five parameters to find a good model, which are $\eta'_1, \eta'_2, \eta'_3, V_{center,off}$ and $V_{inner,off}$.

If we don't have the axes rotation effect, when we only change the voltage of center electrode, we know $\Delta\omega_x^2 \approx \eta'_1 \Delta V_{center} \phi_{center,sim,x}$ and $\Delta\omega_y^2 \approx \eta'_1 \Delta V_{center} \phi_{center,sim,y}$, according to Eq. 4-4 and Eq. 6-4. So $\Delta\omega_x^2 / \Delta\omega_{x,sim}^2 \approx \Delta\omega_y^2 / \Delta\omega_{y,sim}^2 \approx \eta'_1$. We know $\Delta V_{center}, \omega_{x,sim}$ and $\omega_{y,sim}$ from simulation, so we can use the linear fit to find η'_1 . We find some region for DC electrodes so that the principle axes rarely rotate. In the data in Fig. 6.7, the whole data in figure b and part of data in figure a are in compliance with this requirement. We use these data to fit η'_1 and η'_2 .

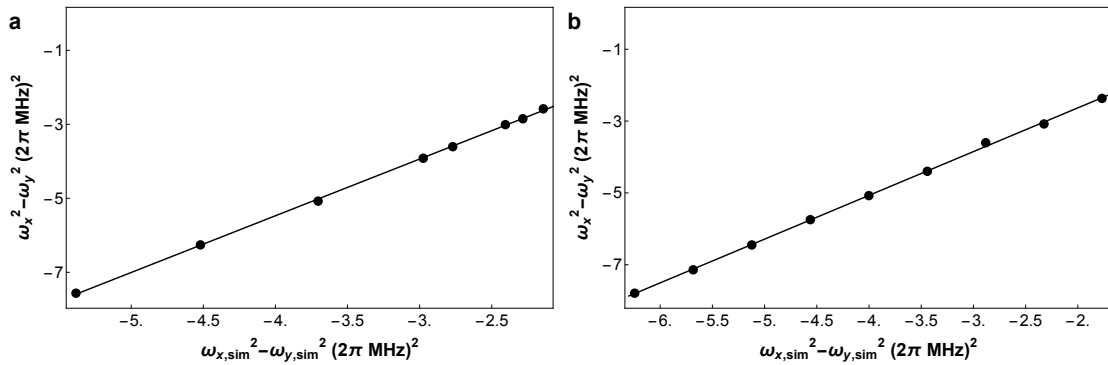


图 6.9 Figure a is the fitting when we only change the center electrode. Figure b is the fitting when we only change the inner electrode.

The fitting result is $\eta'_1 = 1.53295$ and $\eta'_2 = 1.21837$. Then we can find out $V_{center,off} = 19 \text{ V}$ and $V_{inner,off} = 10 \text{ V}$ by fitting. The fitting result is shown in

Fig. 6.10 The figure shows a good fitting for the real data, which means our simulation

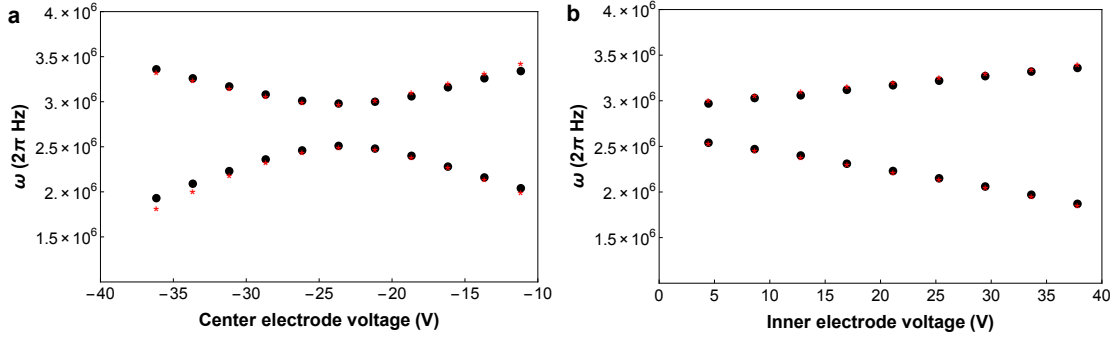


图 6.10 The star mark is the simulated data point. This show the well fitting with the real data.

data is quite good. We can use this model as a tool to predict the performance of the trap.

6.3 Heating rate measurement

Heating rate is a very important parameter for the trap. The big heating will influence the multi-ion quantum logic gate fidelities and the quantum simulation related to the phonon. We use two method to measure the heating rate of our trap. One is the Doppler re-cooling method, the other one is the sideband cooling method.

6.3.1 Doppler re-cooling method

The fluorescence rate from an ion will be impacted by the motional temperature due to the Doppler effect. By monitoring the fluorescence as a function of time during Doppler cooling of an hot ion, we can calculate the initial temperature of the ion. This is the Doppler re-cooling method. We use this method to measure the heating rate in the version two of our trap. The result is shown in the Fig. 6.11. The heating rate is $\dot{n} \approx 500$ phonon/ms with the secular frequency $\omega = 2\pi \times 3$ MHz.

6.3.2 Sideband cooling method

We also use the pulse laser to do the sideband cooling^[83,84]. We are using a pulse laser called "Paladin", from Coherent. It is a industrial laser with around 4 W output power at 355 nm. The repetition rate is fixed at 120.15344 MHz. We use a feed-forward phase-locked loop to keep the frequency difference of two specific comb as a constant. The diagram of the pulse laser system is shown in the Fig. 6.12. We can use this pulse laser to make the Raman transition between the hyperfine structure of $^{171}\text{Yb}^+$. We can

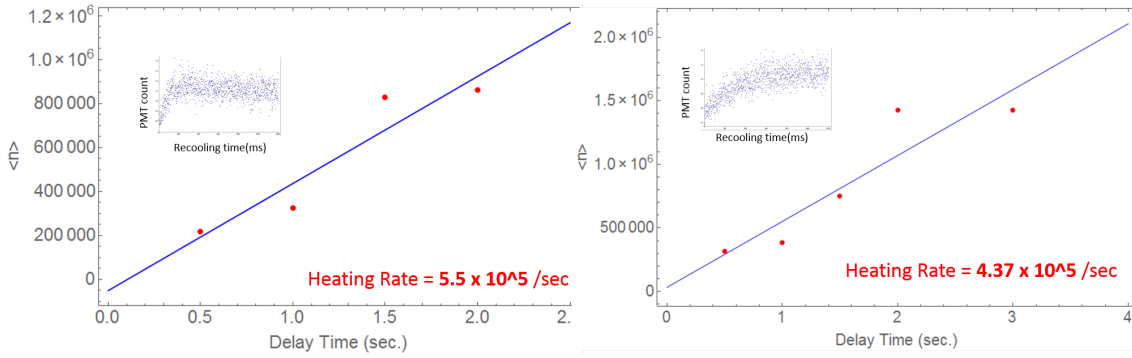


图 6.11 The data of re-cooling method

also do the sideband cooling and phonon operation with this pulse laser. We have done a lot of experiment with this technique in the references^[85–92]. We are using the DC setting as $V_1 = -21.9$ V, $V_2 = -26.8$ V, $V_3 = 15.9$ V, $V_4 = 15.9$ V, $V_5 = 21.5$ V, $V_6 = 21.5$ V and $V_7 = V_8 = V_9 = V_{10} = 0$. A spectroscopy using Raman beam is shown in the Fig. 6.13. You can see the carrier and two motion sideband in the figure.

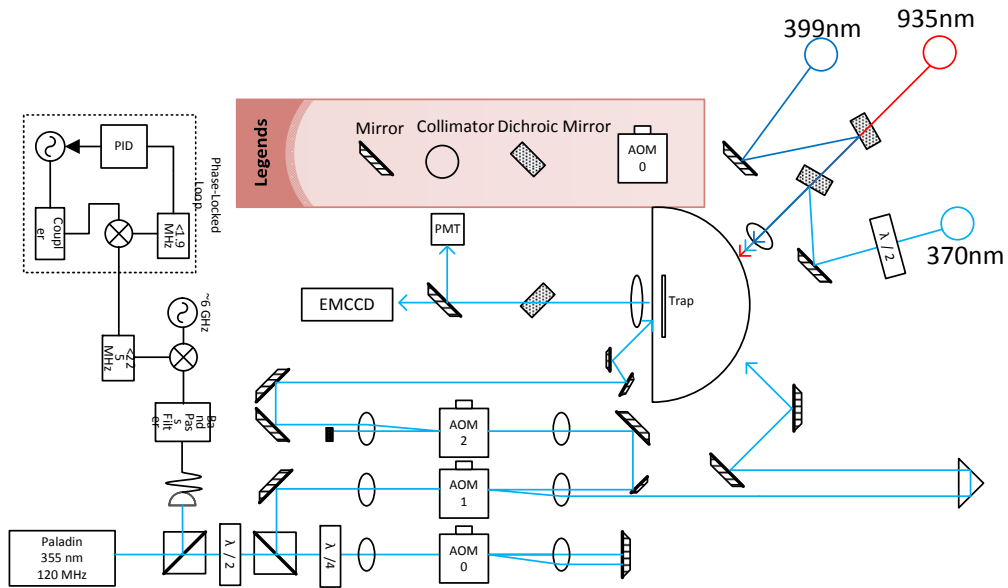


图 6.12 The diagram of two path of Raman beam.

After sideband cooling, we can estimate the average phonon number of the ion by fitting the oscillation of the blue sideband transition. We insert some period with no laser after sideband cooling before the probing cycle. By seeing the change of average phonon of the ion depending on delay time, we can know the heating rate of our trap. We can measure the heating rate of two motion mode.

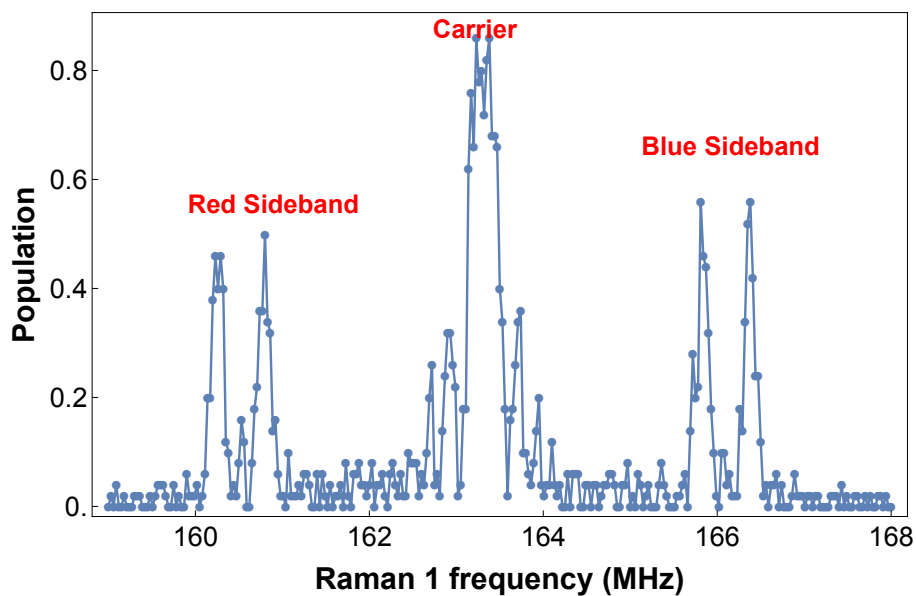


图 6.13 Spectroscopy using Raman beam

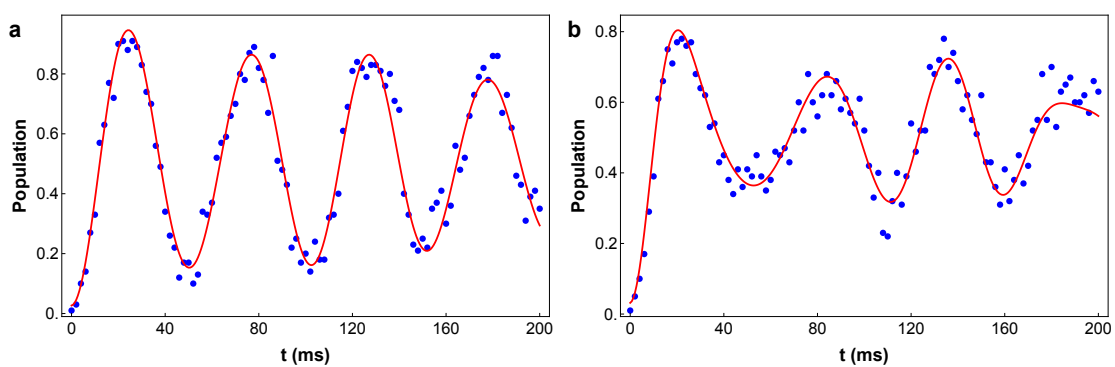


图 6.14 Rabi oscillation of blue sideband right after sideband cooling and oscillation with 1 ms delay

Fig. 6.14 shows the Rabi oscillation of the blue sideband after sideband cooling and the signal with 1 ms delay. We can fit the signal to the signal of a thermal state to find the average phonon number $\bar{n} = 0.1 \pm 0.068$. With 1 ms delay, the can know the average phonon number $\bar{n} = 0.85 \pm 0.21$. We can know the heating rate of this motion mode is $\dot{\bar{n}}_1 \approx 0.75 \pm 0.22$ phonon/ms with the secular frequency $\omega_1 = 2\pi \times 3.04$ MHz .

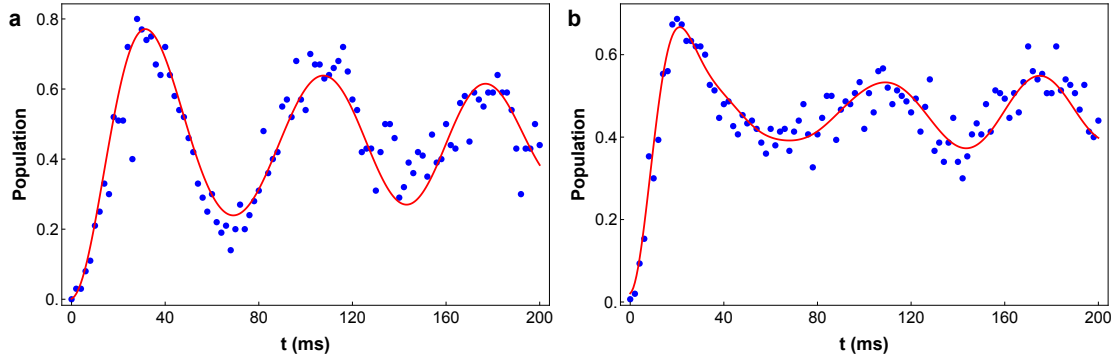


图 6.15 Rabi oscillation of blue sideband right after sideband cooling and oscillation with 1 ms delay

Fig. 6.15 shows the Rabi oscillation of the blue sideband after sideband cooling and the signal with 1 ms delay. We can fit the signal to the signal of a thermal state to find the average phonon number $\bar{n} = 0.28 \pm 0.16$. With 1 ms delay, the can know the average phonon number $\bar{n} = 1.96 \pm 0.47$. We can know the heating rate of this motion mode is $\dot{\bar{n}}_2 \approx 1.68 \pm 0.63$ phonon/ms with the secular frequency $\omega_2 = 2\pi \times 2.53$ MHz.

You can see the heating rate result of two method is quite different. This is not the problem with the measured method, it's because the trap we are measured is different. We used the Doppler re-cooling method to measure the old version of the trap, which has the stage shape RF electrode and cutting through slot. This means we have a huge exposure area of RF electrode to the ion, which may increase the effect of electric field noise causing the anomalous heating. The other reason causing the big heating rate is the micromotion. Micromotion will introduce the noise from RF drive signal casing the anomalous heating. With the old design of the trap, it's difficult to have a stable micromotion situation. The heating rate we measure is extremely big. The trap we measured with sideband cooling method is the newest version of the trap. We use the slope corner to be the RF electrode to reduce the exposure area of RF electrode. We also eliminate the RF electrode shaking effect which give us a stable micromotion condition. So the heating rate is reduced a lot now.

6.3.3 Principle axes angle measurement

In the Chapter. 4.4.3, we show the ability of changing principle axes with DC electrodes. Here, we use Raman beam to measure the angle of two principle axes and compare the angle to the simulated data. According to the reference^[93], we can write the Rabi frequency of the first blue and red sideband transition for one motion mode as

$$\Omega_{b,1} = \Omega_{r,1} \approx \sqrt{n}\eta_1\Omega_0 \approx \sqrt{n}\eta_1\Omega_c \quad (6-5)$$

$$\Omega_{b,2} = \Omega_{r,2} \approx \sqrt{n}\eta_2\Omega_0 \approx \sqrt{n}\eta_2\Omega_c \quad (6-6)$$

where η_1, η_2 are the Lamb-Dicke parameters for two motion mode, Ω_c , is the Rabi frequency of carries transition. We know

$$\eta_1 = \vec{k} \cdot \vec{x}_0 = \sqrt{\hbar/2m\omega_m}k \cos(\theta_1) \quad (6-7)$$

where θ_1 the included angle between the first axis and the effective wave vector \vec{k} . If we measure the Rabi frequency of carrier and blue sideband transition, we can calculate θ_1 . With the same method, we can calculate θ_2 . We can compare these data to simulated one.

With the data shown in Fig. 6.14 and Fig. 6.15, we can know the π -time of blue sideband transition for two motion mode as $\Omega_{b,1} = 25.475$ ms and $\Omega_{b,2} = 35.507$ ms. We can also measure the π -time of carrier transition with near ground state as $\Omega_c = 2.372$ ms. We can know $\eta_1/\eta_2 = \Omega_{b,1}/\Omega_{b,2} = 35.507/25.475 = 1.394$. Since $\theta_1 + \theta_2 = \pi/2$ and $\cos(\theta_1)/\cos(\theta_2) = \eta_1/\eta_2 = 1.394$, we can solve two angle as $\theta_1 = 0.6223$ and $\theta_2 = 0.9485$. The simulated data using the model we find in Chapter. 6.2.3 is $\theta - 1 = 0.4207$, $\theta_2 = 1.1501$, $\omega_1 = 2\pi \times 2.414$ MHz and $\omega_2 = 2\pi \times 3.034$ MHz. This simulated result is quite acceptable comparing to the real data.

With the control of the angle of principle axes and the secular frequency of two motion mode. We make the voltage setting as $V_1 = -0.212$ V, $V_2 = -0.962$ V, $V_3 = 16.62$ V, $V_4 = 16.62$ V, $V_5 = 22.83$ V, $V_6 = 22.83$ V and $V_7 = V_8 = V_9 = V_{10} = 0$. We show the simulated potential in Fig. 6.16. All the simulated parameters are $\omega_1 = 2\pi \times 3.739$ MHz, $\omega_2 = 2\pi \times 1.186$ MHz, $\omega_z = 2\pi \times 0.895$ MHz, $\theta_1 = 0.066$, and $\theta_2 = 1.505$. According to reference^[94], we can make the two-dimensional ion crystal. In the reality, we load the ion crystal which is shown in the Fig. 6.17. The measured parameters are $\omega_1 = 2\pi \times 3.770$ MHz, $\omega_2 = 2\pi \times 1.137$ MHz, $\omega_z = 2\pi \times 0.800$. This show the good work of simulation

again. We may do some simulation with these two-dimensional ion crystal in the future.

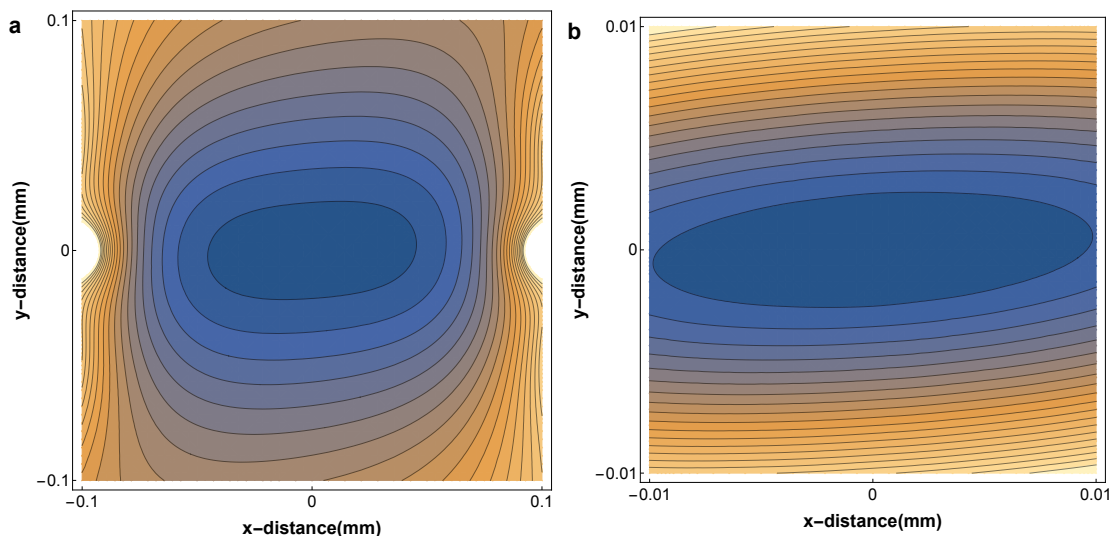


图 6.16 Simulated potential with the DC setting for two-dimensional ion crystal.

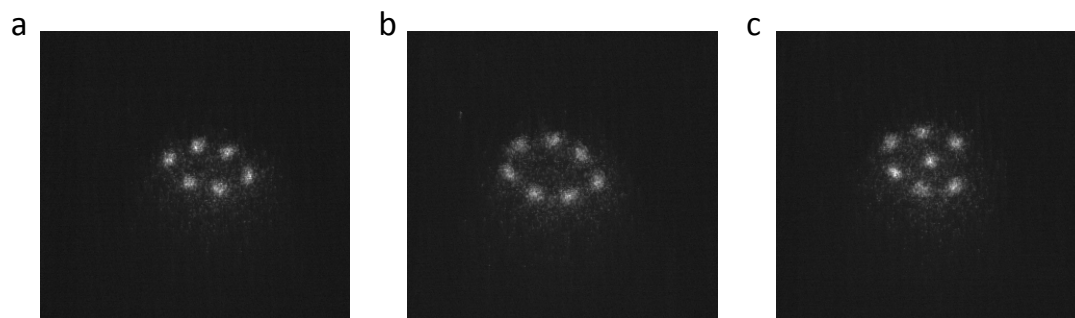


图 6.17 The figure of two-dimensional ion crystal with 6, 7 and 8 ions.

6.4 Remain problems

We have solved a lot of problems in the past iterations, which include short circuit of electrodes due to the oven coating, unstable for micromotion condition due to the shaking of RF electrodes, the extremely big heating rate and etc. For the newest version, we still have some problem unsolved.

One of the most annoying problem is the charging problem of the 355 nm beam, which is used for the Raman transition. We always use around 50 mW of each Raman path to have the around $1 \mu\text{s}$ π -time of carrier transition. After Doppler cooling, the average phonon number of ion is around 25, $\bar{n} = 25$. So we used 40 to 60 sideband cycle

to cool the ion down to the ground state. Every time after we have applied hundreds of sideband cooling process, the micromotion will change a lot, which means the π -time of carrier transition will increase around 5 times. We can adjust the DC voltage around 1 V to compensate it. This makes a lot of trouble in the experiment. We can't do a lot of Raman operation in this situation.

The possible solutions are increasing the distance of RF electrodes, or do another gold coating to reduce the insulating surface.

第7章 Conclusion and outlook

In the thesis, I showed my work about the development of our system. These development, include realization of the new monolithic trap, improving our single qubit gate fidelity, extend the coherence time of single qubit and so on. We make the new world record of the coherence time for a single qubit. We also went through the iteration, which consist of design, fabrication, test, modification, several times to have a working trap in the final. Meanwhile doing this two project, we made a lot of small improvement on our system. For example, we change the rod of the four-rod trap to reduce the heating rate, we improve the microwave gate system to have the very high gate fidelity, we totally rearrange the laser system for $^{138}\text{Ba}^+$ and $^{171}\text{Yb}^+$ to have more power to the chamber. All the small improvements can converge into big progress.

The next step for the quantum memory project is adding the magnetic shield on our system to eliminate the environment magnetic field noise. We can also add the feed-forward system to cancel the 50 Hz noise in the system. We can try to make the hours level quantum single qubit memory.

We can also try the multi ion memory zone. If we have the ability to operate the single ion and cool the trap to 4K, we can easily apply out method to the multi ion. We can have the memory zone of quantum computer.

The other possible direction is to study the protection technique for entanglement state. If we can extend the coherence time of entanglement state one order magnification longer, it could be a good technique for quantum computing.

For the monolithic trap, we need more study about the heating rate. We may try some different gold coating technique or different subtract to see test the heating rate again. We also need to find the charging area and find some way to avoid it.

Accidentally, we realize the two-dimensional ion crystal in our monolithic trap. We can use all the old setting to do the quantum simulation or quantum operation on the 2D crystal other than 1D chain. We don't have the rotating problem in the penny trap. So it would be a perfect platform to study new physics.

插图索引

| | | |
|--------|---|----|
| 图 2.1 | Our four-rod trap | 8 |
| 图 2.2 | Energy level of $^{171}\text{Yb}^+$ | 9 |
| 图 2.3 | Diagram of the 370 laser system. | 12 |
| 图 2.4 | Energy level of $^{138}\text{Ba}^+$ | 13 |
| 图 2.5 | Diagram of the laser system used for $^{138}\text{Ba}^+$ | 15 |
| 图 2.6 | Image system for $^{171}\text{Yb}^+$ and $^{138}\text{Ba}^+$ ions. | 16 |
| 图 2.7 | Camera image of two ions | 16 |
| 图 3.1 | Schematic diagram of a trapped-ion system with two species. | 19 |
| 图 3.2 | The microwave and laser control system. | 20 |
| 图 3.3 | Time sequence of switch control. Mechanical shutter should open 50 ms before AOM and EO pulse picker. | 21 |
| 图 3.4 | Diagram of CPMG and KDD_{xy} | 24 |
| 图 3.5 | Filter function. | 27 |
| 图 3.6 | Filter function. | 28 |
| 图 3.7 | Phase noise measured by Agilent PXA spectrum analyzer | 30 |
| 图 3.8 | Measured result and fitting result for 50 Hz and 150 Hz | 31 |
| 图 3.9 | Ramsey contrasts $\langle \cos(2F_N(T)) \rangle$ depending on the total evolution time for various numbers of pulses. | 33 |
| 图 3.10 | AD9910 evaluation board | 34 |
| 图 3.11 | Rabi oscillation till 100 period. | 36 |
| 图 3.12 | Fidelity as a function of the number of steps for each randomized sequence. | 37 |
| 图 3.13 | Average fidelity as a function of the number of steps for each computational sequence. | 37 |

| | | |
|--------|--|----|
| 图 3.14 | The time diagram of two FPGA..... | 39 |
| 图 3.15 | All the single shot population results after 10 minutes with dynamical decoupling | 40 |
| 图 3.16 | min10 | 41 |
| 图 3.17 | processt | 42 |
| 图 3.18 | BlochSphere | 42 |
| 图 4.1 | Weakness of other type of trap. a , Assemble error b , Surface trap has relatively weak potential. It is subject to environmental noises. | 45 |
| 图 4.2 | Cutaway view of three-layer trap and our new designed trap | 46 |
| 图 4.3 | 3D model of the structure design in Auto Inventor..... | 46 |
| 图 4.4 | Editing electrodes in CPO | 49 |
| 图 4.5 | Views and exporting data in CPO | 51 |
| 图 4.6 | Electric field and pseudo-potential simulated by CPO | 52 |
| 图 4.7 | 3D model of our monolithic trap..... | 54 |
| 图 4.8 | The secular frequency ω depends on the distance D | 55 |
| 图 4.9 | The secular frequency ω depends on the angle θ | 55 |
| 图 4.10 | The secular frequency ω depends on the RF electrode hight H | 56 |
| 图 4.11 | The secular frequency ω depends on all three parameters..... | 56 |
| 图 4.12 | Design of the GTRI trap | 57 |
| 图 4.13 | 10 electrodes basis function..... | 59 |
| 图 4.14 | Potential for 10 setting of DC electrodes voltage | 60 |
| 图 4.15 | Pure radial potential for DC electrodes and total radial potential | 61 |
| 图 5.1 | Three step to make the slop | 64 |
| 图 5.2 | SEM image of only cutting the gold..... | 65 |
| 图 5.3 | SEM image of cutting through the alumina | 66 |
| 图 5.4 | Optical microscope image of cutting deep | 67 |

| | | |
|--------|--|----|
| 图 5.5 | Schematic diagram of the low-pass filter..... | 68 |
| 图 5.6 | Schematic diagram of the low-pass filter..... | 69 |
| 图 5.7 | Diagram of customized wire bonding holder | 70 |
| 图 5.8 | Diagram of how to connect the third and the fourth low-pass filter to the first two..... | 70 |
| 图 5.9 | 3D model of the holder and connection with trap, low-pass filter and chamber. | 71 |
| 图 5.10 | We increase the crosswise ribbon to increase the strength of the attached part. | 73 |
| 图 5.11 | A picture for the trap. | 73 |
| 图 5.12 | Vacuum system. | 74 |
| 图 6.1 | Diagram of the laser alignment and the image system for $^{171}\text{Yb}^+$ and $^{138}\text{Ba}^+$ | 77 |
| 图 6.2 | The diagram of the front view of the trap. We can see the RF and DC electrodes in the CCD. The dashed-line electrodes are on the back side in the camera view..... | 79 |
| 图 6.3 | The picture of two camera for Yb and Ba ions. Left side is the Ba ion, right side is the Yb ion. | 80 |
| 图 6.4 | Electric field of the RF electrodes. If ion equilibrium position is at the center, the micromotion direction is show in the figure..... | 82 |
| 图 6.5 | Modulation on the DC electrode. The ion resonance. | 83 |
| 图 6.6 | The axial frequency depend on the different voltage setting..... | 84 |
| 图 6.7 | The radial frequency depend on the different voltage setting..... | 85 |
| 图 6.8 | Fitting for the measured data and simulated data. | 87 |
| 图 6.9 | Figure a is the fitting when we only change the center electrode. Figure b is the fitting when we only change the inner electrode..... | 88 |
| 图 6.10 | The star mark is the simulated data point. This show the well fitting with the real data. | 89 |
| 图 6.11 | The data of re-cooling method..... | 90 |
| 图 6.12 | The diagram of two path of Raman beam. | 90 |

| | | |
|--------|--|-----|
| 图 6.13 | Spectroscopy using Raman beam..... | 91 |
| 图 6.14 | Rabi oscillation of blue sideband right after sideband cooling and oscillation with 1 ms delay | 91 |
| 图 6.15 | Rabi oscillation of blue sideband right after sideband cooling and oscillation with 1 ms delay | 92 |
| 图 6.16 | Simulated potential with the DC setting for two-dimensional ion crystal.... | 94 |
| 图 6.17 | The figure of two-dimensional ion crystal with 6,7 and 8 ions. | 94 |
| 图 A.1 | | 112 |
| 图 A.2 | | 113 |
| 图 A.3 | | 113 |
| 图 A.4 | | 114 |
| 图 A.5 | | 115 |

表格索引

| | | |
|-------|---|----|
| 表 3.1 | DDS Profile | 35 |
| 表 4.1 | Simulated and practical data for three-layer trap | 53 |
| 表 4.2 | Simulated data for our trap and GTRI trap | 58 |
| 表 4.3 | Simulated data for our trap and three-layer trap | 58 |
| 表 4.4 | Simulated data for our trap and three-layer trap | 59 |

公式索引

| | |
|---------------|----|
| 公式 2-1 | 4 |
| 公式 2-2 | 4 |
| 公式 2-3 | 4 |
| 公式 2-4 | 5 |
| 公式 2-5 | 5 |
| 公式 2-6 | 5 |
| 公式 2-7 | 5 |
| 公式 2-8 | 5 |
| 公式 2-9 | 5 |
| 公式 2-10 | 6 |
| 公式 2-11 | 6 |
| 公式 2-12 | 6 |
| 公式 2-13 | 6 |
| 公式 2-14 | 6 |
| 公式 2-15 | 6 |
| 公式 2-16 | 7 |
| 公式 2-17 | 7 |
| 公式 2-18 | 7 |
| 公式 2-19 | 7 |
| 公式 2-20 | 8 |
| 公式 3-1 | 22 |
| 公式 3-2 | 24 |
| 公式 3-3 | 24 |

| | |
|---------------|----|
| 公式 3-4 | 24 |
| 公式 3-5 | 25 |
| 公式 3-6 | 25 |
| 公式 3-7 | 25 |
| 公式 3-8 | 25 |
| 公式 3-9 | 25 |
| 公式 3-10 | 25 |
| 公式 3-11 | 25 |
| 公式 3-12 | 25 |
| 公式 3-13 | 25 |
| 公式 3-14 | 26 |
| 公式 3-15 | 26 |
| 公式 3-16 | 26 |
| 公式 3-17 | 26 |
| 公式 3-18 | 26 |
| 公式 3-19 | 26 |
| 公式 3-20 | 26 |
| 公式 3-21 | 26 |
| 公式 3-22 | 27 |
| 公式 3-23 | 28 |
| 公式 3-24 | 28 |
| 公式 3-25 | 29 |
| 公式 3-26 | 29 |
| 公式 3-27 | 30 |
| 公式 3-28 | 30 |
| 公式 3-29 | 31 |

公式索引

| | |
|---------------|----|
| 公式 3-30 | 31 |
| 公式 3-31 | 32 |
| 公式 3-32 | 32 |
| 公式 4-1 | 47 |
| 公式 4-2 | 52 |
| 公式 4-3 | 52 |
| 公式 4-4 | 53 |
| 公式 4-5 | 60 |
| 公式 4-6 | 60 |
| 公式 4-7 | 62 |
| 公式 6-1 | 85 |
| 公式 6-2 | 85 |
| 公式 6-3 | 86 |
| 公式 6-4 | 88 |
| 公式 6-5 | 93 |
| 公式 6-6 | 93 |
| 公式 6-7 | 93 |

参考文献

- [1] Feynman R P. Simulating physics with computers[J]. International journal of theoretical physics, 1982, 21(6): 467–488.
- [2] Deutsch D. Quantum theory, the church-turing principle and the universal quantum computer [C]//Proceedings of the Royal Society of London A: Mathematical, Physical and Engineering Sciences: volume 400. [S.l.]: The Royal Society, 1985: 97–117.
- [3] Shor P W. Algorithms for quantum computation: Discrete logarithms and factoring[C]//Foundations of Computer Science, 1994 Proceedings., 35th Annual Symposium on. [S.l.]: Ieee, 1994: 124–134.
- [4] Grover L K. A fast quantum mechanical algorithm for database search[C]//Proceedings of the twenty-eighth annual ACM symposium on Theory of computing. [S.l.]: ACM, 1996: 212–219.
- [5] Lloyd S, et al. Universal quantum simulators[J]. SCIENCE-NEW YORK THEN WASHINGTON-, 1996: 1073–1077.
- [6] DiVincenzo D P, et al. The physical implementation of quantum computation[J]. arXiv preprint quant-ph/0002077, 2000.
- [7] Ladd T D, Jelezko F, Laflamme R, et al. Quantum computers[J]. Nature, 2010, 464: 45–53.
- [8] Duan L M, Monroe C. Quantum networks with trapped ions[J]. Rev. Mod. Phys., 2012, 82: 1209–1224.
- [9] Wiesner S. Conjugate coding.[J]. ACM SIGACT News, 1983, 15: 78–88.
- [10] Pastawski F, Yao N Y, Jiang L, et al. Unforgeable noise-tolerant quantum tokens[J]. Proc. Natl Acad. Sci. USA, 2012, 109: 16079–16082.
- [11] Bollinger J, Heizen D, Itano W, et al. A 303-mhz frequency standard based on trapped be^+ ions [J]. IEEE Trans. Instrum. Meas., 1991, 40: 126–128.
- [12] Fisk P, Sellars M, Lawn M, et al. Very high q microwave spectroscopy on trapped $^{171}yb^+$ ions: application as a frequency standard[J]. IEEE Trans. Instrum. Meas., 1995, 44: 113–116.
- [13] Langer C, Ozeri R, Jost J D, et al. Quantum networks with trapped ions[J]. Phys. Rev. Lett., 2005, 95: 060502.
- [14] Saeedi K, Simmons S, Salvail J Z, et al. Room-temperature quantum bit storage exceeding 39 minutes using ionized donors in silicon-28[J]. Science, 2013, 342(6160): 830–833.
- [15] Zhong M, Hedges M P, Ahlefeldt R L, et al. Optically addressable nuclear spins in a solid with a six-hour coherence time[J]. Nature, 2015, 517(7533): 177–180.
- [16] Epstein R J, Seidelin S, Leibfried D, et al. Simplified motional heating rate measurements of trapped ions[J]. Phys. Rev. A, 2007, 76: 033411.
- [17] Wesenberg J, Epstein R, Leibfried D, et al. Fluorescence during Doppler cooling of a single trapped atom[J]. Phys. Rev. A, 2007, 76(5): 053416.
- [18] Khodjasteh K, Sastrawan J, Hayes D, et al. Designing a practical high-fidelity long-time quantum memory[J]. Nat. Commun., 2013, 4: 2045.

- [19] Biercuk M J, Uys H, VanDevender A P, et al. Optimized dynamical decoupling in a model quantum memory[J]. *Nature*, 2009, 458(7241): 996–1000.
- [20] Kotler S, Akerman N, Glickman Y, et al. Nonlinear single-spin spectrum analyzer[J]. *Phys. Rev. Lett.*, 2013, 110(11): 110503.
- [21] Souza A M, Álvarez G A, Suter D. Robust dynamical decoupling for quantum computing and quantum memory[J]. *Phys. Rev. Lett.*, 2011, 106(24): 240501.
- [22] Haeberlen U. High resolution nmr in solids selective averaging[M]. [S.l.]: Elsevier, 1976
- [23] Kielpinski D, Monroe C, Wineland D J. Architecture for a large-scale ion-trap quantum computer[J]. *Nature*, 2002, 417: 709–711.
- [24] Lekitsch B, Weidt S, Fowler A G, et al. Blueprint for a microwave trapped ion quantum computer[J]. *Sci. Adv.*, 2017, 3(2): e1601540.
- [25] Monroe C, Kim J. Scaling the ion trap quantum processor[J]. *Science*, 2013, 339: 1164–1169.
- [26] Nickerson N H, Fitzsimons J F, Benjamin S C. Freely scalable quantum technologies using cells of 5-to-50 qubits with very lossy and noisy photonic links[J]. *Phys. Rev. X*, 2014, 4: 041041.
- [27] Kielpinski D, Monroe C, Wineland D J. Architecture for a large-scale ion-trap quantum computer[J]. *Nature*, 2002, 417(6890): 709–711.
- [28] Paul W. Electromagnetic traps for charged and neutral particles[J]. *Reviews of modern physics*, 1990, 62(3): 531.
- [29] Wineland D J, Drullinger R E, Walls F L. Radiation-pressure cooling of bound resonant absorbers[J]. *Physical Review Letters*, 1978, 40(25): 1639.
- [30] Neuhauser W, Hohenstatt M, Toschek P, et al. Optical-sideband cooling of visible atom cloud confined in parabolic well[J]. *Physical Review Letters*, 1978, 41(4): 233.
- [31] Fisk P T, Sellars M J, Lawn M A, et al. Accurate measurement of the 12.6 ghz clock transition in trapped $^{171}\text{Yb}^+$ ions[J]. *IEEE Trans. Ultrason. Ferroelectr. Freq. Control*, 1997, 44(2): 344–354.
- [32] March R E. Quadrupole ion trap mass spectrometry: theory, simulation, recent developments and applications[J]. *Rapid Communications in Mass Spectrometry*, 1998, 12(20): 1543–1554.
- [33] Fortier T M, Ashby N, Bergquist J C, et al. Precision atomic spectroscopy for improved limits on variation of the fine structure constant and local position invariance[J]. *Physical Review Letters*, 2007, 98(7): 070801.
- [34] Rosenband T, Hume D, Schmidt P, et al. Frequency ratio of Al^+ and Hg^+ single-ion optical clocks; metrology at the 17th decimal place[J]. *Science*, 2008, 319(5871): 1808–1812.
- [35] Griffiths B, Wood G E. Introduction[M]//Monetary Targets. [S.l.]: Springer, 1981: 1–12
- [36] Dehmelt H G. Radiofrequency spectroscopy of stored ions i: Storage[J]. *Advances in Atomic and Molecular Physics*, 1968, 3: 53–72.
- [37] Wineland D J, Monroe C, Itano W M, et al. Experimental issues in coherent quantum-state manipulation of trapped atomic ions[J]. *Journal of Research of the National Institute of Standards and Technology*, 1998, 103(3): 259.
- [38] Olmschenk S, Matsukevich D, Maunz P, et al. Quantum teleportation between distant matter qubits[J]. *Science*, 2009, 323(5913): 486–489.

- [39] Leibfried y, Blatt R, Monroe C, et al. Quantum dynamics of single trapped ions[J]. *Reviews of Modern Physics*, 2003, 75(1): 281.
- [40] Siverns J, Simkins L, Weidt S, et al. On the application of radio frequency voltages to ion traps via helical resonators[J]. *Applied Physics B*, 2012, 107(4): 921–934.
- [41] Kim K, Chang M S, Korenblit S, et al. Quantum simulation of frustrated ising spins with trapped ions[J]. *Nature*, 2010, 465(7298): 590–593.
- [42] Islam R, Senko C, Campbell W, et al. Emergence and frustration of magnetism with variable-range interactions in a quantum simulator[J]. *Science*, 2013, 340(6132): 583–587.
- [43] Richerme P, Gong Z X, Lee A, et al. Non-local propagation of correlations in quantum systems with long-range interactions[J]. *Nature*, 2014, 511(7508): 198–201.
- [44] Senko C, Smith J, Richerme P, et al. Coherent imaging spectroscopy of a quantum many-body spin system[J]. *Science*, 2014, 345(6195): 430–433.
- [45] Debnath S, Linke N, Figgatt C, et al. Demonstration of a small programmable quantum computer with atomic qubits[J]. *Nature*, 2016, 536(7614): 63–66.
- [46] Waseda Y, Isshiki M. Purification process and characterization of ultra high purity metals: application of basic science to metallurgical processing[M]. [S.l.]: Springer Science & Business Media, 2012
- [47] Drever R, Hall J L, Kowalski F, et al. Laser phase and frequency stabilization using an optical resonator[J]. *Applied Physics B*, 1983, 31(2): 97–105.
- [48] Wang Y, Um M, Zhang J, et al. Single-qubit quantum memory exceeding ten-minute coherence time[J]. *Nature Photonics*, 2017, 11(10): 646.
- [49] Vittorini G, Hucul D, Inlek I, et al. Entanglement of distinguishable quantum memories[J]. *Physical Review A*, 2014, 90(4): 040302.
- [50] De Munshi D, Dutta T, Rebhi R, et al. Precision measurement of branching fractions of ba 138+: Testing many-body theories below the 1% level[J]. *Physical Review A*, 2015, 91(4): 040501.
- [51] Kurz N, Dietrich M, Shu G, et al. Measurement of the branching ratio in the 6 p 3/ 2 decay of ba ii with a single trapped ion[J]. *Physical Review A*, 2008, 77(6): 060501.
- [52] Röck N. Quantum manipulation on the barium quadrupolar transition[M]. [S.l.]: na, 2011
- [53] Chew A. Doppler-free spectroscopy of iodine at 739nm[J]. undergraduate thesis, University of Maryland, 2008.
- [54] Hite D A, Colombe Y, Wilson A C, et al. 100-fold reduction of electric-field noise in an ion trap cleaned with in situ argon-ion-beam bombardment.[J]. *Phys. Rev. Lett.*, 2012, 109(10): 103001.
- [55] Deslauriers L, Olmschenk S, Stick D, et al. Scaling and suppression of anomalous heating in ion traps[J]. *Physical Review Letters*, 2006, 97(10): 103007.
- [56] Nielsen M A, Chuang I L. Quantum computation and quantum information[M]. [S.l.]: Cambridge Univ., 2010
- [57] Home J P, Hanneke D, Jost J D, et al. Complete methods set for scalable ion trap quantum information processing[J]. *Science*, 2009, 325: 1227–1230.

- [58] Hanneke D, Home J P, Jost J D, et al. Realization of a programmable two-qubit quantum processor[J]. *Nat. Phys.*, 2010, 6: 13–16.
- [59] Duan L M, Blinov B B, Moehring D L, et al. Scalable trapped ion quantum computation with a probabilistic ion-photon mapping[J]. *Quantum Inf. Comput.*, 2004, 4(3): 165–173.
- [60] Blinov B, Moehring D, Duan L M, et al. Observation of entanglement between a single trapped atom and a single photon[J]. *Nature*, 2004, 428(6979): 153–157.
- [61] Moehring D L, Maunz P, Olmschenk S, et al. Entanglement of single atom quantum bits at a distance[J]. *Nature*, 2007, 449: 68–71.
- [62] Kurz C, Schug M, Eich P, et al. Experimental protocol for high-fidelity heralded photon-to-atom quantum state transfer[J]. *Nat. Commun.*, 2014, 5: 5527.
- [63] Ozeri R, Langer C, Jost J, et al. Hyperfine coherence in the presence of spontaneous photon scattering[J]. *Phys. Rev. Lett.*, 2005, 95(3): 030403.
- [64] Uys H, Biercuk M, VanDevender A, et al. Decoherence due to elastic rayleigh scattering[J]. *Phys. Rev. Lett.*, 2010, 105(20): 200401.
- [65] Campbell W, Mizrahi J, Quraishi Q, et al. Ultrafast gates for single atomic qubits[J]. *Phys. Rev. Lett.*, 2010, 105(9): 090502.
- [66] Ball H, Oliver W D, Biercuk M J. The role of master clock stability in quantum information processing[J]. *Nature Quantum Information*, 2016, 2: 16033.
- [67] Uhrig G S. Exact results on dynamical decoupling by π pulses in quantum information processes [J]. *New J. Phys.*, 2008, 10(8): 083024.
- [68] Knill E, Leibfried D, Reichle R, et al. Randomized benchmarking of quantum gates[J]. *Phys. Rev. A*, 2008, 77(1): 012307.
- [69] Kielpinski D, Kafri D, Woolley M J, et al. Quantum interface between an electrical circuit and a single atom.[J]. *Phys. Rev. Lett.*, 2012, 108(13): 130504.
- [70] Daniilidis N, Gorman D J, Tian L, et al. Quantum information processing with trapped electrons and superconducting electronics[J]. *New J. Phys.*, 2013, 251(15): 073017.
- [71] Barrett M, Chiaverini J, Schaetz T, et al. Deterministic quantum teleportation of atomic qubits [J]. *Nature*, 2004, 429(6993): 737–739.
- [72] Hensinger W, Olmschenk S, Stick D, et al. T-junction ion trap array for two-dimensional ion shuttling, storage, and manipulation[J]. *Applied Physics Letters*, 2006, 88(3): 034101.
- [73] Stick D, Hensinger W, Olmschenk S, et al. Ion trap in a semiconductor chip[J]. *Nature Physics*, 2006, 2(1): 36–39.
- [74] Wilpers G, See P, Gill P, et al. A monolithic array of three-dimensional ion traps fabricated with conventional semiconductor technology[J]. *Nature nanotechnology*, 2012, 7(9): 572–576.
- [75] Shaikh F, Ozakin A, Amini J M, et al. Monolithic microfabricated symmetric ion trap for quantum information processing[J]. *arXiv preprint arXiv:1105.4909*, 2011.
- [76] Madsen M, Hensinger W, Stick D, et al. Planar ion trap geometry for microfabrication[J]. *Applied Physics B: Lasers and Optics*, 2004, 78(5): 639–651.
- [77] Hucul D, Yeo M, Hensinger W, et al. On the transport of atomic ions in linear and multidimensional ion trap arrays[J]. *arXiv preprint quant-ph/0702175*, 2007.

- [78] Goursat E. A course in mathematical analysis: volume 2[M]. [S.l.]: Ginn & Company, 1917
- [79] Madsen M J. Advanced ion trap development and ultrafast laser-ion interactions[M]. [S.l.: s.n.], 2006.
- [80] Zhang J, Pagano G, Hess P, et al. Observation of a many-body dynamical phase transition with a 53-qubit quantum simulator[J]. arXiv preprint arXiv:1708.01044, 2017.
- [81] Auciello O, Pacheco S, Sumant A V, et al. Are diamonds a mems'best friend?[J]. IEEE Microwave magazine, 2007, 8(6): 61–75.
- [82] Berkeland D, Miller J, Bergquist J C, et al. Minimization of ion micromotion in a paul trap[J]. Journal of applied physics, 1998, 83(10): 5025–5033.
- [83] Monroe C, Meekhof D, King B, et al. Resolved-sideband raman cooling of a bound atom to the 3d zero-point energy[J]. Physical Review Letters, 1995, 75(22): 4011.
- [84] Turchette Q, King B, Leibfried D, et al. Heating of trapped ions from the quantum ground state [J]. Physical Review A, 2000, 61(6): 063418.
- [85] Zhang J, Zhang J, Zhang X, et al. Realization of geometric landau-zener-stückelberg interferometry[J]. Physical Review A, 2014, 89(1): 013608.
- [86] An S, Zhang J N, Um M, et al. Experimental test of the quantum jarzynski equality with a trapped-ion system[J]. Nature Physics, 2015, 11(2): 193–199.
- [87] Park J, Zhang J, Lee J, et al. Testing nonclassicality and non-gaussianity in phase space[J]. Physical review letters, 2015, 114(19): 190402.
- [88] Zhang X, Shen Y, Zhang J, et al. Time reversal and charge conjugation in an embedding quantum simulator[J]. Nature communications, 2015, 6.
- [89] Um M, Zhang J, Lv D, et al. Phonon arithmetic in a trapped ion system[J]. Nature communications, 2016, 7.
- [90] An S, Lv D, Del Campo A, et al. Shortcuts to adiabaticity by counterdiabatic driving for trapped-ion displacement in phase space[J]. Nature communications, 2016, 7.
- [91] Shen Y, Zhang X, Zhang S, et al. Quantum implementation of the unitary coupled cluster for simulating molecular electronic structure[J]. Physical Review A, 2017, 95(2): 020501.
- [92] Lv D, An S, Um M, et al. Reconstruction of the jaynes-cummings field state of ionic motion in a harmonic trap[J]. Physical Review A, 2017, 95(4): 043813.
- [93] James D, Jerke J. Effective hamiltonian theory and its applications in quantum information[J]. Canadian Journal of Physics, 2007, 85(6): 625–632.
- [94] Richerme P. Two-dimensional ion crystals in radio-frequency traps for quantum simulation[J]. Physical Review A, 2016, 94(3): 032320.

致 谢

衷心感谢导师 xxx 教授和物理系 xxx 副教授对本人的精心指导。他们的言传身教将使我终生受益。

在美国麻省理工学院化学系进行九个月的合作研究期间，承蒙 xxx 教授热心指导与帮助，不胜感激。感谢 xx 实验室主任 xx 教授，以及实验室全体老师和同学们的热情帮助和支持！本课题承蒙国家自然科学基金资助，特此致谢。

感谢 THUThesis，它的存在让我的论文写作轻松自在了许多，让我的论文格式规整漂亮了许多。

声 明

本人郑重声明：所呈交的学位论文，是本人在导师指导下，独立进行研究工作所取得的成果。尽我所知，除文中已经注明引用的内容外，本学位论文的研究成果不包含任何他人享有著作权的内容。对本论文所涉及的研究工作做出贡献的其他个人和集体，均已在文中以明确方式标明。

签 名：_____ 日 期：_____

附录 A Codes

A.1 Mathematica simulation program

```
<< PhysicalConstants`  
<< VectorAnalysis`  
mYb171 = 0.171 / AvogadroConstant / Mole;  
Ba138 = 0.138 / AvogadroConstant / Mole;  
qe = ElectronCharge / Coulomb;  
 $\Omega_{RF} = 2 \pi 39 \times 10^6$ ;  
RFV0lt = 1;  
dcorr =  $10^{-3}$ ;  
DcEndCapVoltage = 1;  
path = "D:\\CQI\\Design\\OneBodyTrap_Simulate\\20131018_LoadingSimulate\\";  
 $\eta_{z1} = 0.9702709454044968$ ;  
 $\eta_{z2} = 0.875817787719819$ ;  
 $\eta_{z3} = 0.6560355095941427$ ;  
 $\eta_1 = 1.66$ ;  
 $\eta_2 = 1.11$ ;  
 $\eta_3 = 1$ ;
```

图 A.1

Loading Radial data

```

In[17]:= s = "slope_RF.txt";
str =
  StringToStream[
    ReadList[path<>s, Record, RecordSeparators -> {" x, y, ex, ey (V/mm):"}][[2]];
ListTmp = ReadList[str, Number];
Close[str];
PotRFEF =
  ListInterpolation[Partition[Table[ListTmp[[nn*4-1]]^2+ListTmp[[nn*4]]^2, {nn, 10201}],
    101], {{-0.1, 0.1}, {-0.1, 0.1}}];
RFP[x_, y_] =  $\frac{qe}{4 mYb171 \Omega RF^2 dcorr^2}$  * PotRFEF[x, y];
s = "slope_DC_1.txt";
str =
  StringToStream[
    ReadList[path<>s, Record, RecordSeparators -> {" x, y, z and potential:"}][[2]];
Dc1 = ReadList[str, Number];
Close[str];
Dc1PA = ListInterpolation[Partition[Table[Dc1[[nn*4]], {nn, 10201}], 101],
  {{-0.1, 0.1}, {-0.1, 0.1}}];
s = "slope_DC_2.txt";
str =
  StringToStream[
    ReadList[path<>s, Record, RecordSeparators -> {" x, y, z and potential:"}][[2]];
Dc2 = ReadList[str, Number];
Close[str];
Dc2PA = ListInterpolation[Partition[Table[Dc2[[nn*4]], {nn, 10201}], 101],
  {{-0.1, 0.1}, {-0.1, 0.1}}];
s = "slope_DC_3.txt";
str =
  StringToStream[
    ReadList[path<>s, Record, RecordSeparators -> {" x, y, z and potential:"}][[2]];
Dc3 = ReadList[str, Number];
Close[str];
Dc3PA = ListInterpolation[Partition[Table[Dc3[[nn*4]], {nn, 10201}], 101],
  {{-0.1, 0.1}, {-0.1, 0.1}}];

```

图 A.2

Loading Axial data

```

In[37]:= s = "slope_DC_1_yz.txt";
str =
  StringToStream[
    ReadList[path<>s, Record, RecordSeparators -> {" x, y, z and potential:"}][[2]];
Dc1 = ReadList[str, Number];
Close[str];
Dc1PAyz =
  ListInterpolation[Transpose[Partition[Table[Dc1[[nn*4]], {nn, 10201}], 101]],
  {{-0.1, 0.1}, {-0.1, 0.1}}];
s = "slope_DC_2_yz.txt";
str =
  StringToStream[
    ReadList[path<>s, Record, RecordSeparators -> {" x, y, z and potential:"}][[2]];
Dc2 = ReadList[str, Number];
Close[str];
Dc2PAyz =
  ListInterpolation[Transpose[Partition[Table[Dc2[[nn*4]], {nn, 10201}], 101]],
  {{-0.1, 0.1}, {-0.1, 0.1}}];
s = "slope_DC_3_yz.txt";
str =
  StringToStream[
    ReadList[path<>s, Record, RecordSeparators -> {" x, y, z and potential:"}][[2]];
Dc3 = ReadList[str, Number];
Close[str];
Dc3PAyz =
  ListInterpolation[Transpose[Partition[Table[Dc3[[nn*4]], {nn, 10201}], 101]],
  {{-0.1, 0.1}, {-0.1, 0.1}}];

```

图 A.3


```

FreRotateXRP[RFVolt_, Vcenter_, Vinner_, Vouter_] := Module[{r, a, angle},
  RP[x_, y_] := RFVolt^2 RFP[x, y] + η2 Vinner DC2PA[x, -y] + η1 Vcenter DC3PA[x, y] +
    η2 Vinner DC2PA[x, -y] + η2 Vinner DC2PA[-x, y] + η1 Vcenter DC3PA[-x, -y] +
    η2 Vinner DC2PA[-x, y] + η3 Vouter DC1PA[x, y] + η3 Vouter DC1PA[x, y] +
    η3 Vouter DC1PA[-x, -y] + η3 Vouter DC1PA[-x, -y];
  r = 0.01;
  a = Table[RP[0 + r Cos[θ], 0 + r Sin[θ]], {θ, 0, π, 0.0001}];
  angle = Position[a, Min[a]][[1, 1]] * 0.0001;
  If[angle < π/2, angle = angle + π/2];
  {

$$\sqrt{\frac{qe}{mYb171 dcorr^2}} D[RP[0 + x \text{Cos}[angle], 0 + x \text{Sin}[angle]], x, x] /. x \rightarrow 0 / 2 / \pi,$$


$$\sqrt{\frac{qe}{mYb171 dcorr^2}} D[RP[0 + x \text{Cos}[angle + \pi/2], 0 + x \text{Sin}[angle + \pi/2]], x, x] /. x \rightarrow 0 / 2 / \pi,$$

    angle}
]

```

图 A.4

Simulate

```
 $\eta_1 = 1.6663261598171637` ;$   
 $\eta_2 = 1.1185497989945605` ;$   
centerOff = 8;  
innerOff = 20;  
RFVolt = 300;  
Vcenter = centerOff + (-5.1 - 23.1) / 24  
Vinner = innerOff + (399 + 548) / 24.  
Vouter = 0;  
PlotRP[RFVolt, Vcenter, Vinner, Vouter]  
FreRotateXRP[RFVolt, Vcenter, Vinner, Vouter]  
FreZAP[Vcenter, Vinner, Vouter]
```

6.825

59.4583

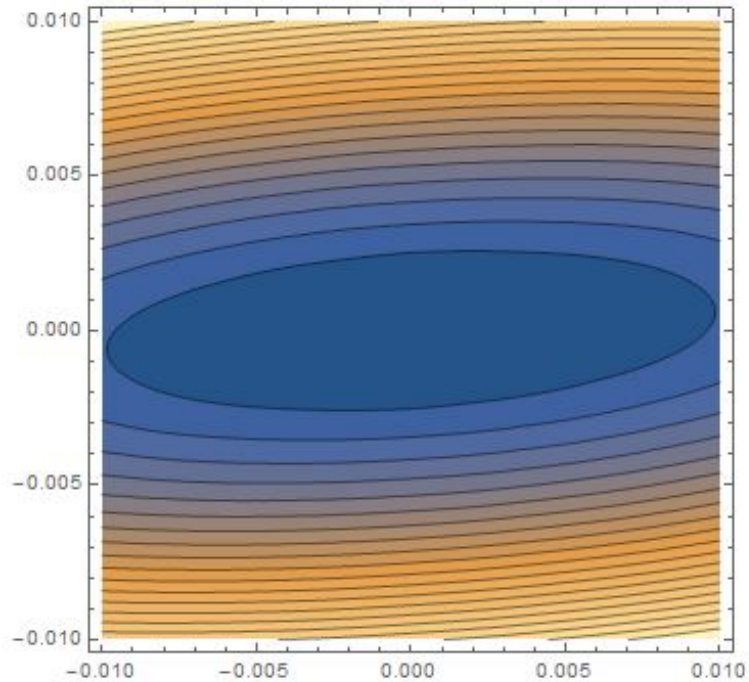


图 A.5

A.2 Program for generating different model with different parameters

```

import math

def GenerateElectricNode (AngleLU,AngleLD,AngleRU,AngleRD,RfLength,TrapDistance
,Dis1,Dis2,DcNumber,DcWidth,DcLength):#
    Dis1 is the distance between 2 dc rode.
    Dis2 is the distance between Dc and Rf
    .
    OutS = 'Default or template for CPO3D\nC:\cpo\OneBodyTrap\TmpFile\Dc_%.3f_%
        0.3f_%.3f_%.3f_%.3f_%.3f_%.3f_%.3f.txt name of
        hidden output file, for processed
        data\nC:\cpo\OneBodyTrap\Dc_%.3f_%.3f_%.3f_%.3f_%.3f_%.3f_%.3f_%.3f.txt name of
        main ray output file, for ray data\nm
        bbbv n/p/m/a for print level,
        cumulative, blank comment start,
        colour electrodes\n0 0 0 0 voltage
        reflection symmetries in x,y,z,x=y
        planes\n4 number of different
        voltages (time-independent)\n0.0001
        20 0 allowed consistency error,
        side/length ratio check, allow
        outside zs\na apply inscribing
        correction (a/s/n=always/sometimes/
        never)\n' % (AngleLU,AngleLD,AngleRU,
        AngleRD,RfLength,TrapDistance,Dis1,
        Dis2,DcNumber,DcWidth,DcLength,
        AngleLU,AngleLD,AngleRU,AngleRD,
        RfLength,TrapDistance,Dis1,Dis2,
        DcNumber,DcWidth,DcLength)

    #begin with Rf part
    OutS = OutS+'rec -simple flat rectangle Rf_1_1\n0 0 0 corner 1\n%.3f
        %.3f 0 corner 2\n0 0 %.3f
        corner 3\n%.3f %.3f %.3f corner
        4\n 1 1 numbers of 2 applied
        voltages (can be same)\n 3 51
        total nr of subdivs and 0, or
        subdivs along sides 1-2 and 2-3\
        ncolour 1\n'% (-RfLength,RfLength*
        math.tan(float(AngleLU)/180*math.pi),
        DcNumber*DcWidth+(DcNumber-1)*Dis1,-
        RfLength,RfLength*math.tan(float(
        AngleLU)/180*math.pi),DcNumber*
        DcWidth+(DcNumber-1)*Dis1)

```

```

OutS = OutS+'rec -simple flat rectangle      Rf_1_2\n0 0 0    corner 1\n%0.
3f %0.3f 0    corner 2\n0 0 %0.3f
corner 3\n%0.3f %0.3f %0.3f    corner
4\n 1 1 numbers of 2 applied
voltages (can be same)\n 3    51
        total nr of subdivs and 0, or
subdivs along sides 1-2 and 2-3\
ncolour      1\n'%(-RfLength,-RfLength*
math.tan(float(AngleLD)/180*math.pi),
DcNumber*DcWidth+(DcNumber-1)*Dis1,-
RfLength,-RfLength*math.tan(float(
AngleLD)/180*math.pi),DcNumber*
DcWidth+(DcNumber-1)*Dis1)

OutS = OutS+'rec -simple flat rectangle      Rf_2_1\n%0.3f %0.3f 0    corner
1\n%0.3f %0.3f 0    corner 2\n%0.3f
%0.3f %0.3f    corner 3\n%0.3f %0.3f
%0.3f    corner 4\n 1 1 numbers of
2 applied voltages (can be same)\n 3
51        total nr of subdivs and 0
, or subdivs along sides 1-2 and 2-3\
ncolour      1\n'%(TrapDistance,0,
TrapDistance+RfLength,RfLength*math.
tan(float(AngleRU)/180*math.pi),
TrapDistance+RfLength,RfLength*math.
tan(float(AngleRU)/180*math.pi),
DcNumber*DcWidth+(DcNumber-1)*Dis1,
TrapDistance,0,DcNumber*DcWidth+(
DcNumber-1)*Dis1)

OutS = OutS+'rec -simple flat rectangle      Rf_2_2\n%0.3f %0.3f 0    corner
1\n%0.3f %0.3f 0    corner 2\n%0.3f
%0.3f %0.3f    corner 3\n%0.3f %0.3f
%0.3f    corner 4\n 1 1 numbers of
2 applied voltages (can be same)\n 3
51        total nr of subdivs and 0
, or subdivs along sides 1-2 and 2-3\
ncolour      1\n'%(TrapDistance,0,
TrapDistance+RfLength,-RfLength*math.
tan(float(AngleRD)/180*math.pi),
TrapDistance+RfLength,-RfLength*math.
tan(float(AngleRD)/180*math.pi),
DcNumber*DcWidth+(DcNumber-1)*Dis1,
TrapDistance,0,DcNumber*DcWidth+(
DcNumber-1)*Dis1)

#begin with the dc part
#left up part
for j in range(DcNumber):
    if j != 1:

```

```

OutS = OutS + 'rec -simple flat rectangle      Dc_left_up_%d\n%0.3f %0.
3f %0.3f      corner 1\n%0.3f %0.3f %
%0.3f      corner 2\n%0.3f %0.3f %
0.3f      corner 3\n%0.3f %0.3f %0.
3f      corner 4\n 3 3 numbers
of 2 applied voltages (can be
same)\n 2 17      total nr of
subdivs and 0, or subdivs along
sides 1-2 and 2-3\ncolour 2\n'
%(j, -(RfLength+Dis2), (RfLength+
Dis2)*math.tan(float(AngleLU)/180
*math.pi), j*(DcWidth+Dis1), -(
RfLength+Dis2+DcLength), (RfLength
+Dis2+DcLength)*math.tan(float(
AngleLU)/180*math.pi), j*(DcWidth+
Dis1), -(RfLength+Dis2+DcLength), (
RfLength+Dis2+DcLength)*math.tan(
float(AngleLU)/180*math.pi), (j+1)
*(DcWidth+Dis1)-Dis1, -(RfLength+
Dis2), (RfLength+Dis2)*math.tan(
float(AngleLU)/180*math.pi), (j+1)
*(DcWidth+Dis1)-Dis1)

else:
OutS = OutS + 'rec -simple flat rectangle      Dc_left_up_%d\n%0.3f %0.
3f %0.3f      corner 1\n%0.3f %0.3f %
%0.3f      corner 2\n%0.3f %0.3f %
0.3f      corner 3\n%0.3f %0.3f %0.
3f      corner 4\n 2 2 numbers
of 2 applied voltages (can be
same)\n 2 17      total nr of
subdivs and 0, or subdivs along
sides 1-2 and 2-3\ncolour 2\n'
%(j, -(RfLength+Dis2), (RfLength+
Dis2)*math.tan(float(AngleLU)/180
*math.pi), j*(DcWidth+Dis1), -(
RfLength+Dis2+DcLength), (RfLength
+Dis2+DcLength)*math.tan(float(
AngleLU)/180*math.pi), j*(DcWidth+
Dis1), -(RfLength+Dis2+DcLength), (
RfLength+Dis2+DcLength)*math.tan(
float(AngleLU)/180*math.pi), (j+1)
*(DcWidth+Dis1)-Dis1, -(RfLength+
Dis2), (RfLength+Dis2)*math.tan(
float(AngleLU)/180*math.pi), (j+1)
*(DcWidth+Dis1)-Dis1)

#left down part
for j in range(DcNumber):
OutS = OutS + 'rec -simple flat rectangle      Dc_left_down_%d\n%0.3f %0.
3f %0.3f      corner 1\n%0.3f %0.3f %

```

```

0.3f    corner 2\n%0.3f %0.3f %0.3f
        corner 3\n%0.3f %0.3f %0.3f
corner 4\n 2 2 numbers of 2
applied voltages (can be same)\n 2
        17        total nr of subdivs and
0, or subdivs along sides 1-2 and 2
-3\ncolour 2\n'% (j, -(RfLength+
Dis2), -(RfLength+Dis2)*math.tan(
float(AngleLD)/180*math.pi), j*(
DcWidth+Dis1), -(RfLength+Dis2+
DcLength), -(RfLength+Dis2+DcLength)
*math.tan(float(AngleLD)/180*math.
pi), j*(DcWidth+Dis1), -(RfLength+
Dis2+DcLength), -(RfLength+Dis2+
DcLength)*math.tan(float(AngleLD)/
180*math.pi), (j+1)*(DcWidth+Dis1)-
Dis1, -(RfLength+Dis2), -(RfLength+
Dis2)*math.tan(float(AngleLD)/180*
math.pi), (j+1)*(DcWidth+Dis1)-Dis1)

#right up part
for j in range(DcNumber):
    OutS = OutS + 'rec -simple flat rectangle      Dc_right_up_%d\n%0.3f %0.3f
        %0.3f    corner 1\n%0.3f %0.3f %0.
3f    corner 2\n%0.3f %0.3f %0.3f
        corner 3\n%0.3f %0.3f %0.3f
corner 4\n 2 2 numbers of 2
applied voltages (can be same)\n 2
        17        total nr of subdivs and
0, or subdivs along sides 1-2 and 2
-3\ncolour 2\n'% (j, TrapDistance+
RfLength+Dis2, (RfLength+Dis2)*math.
tan(float(AngleRU)/180*math.pi), j*(
DcWidth+Dis1), TrapDistance+RfLength
+Dis2+DcLength, (RfLength+Dis2+
DcLength)*math.tan(float(AngleRU)/
180*math.pi), j*(DcWidth+Dis1),
TrapDistance+RfLength+Dis2+DcLength
, (RfLength+Dis2+DcLength)*math.tan(
float(AngleRU)/180*math.pi), (j+1)*(
DcWidth+Dis1)-Dis1, TrapDistance+
RfLength+Dis2, (RfLength+Dis2)*math.
tan(float(AngleRU)/180*math.pi), (j+
1)*(DcWidth+Dis1)-Dis1)

#right down part
for j in range(DcNumber):
    if j != 1:
        OutS = OutS + 'rec -simple flat rectangle      Dc_left_down_%d\n%0.3f %0
        .3f %0.3f    corner 1\n%0.3f %0.
3f %0.3f    corner 2\n%0.3f %0.3f

```

```

        %0.3f      corner 3\n%0.3f %0.3f %
0.3f      corner 4\n 3 3 numbers
of 2 applied voltages (can be
same)\n 2 17 total nr of
subdivs and 0, or subdivs along
sides 1-2 and 2-3\ncolour 2\n'
%(j,TrapDistance+RfLength+Dis2,-(
RfLength+Dis2)*math.tan(float(
AngleRD)/180*math.pi),j*(DcWidth+
Dis1),TrapDistance+RfLength+Dis2+
DcLength,-(RfLength+Dis2+DcLength
)*math.tan(float(AngleRD)/180*
math.pi),j*(DcWidth+Dis1),
TrapDistance+RfLength+Dis2+
DcLength,-(RfLength+Dis2+DcLength
)*math.tan(float(AngleRD)/180*
math.pi),(j+1)*(DcWidth+Dis1)-
Dis1,TrapDistance+RfLength+Dis2,-
(RfLength+Dis2)*math.tan(float(
AngleRD)/180*math.pi),(j+1)*(
DcWidth+Dis1)-Dis1)
else:
    OutS = OutS + 'rec -simple flat rectangle      Dc_left_down_%d\n%0.3f %0
.3f %0.3f      corner 1\n%0.3f %0.
3f %0.3f      corner 2\n%0.3f %0.3f
%0.3f      corner 3\n%0.3f %0.3f %
0.3f      corner 4\n 2 2 numbers
of 2 applied voltages (can be
same)\n 2 17 total nr of
subdivs and 0, or subdivs along
sides 1-2 and 2-3\ncolour 2\n'
%(j,TrapDistance+RfLength+Dis2,-(
RfLength+Dis2)*math.tan(float(
AngleRD)/180*math.pi),j*(DcWidth+
Dis1),TrapDistance+RfLength+Dis2+
DcLength,-(RfLength+Dis2+DcLength
)*math.tan(float(AngleRD)/180*
math.pi),j*(DcWidth+Dis1),
TrapDistance+RfLength+Dis2+
DcLength,-(RfLength+Dis2+DcLength
)*math.tan(float(AngleRD)/180*
math.pi),(j+1)*(DcWidth+Dis1)-
Dis1,TrapDistance+RfLength+Dis2,-
(RfLength+Dis2)*math.tan(float(
AngleRD)/180*math.pi),(j+1)*(
DcWidth+Dis1)-Dis1)
    OutS = OutS + '''end of electrode information
0      1 0.5      final nmbr segs, nmbr steps, weight, disable overlap test
1e-07      charge inacc,non-0 total Q,improve matrix,import

```



```

#ou = open('filelist.txt','w')
#ou.write('')
#for i in range(11):
# for j in range(11):
#   for k in range(11):
#       GenerateElectricNode(20+i*5,0.01+0.009*j,0.01+0.019*k,0.025,0.025,3,0.
#                               375,0.1)
#       ou.write('\ "Rf_%0.3f_%0.3f_%0.3f_%0.3f_%0.3f_%0.3f_%0.3f.dat\",'%(
#                               20+i*5,0.01+0.009*j,0.01+0.019*k,0.025,
#                               0.025,3,0.375,0.1))
#ou.write('')
#ou.close()

```

A.3 KDD_{xy} sequence

Sequence=

```

{
Chapter(DopplerCooling ,
00000000 00000000 00000000 00000000)
Chapter(OpticalPumping ,
11000000 00000000 00000000 00000000)
Chapter(Detection ,
10100000 00000000 00000000 00001111,
10000000 00000000 00000000 00000000,
10000000 00000000 00000000 00010000)
Chapter(Zero ,
10000000 00000000 00000000 00000000)
Chapter(ZeroOff000 ,
10001000 00010010 00000000 00000000)
Chapter(ZeroOff001 ,
10000000 00010010 00000001 00000000)
Chapter(ZeroOff010 ,
10000000 00010010 00000010 00000000)
Chapter(ZeroOff011 ,
10000000 00010010 00000011 00000000)

```

```
Chapter (ZeroOff100 ,
10000000 00010010 00000100 00000000)
Chapter (ZeroOff101 ,
10000000 00010010 00000101 00000000)
Chapter (ZeroOff110 ,
10000000 00010010 00000110 00000000)
Chapter (ZeroOff111 ,
10000000 00010010 00000111 00000000)
Chapter (ZeroOff000OS ,
10000000 00000010 00000000 00000000)
Chapter (ZeroOff001OS ,
10000000 00000010 00000001 00000000)
Chapter (ZeroOff010OS ,
10000000 00000010 00000010 00000000)
Chapter (ZeroOff011OS ,
10000000 00000010 00000011 00000000)
Chapter (ZeroOff100OS ,
10000000 00000010 00000100 00000000)
Chapter (ZeroOff101OS ,
10000000 00000010 00000101 00000000)
Chapter (ZeroOff110OS ,
10000000 00000010 00000110 00000000)
Chapter (ZeroOff111OS ,
10000000 00000010 00000111 00000000)

Chapter (MicroWaveTrigger ,
10010100 00010010 00000000 00000000)
Chapter (MicroWaveTriggerOS ,
10010100 00000010 00000000 00000000)

Chapter (MicroWave0 ,
10000000 00010010 00001100 00000000 ,
10000000 00010010 00011100 00000000)
```

Chapter (MicroWave90 ,
10000000 00010010 00001010 00000000 ,
10000000 00010010 00011010 00000000)
Chapter (MicroWave180 ,
10000000 00010010 00001001 00000000 ,
10000000 00010010 00001011 00000000 ,
10000000 00010010 00011011 00000000)
Chapter (MicroWave270 ,
10000000 00010010 00001001 00000000 ,
10000000 00010010 00011001 00000000)
Chapter (MicroWave120 ,
10000000 00010010 00001100 00000000 ,
10000000 00010010 00001110 00000000 ,
10000000 00010010 00011110 00000000)
Chapter (MicroWave30 ,
10000000 00010010 00001111 00000000 ,
10000000 00010010 00011111 00000000)
Chapter (MicroWave210 ,
10000000 00010010 00001100 00000000 ,
10000000 00010010 00001101 00000000 ,
10000000 00010010 00011101 00000000)
Chapter (MicroWave00S ,
10000000 00000010 00001100 00000000 ,
10000000 00000010 00011100 00000000)
Chapter (MicroWave900S ,
10000000 00000010 00001010 00000000 ,
10000000 00000010 00011010 00000000)
Chapter (MicroWave1800S ,
10000000 00000010 00001001 00000000 ,
10000000 00000010 00001011 00000000 ,
10000000 00000010 00011011 00000000)
Chapter (MicroWave2700S ,
10000000 00000010 00001001 00000000 ,

```
10000000 00000010 00011001 00000000)
Chapter (MicroWave120OS ,
10000000 00000010 00001100 00000000 ,
10000000 00000010 00001110 00000000 ,
10000000 00000010 00011110 00000000)
Chapter (MicroWave30OS ,
10000000 00000010 00001111 00000000 ,
10000000 00000010 00011111 00000000)
Chapter (MicroWave210OS ,
10000000 00000010 00001100 00000000 ,
10000000 00000010 00001101 00000000 ,
10000000 00000010 00011101 00000000)
-----
DopplerCooling (1000)
OpticalPumping (10)
MicroWave90 (2 ,7.80343)
MicroWaveTrigger (0.2)
ZeroOff000 (0.6)
MicroWaveTrigger (0.2)
ZeroOff000 (239999999.000)
MicroWaveTrigger (0.2)
ZeroOff000 (0.6)
MicroWaveTrigger (0.2)
ZeroOff000 (239850006.803)
ZeroOff000OS (149992.196566)
MicroWave90OS (2 ,7.80343)
Detection (375 ,1 ,1)
Zero (10)
}
```

个人简历、在学期间发表的学术论文与研究成果

个人简历

1989年09月01日出生于湖北省省浠水县。

2008年9月考入清华大学交叉信息研究院计算机科学实验班专业，2012年7月本科毕业并获得计算机科学与技术学士学位。

2012年9月免试进入清华大学交叉信息研究院攻读物理学位至今。

发表的学术论文

- [1] Wang Y, Um M, Zhang J, An S, Lyu M, Zhang JN, Duan LM, Yum D, Kim K. Single-qubit quantum memory exceeding ten-minute coherence time. *Nature Photonics*. 2017 Sep 25;11(10):646.

- [2] Um, Mark, Xiang Zhang, Junhua Zhang, Ye Wang, Shen Yangchao, D-L. Deng, Lu-Ming Duan, and Kihwan Kim. "Experimental certification of random numbers via quantum contextuality." *Scientific reports* 3 (2013).

- [3] Zhang X, Um M, Zhang J, An S, Wang Y, Deng DL, Shen C, Duan LM, Kim K. State-independent experimental test of quantum contextuality with a single trapped ion. *Physical review letters*. 2013 Feb 11;110(7):070401.

研究成果

综合论文训练记录表

| | | | | | |
|------------|--|----|--|----|--|
| 学生姓名 | | 学号 | | 班级 | |
| 论文题目 | | | | | |
| 主要内容以及进度安排 | <p>指导教师签字：_____</p> <p>考核组组长签字：_____</p> <p style="text-align: right;">年 月 日</p> | | | | |
| 中期考核意见 | <p>考核组组长签字：_____</p> <p style="text-align: right;">年 月 日</p> | | | | |

| | |
|---|--|
| <p style="text-align: center;">指导教师评语</p> | <p style="text-align: right;">指导教师签字：_____</p> <p style="text-align: right;">年 月 日</p> |
| <p style="text-align: center;">评阅教师评语</p> | <p style="text-align: right;">评阅教师签字：_____</p> <p style="text-align: right;">年 月 日</p> |
| <p style="text-align: center;">答辩小组评语</p> | <p style="text-align: right;">答辩小组组长签字：_____</p> <p style="text-align: right;">年 月 日</p> |

总成绩：_____

教学负责人签字：_____

年 月 日